SANDIA REPORT
SAND2010-6771
Unlimited Release
Printed October 2010

Dosimetry Experiments at the MEDUSA Facility (Little Mountain)

Victor J. Harper-Slaboszewicz, E. Frederick Hartman, Marty R. Shaneyfelt,
James R. Schwank, Timothy J. Sheridan

Prepared by
Sandia National Laboratories
Albuquerque, New Mexico 87185 and Livermore, California 94550

Sandia National Laboratories is a multi-program laboratory managed and operated by Sandia Corporation, a wholly owned subsidiary of Lockheed Martin Corporation, for the U.S. Department of Energy's National Nuclear Security Administration under contract DE-AC04-94AL85000.

Issued by Sandia National Laboratories, operated for the United States Department of Energy by Sandia Corporation.

Available to DOE and DOE contractors from
U.S. Department of Energy
Office of Scientific and Technical Information
P.O. Box 62
Oak Ridge, TN 37831

Telephone: (865) 576-8401
Facsimile: (865) 576-5728
E-Mail: reports@adonis.osti.gov
Online ordering: http://www.osti.gov/bridge

Available to the public from
U.S. Department of Commerce
National Technical Information Service
5285 Port Royal Rd.
Springfield, VA 22161

Telephone: (800) 553-6847
Facsimile: (703) 605-6900
E-Mail: orders@ntis.fedworld.gov
Online order: http://www.ntis.gov/help/ordermethods.asp?loc=7-4-0#online

SAND2010-6771
Unlimited Release
Printed October 2010

Dosimetry Experiments at the MEDUSA Facility (Little Mountain)

Victor J. Harper-Slaboszewicz
Radiation Effects Research Department 01344

E. Frederick Hartman, Timothy J. Sheridan
Radiation Effects Experimentation Department, 01343

Marty R. Shaneyfelt, James R. Schwank
17311 Radiation Physics, Technology and Assurance Department 17311

Sandia National Laboratories

P. O. Box 5800

Albuquerque, New Mexico 87185-MS 1159

Abstract

A series of experiments on the MEDUSA linear accelerator radiation test facility were performed to evaluate the difference in dose measured using different methods. Significant differences in dosimeter-measured radiation dose were observed for the different dosimeter types for the same radiation environments, and the results are compared and discussed in this report.

ACKNOWLEDGEMENTS

The authors acknowledge the close cooperation and services provided by the SVIC Linac operations personnel at the Little Mountain location of Hill AFB, UT. The authors appreciate the careful reading and thoughtful comments provided by Dave Beutler on the draft of this report. The authors also acknowledge the editing and formatting work on this report that was performed by Diana Wrobel.

Table of Contents

Table of Figures

Table of Tables

1 Executive Summary

A series of experiments on the MEDUSA linear accelerator (LINAC) radiation test facility were performed to evaluate the difference in dose measured using different methods. All of the following comments apply to operation in the long pulse mode, with pulse lengths varying from one to fifty microseconds.

The standard method for characterizing dose and dose rate at MEDUSA is the silicon calorimeter, with the advantages of rapid reading, measurement of the dose to the material of primary interest, and direct measurement of the quantity (energy deposition) of interest. Experiments show that, at a fixed position, as the pulse width is increased, the silicon dose tracks the beam energy as measured by the beam current and voltage fairly well. Experiments using the photocurrent output of a neutron-damaged transistor to measure silicon dose rate gave results consistent with the silicon calorimeter.

Measurements in electron beam mode at 19 MeV using manganese-doped calcium fluoride thermoluminescent dosimeters (TLDs) and silicon calorimeters at multiple dose rates, pulse widths, and doses indicate that the ratio of the TLD dose to the silicon dose in the same environment decreases with increasing dose above a dose of 50 krads(CaF_2:Mn), dropping to 0.6-0.7 at 200 krads(CaF_2:Mn). A possible mechanism for this reduced TLD response is proposed.

Experiments in the electron beam mode at 19 MeV using the threshold voltage shift due to oxide trapped charge in well-characterized MOSFETs as a measure of dose indicate that the dose response of the oxide is well behaved at all but the highest dose rate ($5x10^{10}$ rad(Si)/s), and that the dose to the oxide is larger than the dose measured using the silicon calorimeter by 60-90% at all doses. In addition, anomalous responses in the MOSFETs were observed at the highest dose rate ($5 x10^{10}$ rad(Si)/s). No mechanism for the enhanced oxide response at MEDUSA is identified.

Diamond PCDs are widely used for pulse shape measurement at high dose rate. Experiments at MEDUSA show that in the pulse width regime 1-50 microseconds, the PCD output does not track the silicon energy deposition as measured using the silicon calorimeter, especially during the first two microseconds. These detectors are currently used at MEDUSA as a transfer calibration, with the transfer measured for each position and pulse width. In this particular application, there is not a problem. However, PCDs should be used to measure details of pulse shape in this pulse length regime only with caution.

Lithium fluoride (LiF) TLDs are commonly used. They are convenient and inexpensive. Experiments at MEDUSA show that the doses measured with LiF TLDs are consistent with CaF_2:Mn TLDs up to about 30 krads. Above 30 krads, the dose measured with LiF TLDs is significantly less than that measured using the CaF2:Mn TLDs.

Alanine dosimeters are widely used as reference dosimeters because of their stability and precision. Experiments at MEDUSA show that alanine doses track doses measured with the silicon calorimeter to within about ±7%. However, the ratio of CaF_2:Mn dose to alanine dose drops by about 30% at a silicon

dose of 240 krads. This is consistent with the behavior of the ratio of CaF_2:Mn dose to silicon dose measured by the silicon calorimeter discussed above.

The results of this study provide no reason to believe that the silicon calorimeter does not provide a consistent and believable measure of ionization at a given position in the MEDUSA beam. There are clearly difficulties in extrapolating the calorimeter dose to other materials, geometries, and measurement systems, as indicated by the anomalies noted in CaF_2:Mn, LiF, silicon oxide, and diamond dose measurements in this report.

Dosimeter	Recommended uncertainty
Si calorimeter	when shooting frequently at > 100 kRad(Si) per pulse +6% /-13%, otherwise ±(6% + 30 rad(Si))
CaF_2:Mn TLD	±10% below 50 krad(Si), +30%/-10% above 50 krad(Si)
LiF TLD	±10% below 30 krads(Si), do not use above 30 krads(Si)
SiO_2 oxide trapped charge	±50%*
Diamond PCD	for pulses in the range 1-5 µs +10%/-30%

*+/- 50% based not on measurement accuracy, but based on variability in observed response likely due to incomplete understanding of kinetics of oxide trapped charge in this environment.

2 General Considerations for Electron Beam Radiation Effects Testing

2.1 Pulse Shape and Energy Spectrum

One major difference between bremsstrahlung photon sources[1] and high energy electron sources is the relative energy deposition in different materials.

For electron beam sources, the electron energies are concentrated near a single energy. The local electron energy deposition (obtained by multiplying the collisional stopping power by the electron fluence) is shown in Figure 1 for different electron energies. For LINAC sources the primary electrons are well above 1 MeV, and in this range the energy deposition varies from material to material by less than a factor of two.

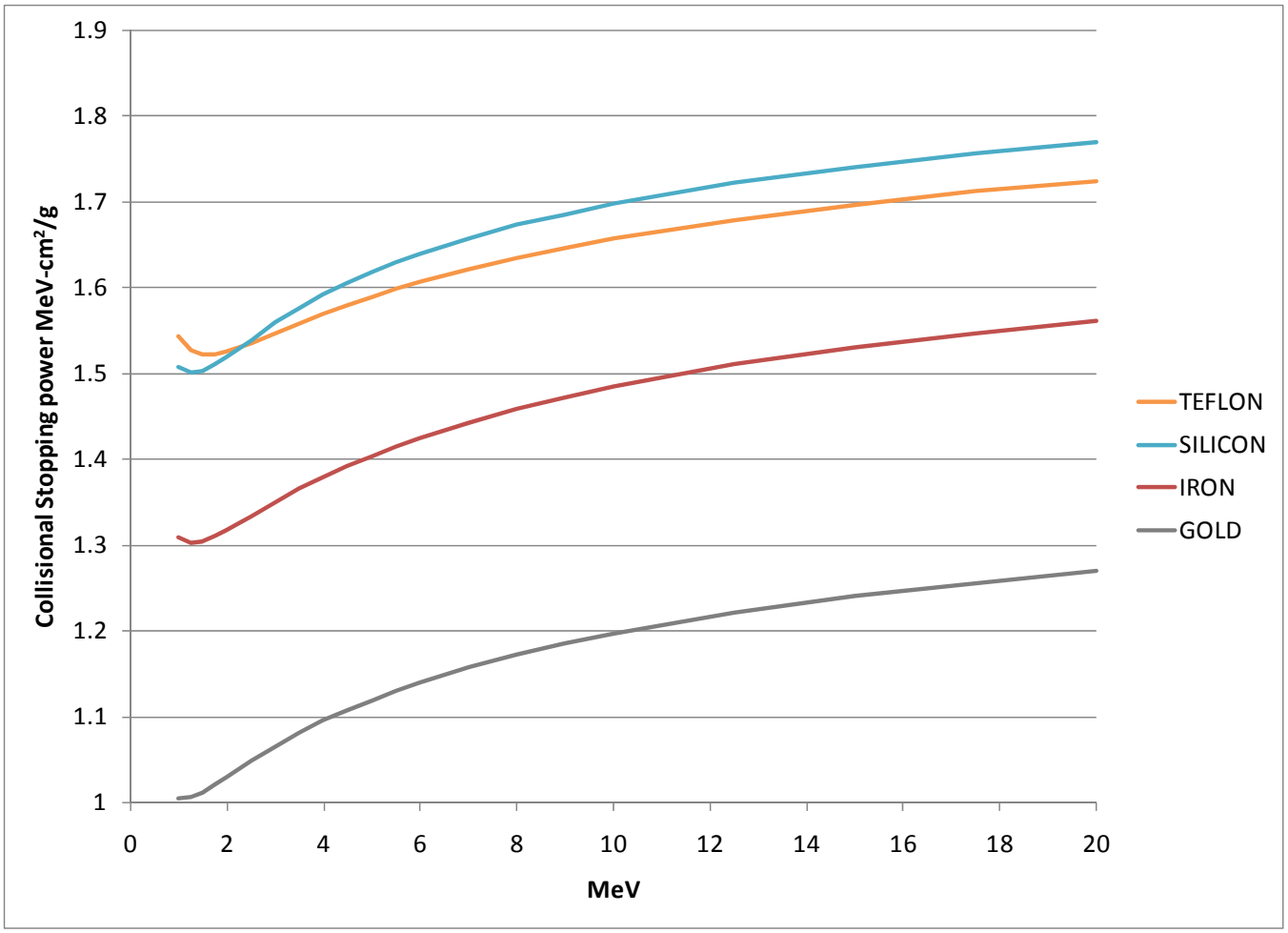

Figure 1: Collisional Stopping Power for Electrons for Various Materials

[1] E F Hartman, T A Zarick, T J Sheridan, and J C Riordan, "Spectral Unfolds of PITHON Flash X-ray Source", Sandia National Laboratories Report SAND2007-7667, December 2007.

For bremsstrahlung photon sources, the photon energy spectrum increases monotonically from the endpoint energy down to the point where intervening materials shield the radiation. This cutoff is typically somewhere in the vicinity of 100-300 keV. Therefore, for high voltage bremsstrahlung sources such as MEDUSA in brems mode, all photon energies from about 100 keV up to the endpoint are of interest. Figure 2 shows the quantity similar to stopping power for photons. When multiplied by the photon fluence, it gives the energy deposition in the material.

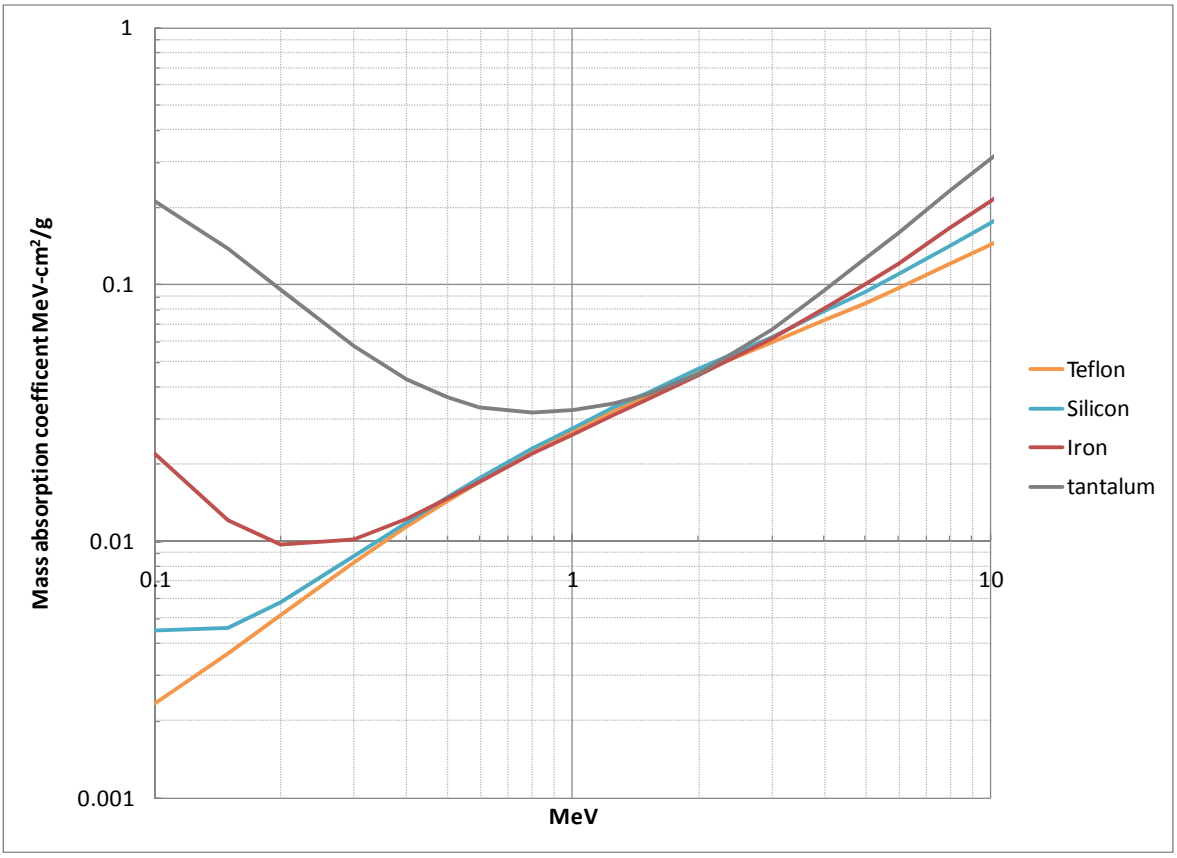

Figure 2: Photon Mass-Energy Absorption Coefficient for Various Materials

Note that the behavior of different materials above about 2 MeV is very similar, but below 2 MeV the behavior becomes dramatically different. The behavior of a test article containing multiple materials can be dramatically different for bremsstrahlung photon and electron sources.

2.1.1 19 MeV Mode

The MEDUSA LINAC at Little Mountain (see [2] for pictures of the facility) produces an electron beam with a nearly square current pulse shape and a nearly monoenergetic electron energy spectrum. The typical measured current pulse and electron energy spectrum at the beam head are shown below in Figures 3 and 4. The current is measured with a Pierson probe 18 inches beyond the last steering magnet (after the cavity) and 30 inches before the exit window of the beam pipe. The spectrum was measured using an analyzing magnet and a faraday cup behind a collimator at a fixed deflection angle. The energy was scanned by adjusting the analyzing magnet current.

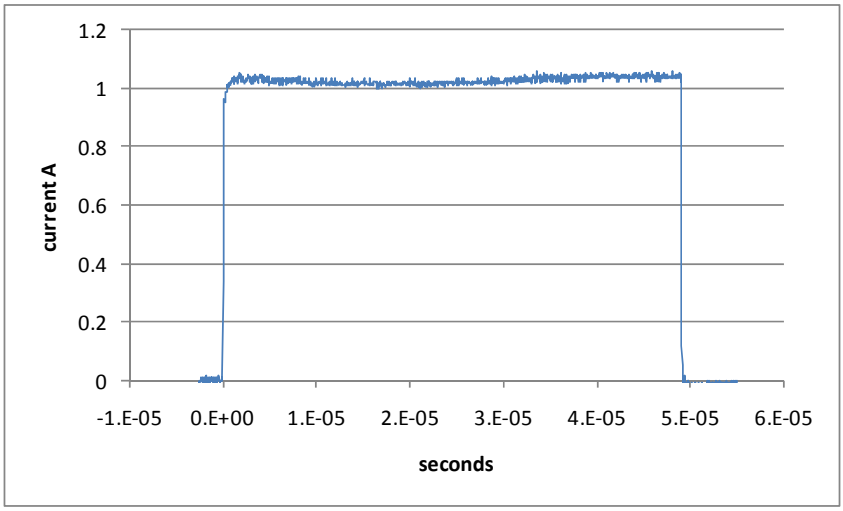

Figure 3: LINAC Current Pulse

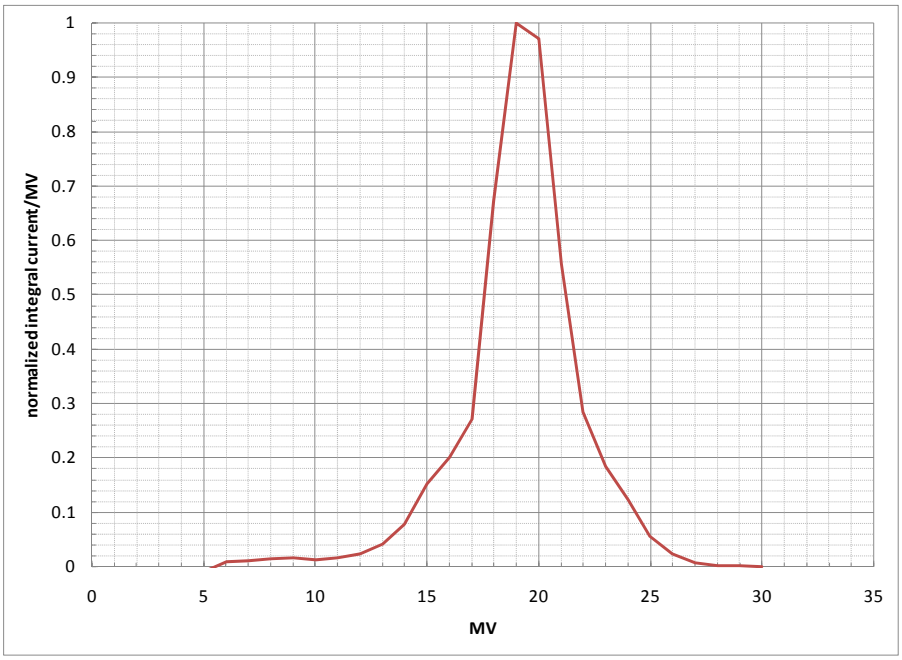

Figure 4: LINAC Electron Energy Spectrum

The spectrum is nearly independent of time, as shown in the Figure 5 below. The labels indicate the time after the beginning of the pulse when the spectrum was measured. It appears that the energy spectrum is initially peaked at 19 MeV, and then the peak moves down to 19 MeV between 1 and 5 microseconds. After that it moves up to 19 MeV again and stays there until the end of the pulse.

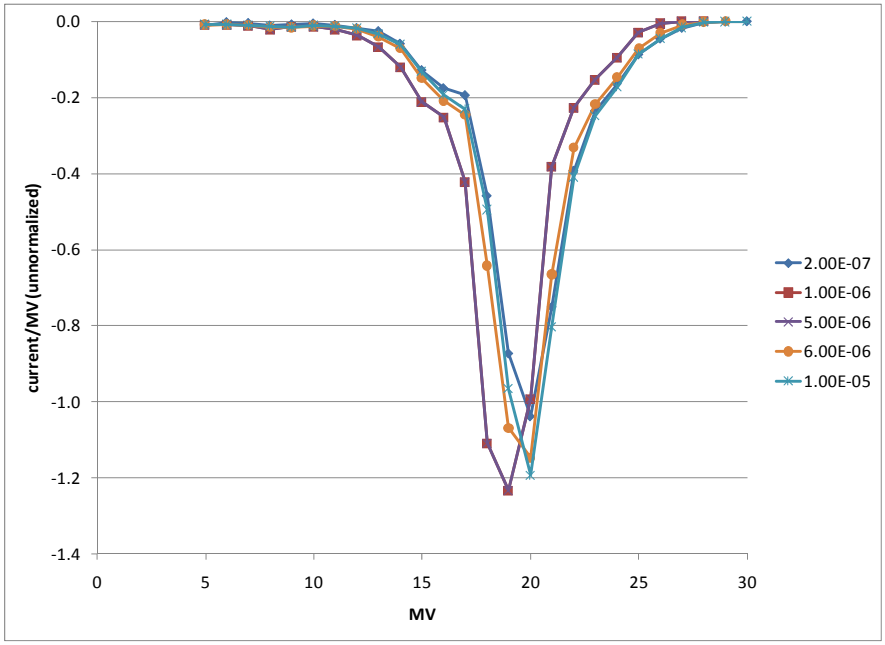

Figure 5: LINAC Electron Energy Spectra at Various Times during Single Pulse

2.1.2 10 MeV Mode

Similar data for the 10 MeV tuning of MEDUSA are shown in Figure 6 below. The pulse shape is once again nearly square.

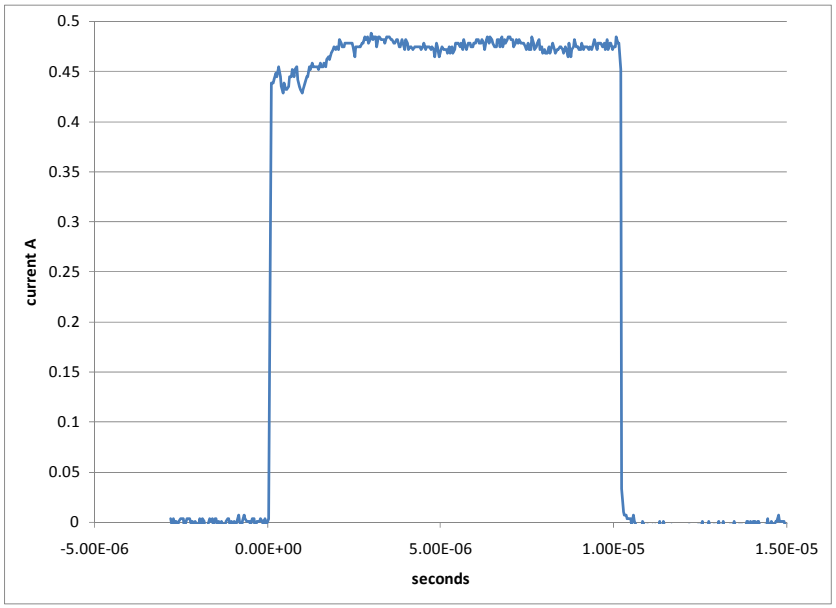

Figure 6: Typical 10μs LINAC Current Pulse Shape for 10 MeV Beam

The time-integrated spectrum is also narrow, with a somewhat more pronounced low energy tail than the 19 MeV beam as shown in Figure 7.

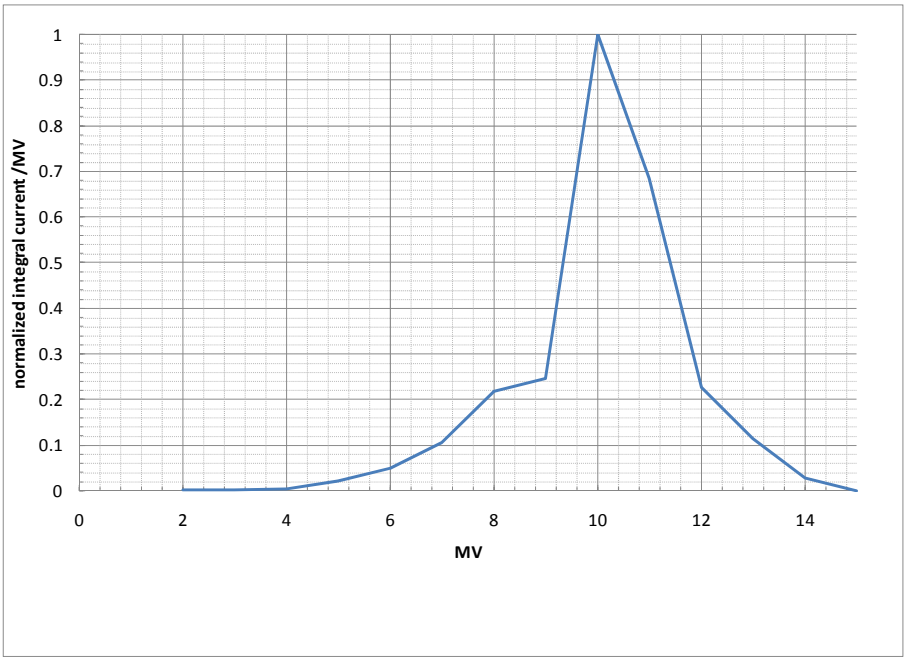

Figure 7: Time Integrated Electron Energy Spectrum for 19 MeV Beam

The 10-MeV spectrum shows somewhat more time dependence, with the initial spectrum at 200 ns about 3 MeV more energetic than the time-integrated spectrum. It drops to the time-integrated value by 1 microsecond, and remains there until close to the end of the pulse, at which time it becomes about 1 MeV more energetic again. Figure 8 illustrates the time dependence.

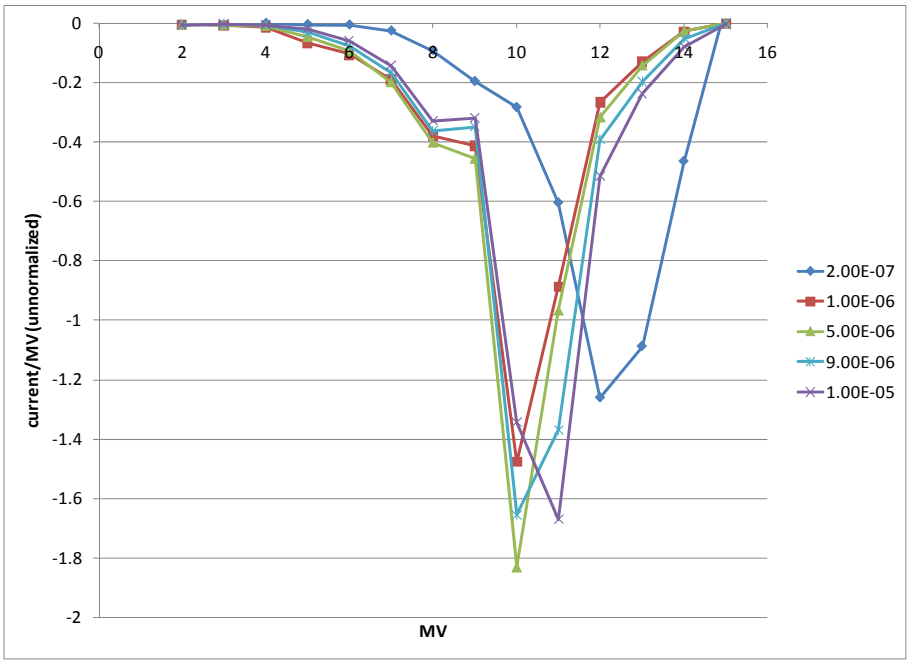

Figure 8: Time Dependence of Electron Energy Spectrum for 10-MeV Beam

2.1.3 Microstructure

One feature of the MEDUSA electron beam, shared with most LINACs, is microstructure in the electron pulse. The LINAC pulse has microstructure such that there are many short pulses of about 40-80 ps duration at a rep rate of about 1.3 GHz during the longer several microsecond pulse[2]. As a result, the instantaneous dose rate to a material during the microstructure peaks can be much higher than the pulse-averaged dose rate. However, as discussed in the Appendix, the energy deposition mechanisms relevant to this report occur on timescales which are either fast or slow compared to this microstructure pulse width, so the microstructure is not expected to have any significant effect on energy deposition in these experiments.

2.2 Beam Profile and Energy Deposition Profile

At the beam head the LINAC produces a small, highly forward directed beam with a high current density. To reduce beam bending and distortion by the heating of the air at this current density, a scatter plate at the beam head is used to broaden the beam. Beyond the scatter plate, the beam continues to diverge with the angular distribution introduced by the scatter plate so that the current density at the device under test is easily and reproducibly adjusted by varying the axial distance from the scatter plate to the test article.

There is an intrinsic tradeoff in the use of the scatter plate. A thinner scatter plate produces a narrower angular distribution of the beam, so higher dose rates can be achieved close in to the scatter plate. However, this narrower angular distribution produces a more peaked dose distribution across the test article, so small changes in lateral position on the test fixture can result in substantial changes in dose. Conversely, a thicker scatter plate produces a broader beam profile less sensitive to lateral position but does not allow the use of very high dose rates.

The axial energy deposition profile of high-energy electrons produced by the 19 MeV mode of MEDUSA is described by the Bragg-Gray curve, as shown as the blue curve in Figure 9 below for a solid. The dose builds up as the beam penetrates into the material, reaching a maximum value ~25% higher than the dose near the front surface, and then drops quickly. Also shown in red is the fraction of the dose due to primary electrons as a function of depth. To minimize variations in dose it is desirable that the dose in the material of interest be dominated by primary electron energy deposition.

[2] E F Hartman and T A Zarick, "A Test Protocol to Screen Capacitors for Radiation-Induced Charge Loss", Sandia National Laboratories Report SAND2008-5577, September 2008.

Another factor of interest is the deposition of charge into the material, also shown in green in Figure 9. Deposition of primary electrons into the material may affect the response of the device under test. . Also shown for reference are the positions of the 0.125 inch (purple dashed line) and 0.313 inch (light blue dashed line) scatter plates on the deposition curves.

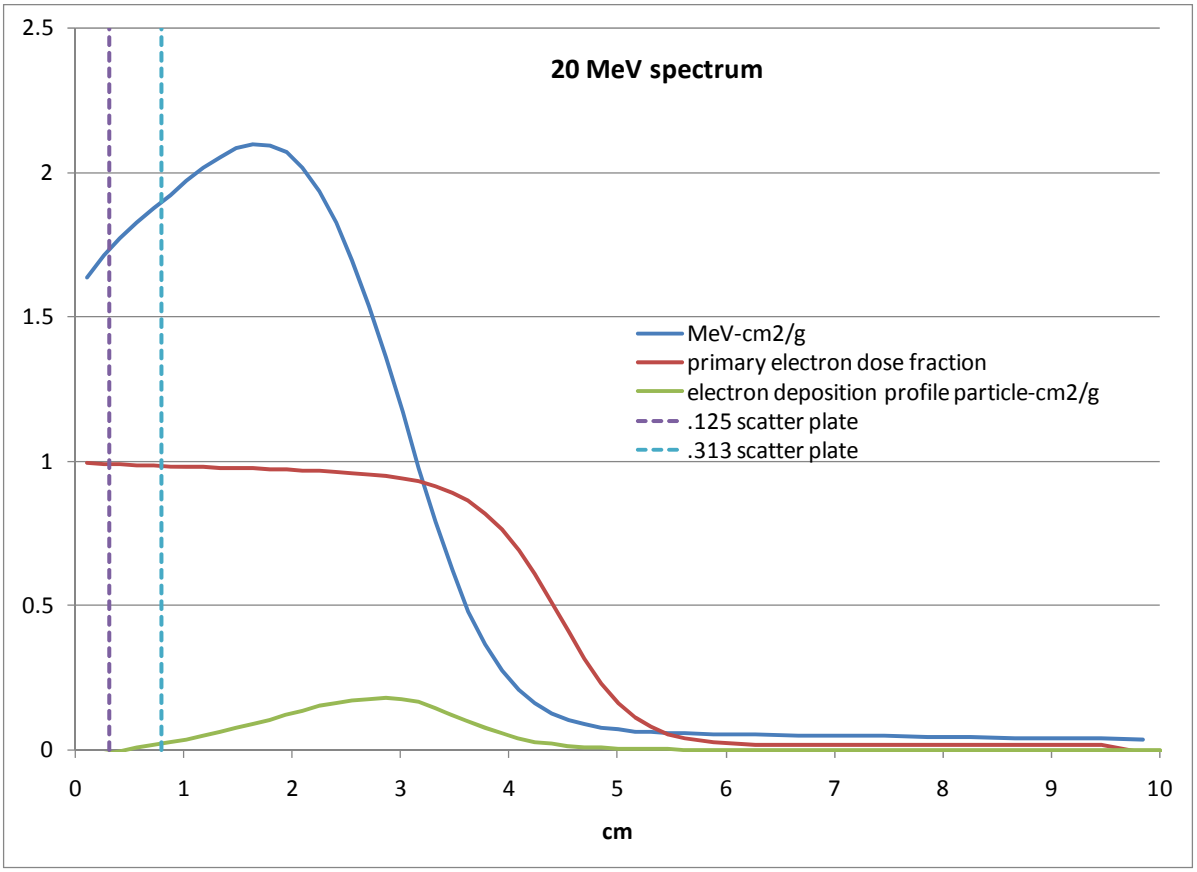

Figure 9: Dose Profiles for 19 MeV Spectrum

Corresponding distributions are shown for the nominal 10 MeV mode of MEDUSA in Figure 10 below. Note that the magnitudes remain similar, but they are considerably compressed in depth, so that the available mass thickness for radiation testing is considerably reduced compared to the nominal full voltage mode.

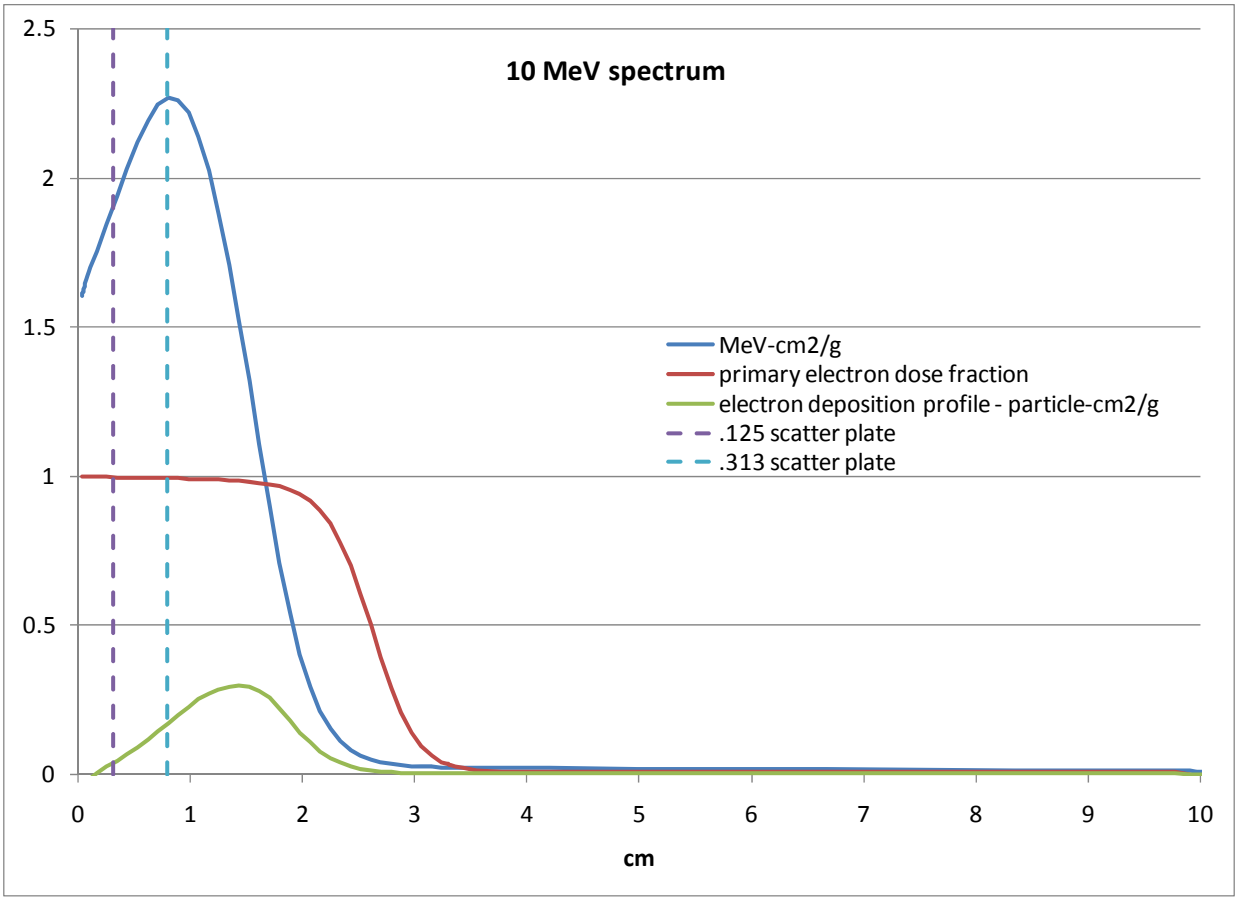

Figure 10: Dose Profile for 10 MeV Spectrum

3 Dosimetry using Silicon Calorimeter

The silicon calorimeter used at MEDUSA consists of two 0.5 mm thick, 5 mm square Si chips sandwiching a 1 mil thick Type E thermocouple. The calorimeter is embedded in a 0.11 g/cm^3 polystyrene foam, with 0.8 mm of foam in front of the silicon chips and 1.23 mm of foam behind the chips. The aluminum case is 0.8 mm thick in front and 2.65 mm thick behind. The calorimeter assembly is illustrated in Figure 11.

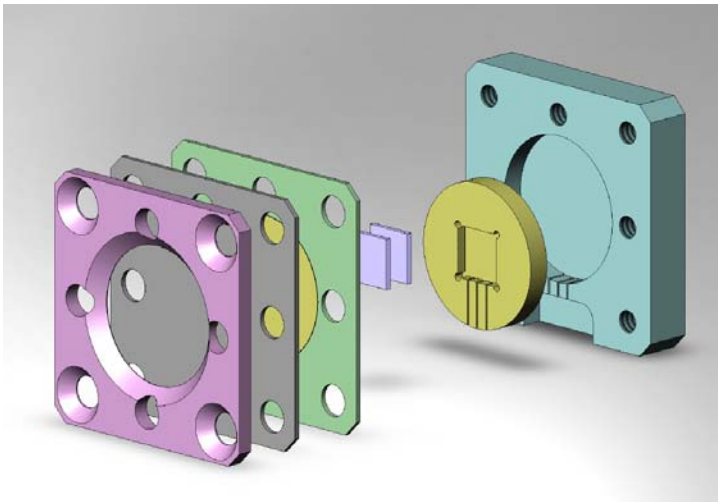

Figure 11: Silicon Calorimeter Assembly

The output of the thermocouple is filtered, amplified and recorded on an oscilloscope. Two stages of amplification are used. The first stage is a Stanford Research Systems SR560. This is used to filter the signal with a 30 Hz filter to reduce noise and to provide variable gain between 1 and 100. The second stage is a specially designed voltage amplifier with stable amplification and easily adjusted offset (the "blue amp").

The voltage step in the thermocouple output is converted to dose silicon using a conversion factor based on measured values of the silicon heat capacity and tabulated values for the Type E thermocouple output. The calorimeter is assumed to be at room temperature and the measured doses are assumed to be relatively small, so a constant room temperature conversion factor is used. The effect of this assumption is discussed below.

3.1 Calorimeter Reading Uncertainty at Low Dose

To obtain calorimeter readings at low dose, very large amplifications are used. Although the amplification is stable, these very large amplifications also amplify noise, which increases the uncertainty in the calorimeter readings below about 500 rad(Si). The apparent variability in dose readings at these low doses due to noise is approximately 30 rad(Si). Although this is difficult to resolve at higher doses, it is reasonable to expect that the same noise uncertainty is present at higher doses. Therefore, calorimeter measurements have an added uncertainty of about 30 rad(Si).

3.2 Potential Error in Calorimeter Measurement Due to Assuming a Constant Conversion Factor

The above conversions to dose assume a constant conversion factor. The temperature dependence of the conversion factor should be considered, since the calorimeter start temperature varies. The Seebeck coefficient for a Type E thermocouple increases slowly with temperature. Also, in this range, the heat capacity of silicon increases with temperature. These offsetting effects mean that the conversion factor is weakly dependent on temperature, as shown in Figure 12 below, generated using measured values of the specific heat[3].

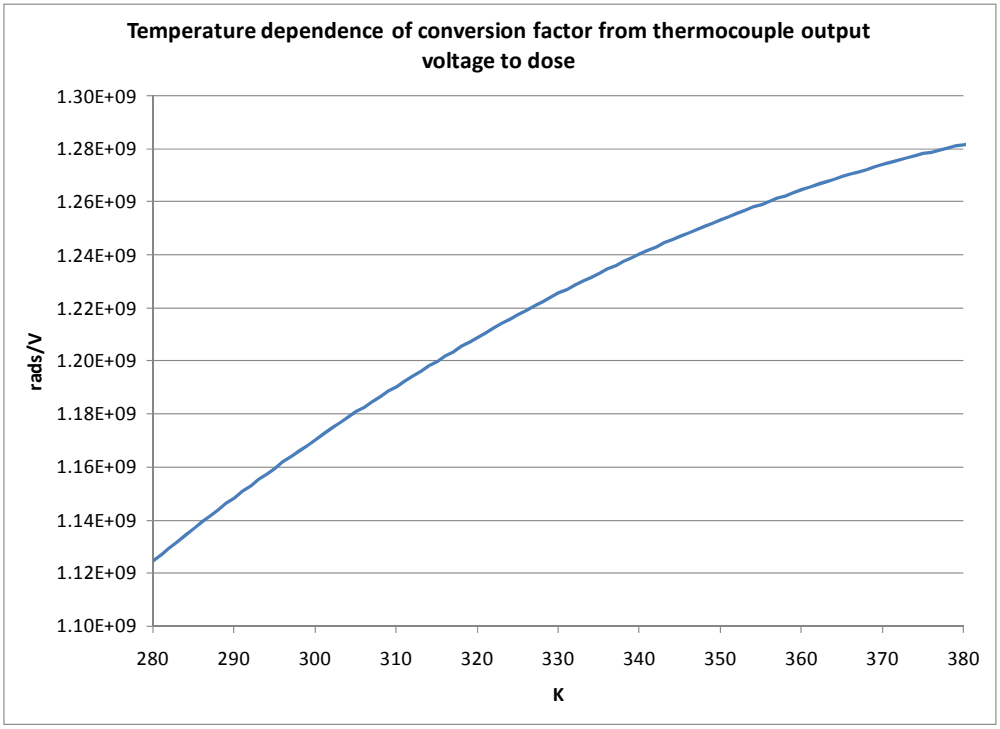

Figure 12: Temperature Dependence of Silicon Calorimeter Conversion Factor

The assumption of a constant conversion factor introduces error into the estimated dose in two ways. First, for large dose measurements, significant temperature excursions are expected, of approximately 14 K/Mrad(Si). If a 1 Mrad(Si) exposure were made starting at room temperature, the conversion factor would increase 2.5% by the end of the measurement, so the calculated dose assuming a constant conversion factor would be about 1.2% low. Second, for repeated dose measurements, the silicon calorimeter does not always cool down to room temperature in between exposures. The result could be a temperature excursion of as much as a few tens of degrees K. The true conversion factor might be as much as 7% higher than the nominal conversion factor for a 50 degree temperature excursion. As a result, the calculated dose might be as much as 7% lower than the true dose for rapid exposures with large accumulated dose.

[3] Specific Heat of Pure Silicon, A Report to Sandia National Laboratories, by Robert Taylor, January 2004, Thermophysical Properties Research Laboratory, Inc., TPRL 3103.

The effect of neglecting the temperature dependence of the conversion factor from volts to rads(Si) is to underestimate the silicon dose by up to a few percent for rapid large dose exposures.

3.2.1 Consistency Measurements

A series of experiments were performed to evaluate the reproducibility of the silicon calorimeter measurements. These included exposing multiple calorimeters, all of the same basic design but built at different times by different people, to the same environment and comparing the results; using different amplifiers in the signal path and comparing the results; and looking at the axial falloff of the dose measured using a silicon calorimeter to see how it compares with the $1/r^2$ falloff expected from an effective point source. All of these measurements were made with MEDUSA in 19 MeV electron beam mode with a 0.313 inch scatter plate.

3.2.1.1 Intra-day and Day to Day Reproducibility

One set of experiments was performed to evaluate the variation in the calorimeter output intra-day and day-to-day, keeping the position, calorimeter, and amplifier constant. This is typically what happens during an experimental run. The results are shown in Table 1. The variation reflects the combined variability in the calorimeter response and electron beam during an experimental run. Hence, this provides an upper bound on the random variability in the calorimeter response over these time scales. These experiments were performed using calorimeter 001 and amplifier 006 using a fixed accelerator pulse width of 49 microseconds. Six exposures were made at each axial position on each day.

Table 1: Intra-day and Day to Day Reproducibility of the Silicon Calorimeter

position	1	2	3	4
day 1 mean	70278	20229	6719	1942
day 1 σ %	0.26%	0.25%	0.38%	0.68%
day 2 mean	70401	20313	6740	1948
day 2 σ %	0.51%	0.66%	0.90%	1.04%
day 1 to day 2 δ %	-0.17%	-0.41%	-0.31%	-0.34%

The shot-to-shot uncertainty is approximately 1%, and increases at lower doses. The day to day change is within the shot-to-shot uncertainty.

3.2.1.2 Calorimeter to Calorimeter Variability

Another set of experiments was performed to evaluate the calorimeter to calorimeter variability. The results are shown in Table 2. These experiments were performed using amplifier 006 and multiple calorimeters using a fixed accelerator pulse width of 49 microseconds. Three exposures were made at each axial position with each calorimeter.

Table 2: Silicon Calorimeter to Calorimeter Reproducibility

calorimeter number/position	1	2	3	4
001	70122	20194	6687	1938
002	70434	20276	6723	1939
003	68398	19633	6617	1935
004	69939	20011	6641	1923
005	68761	20023	6598	1924
011	70309	20140	6673	1921
012	68702	19403	6398	1827
014	70434	19960	6561	1870
015	69627	20136	6697	1952
σ %	1.16%	1.42%	1.49%	2.09%
range %	2.92%	4.37%	4.91%	6.50%

The range is defined as the difference between the maximum and minimum readings among the six calorimeters divided by the average reading at a given position. The maximum range is 6.5%, and occurs at the lowest doses (position 4).

3.2.1.3 Amplifier to Amplifier Variability

The final set of experiments was performed to evaluate the amplifier to amplifier variability. The results are show in Table 3. These experiments were performed using a single calorimeter (numbered 001) and multiple "blue" amplifiers using a fixed accelerator pulse width of 49 microseconds. Three exposures were made at each axial position with each amplifier.

Table 3: "Blue" Amplifier to Amplifier Reproducibility

amplifier number/position	1	2	3	4
001	70512	20315	6733	1959
002	70122	20120	6660	1957
003	70496	20257	6735	1939
004	70060	20198	6703	1951
006	70278	20229	6719	1942
σ %	0.30%	0.36%	0.45%	0.45%
range %	0.64%	0.96%	1.11%	1.00%

The range is defined as the difference between the maximum and minimum readings among the six calorimeters divided by the average reading at a given position. The maximum range just over 1%, and occurs at position 3. This "blue" amplifier variability is indistinguishable from the shot to shot variability using a single calorimeter and amplifier.

3.2.1.4 Stanford Amplifier Gain Consistency

The consistency of the gain of the Stanford amplifier used between the calorimeter and the "blue" amplifier was characterized by a series of shots at multiple pulse lengths and dose rates, holding the position, pulse width, calorimeter, and "blue" amplifier constant while the Stanford amplifier gain was varied. The results are shown in Figure 13. The vertical axis is the ratio of the dose at a gain to the dose at gain=1 for the specified condition. The range is ±2%, while the standard deviation is 0.9%.

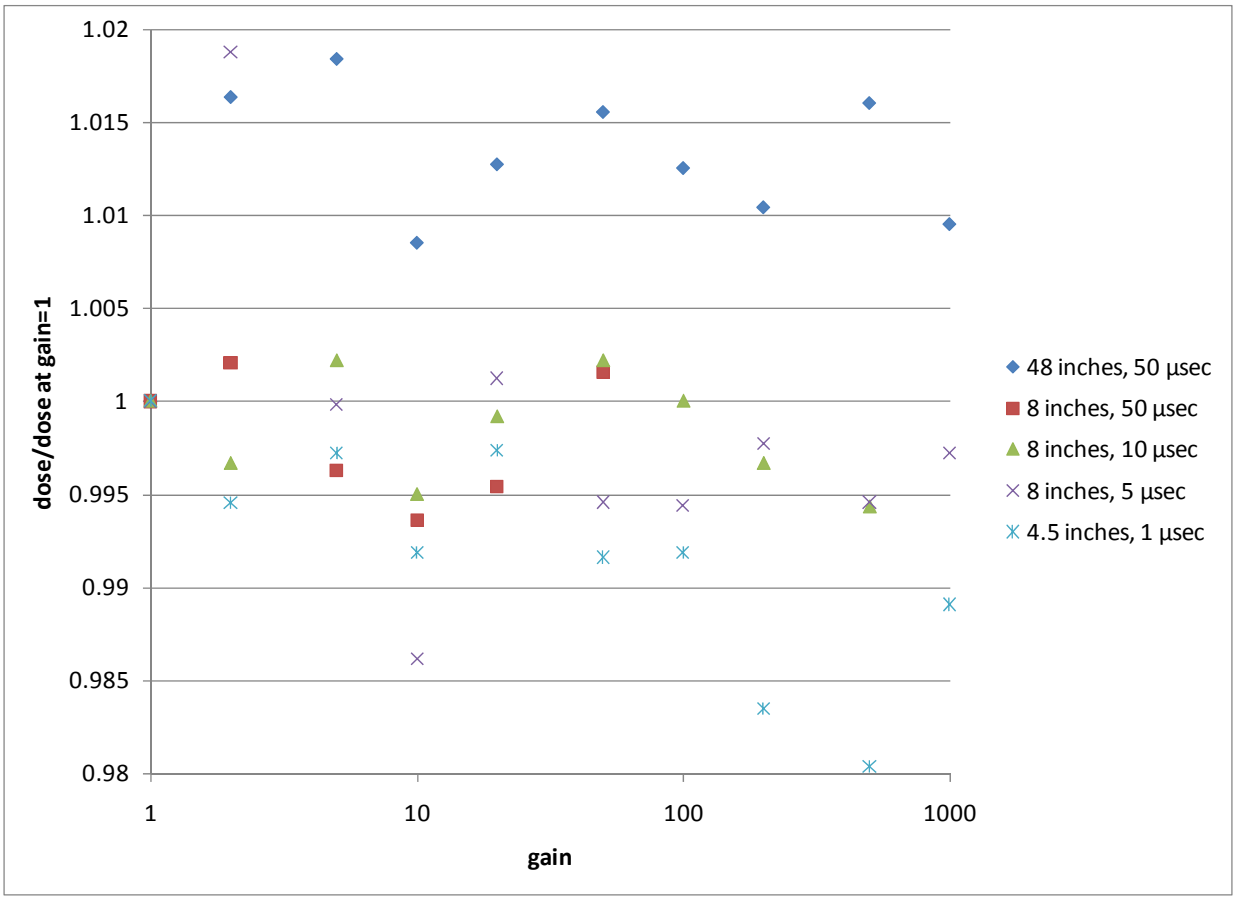

Figure 13: Stanford Amplifier Gain Consistency

3.2.2 Modeling of Heat Flow in the Silicon Calorimeter

Detailed modeling of the heat flow in the silicon calorimeter using the as-built geometry was performed, and the results are shown in Figure 14 below. The very good agreement shows there are likely no anomalies in heat flow that are biasing the silicon calorimeter results.

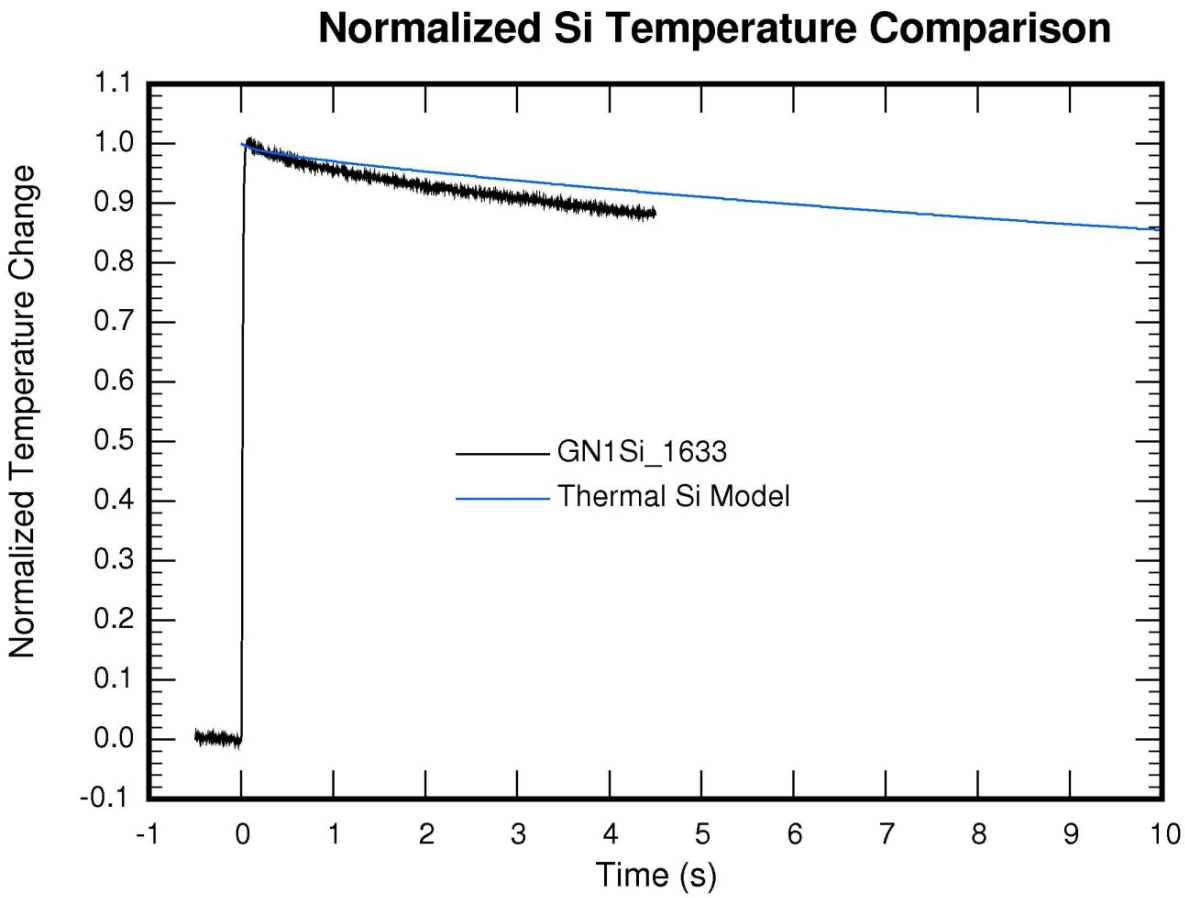

Figure 14: Measured and Calculated Temperature Relaxation in Silicon Calorimeter

3.2.3 Dose-distance Behavior of Silicon Calorimeter

To evaluate the consistency of the silicon calorimeter measurements with the expected $1/r^2$ behavior of a point source, three scans of calorimeter output vs. distance were performed using calorimeter 001 and "blue" amplifier 006 for nominal pulse widths of 1, 5, and 10 microseconds. The results are shown in Figure 15 below along with power law fits to the data for each pulse width. These show that the falloff with distance (in this case, distance is defined as how far the silicon calorimeter is located from the exit port of the LINAC) is very close to $1/r^2$, as it should be if there are not dose-dependent anomalies in the silicon calorimeter response.

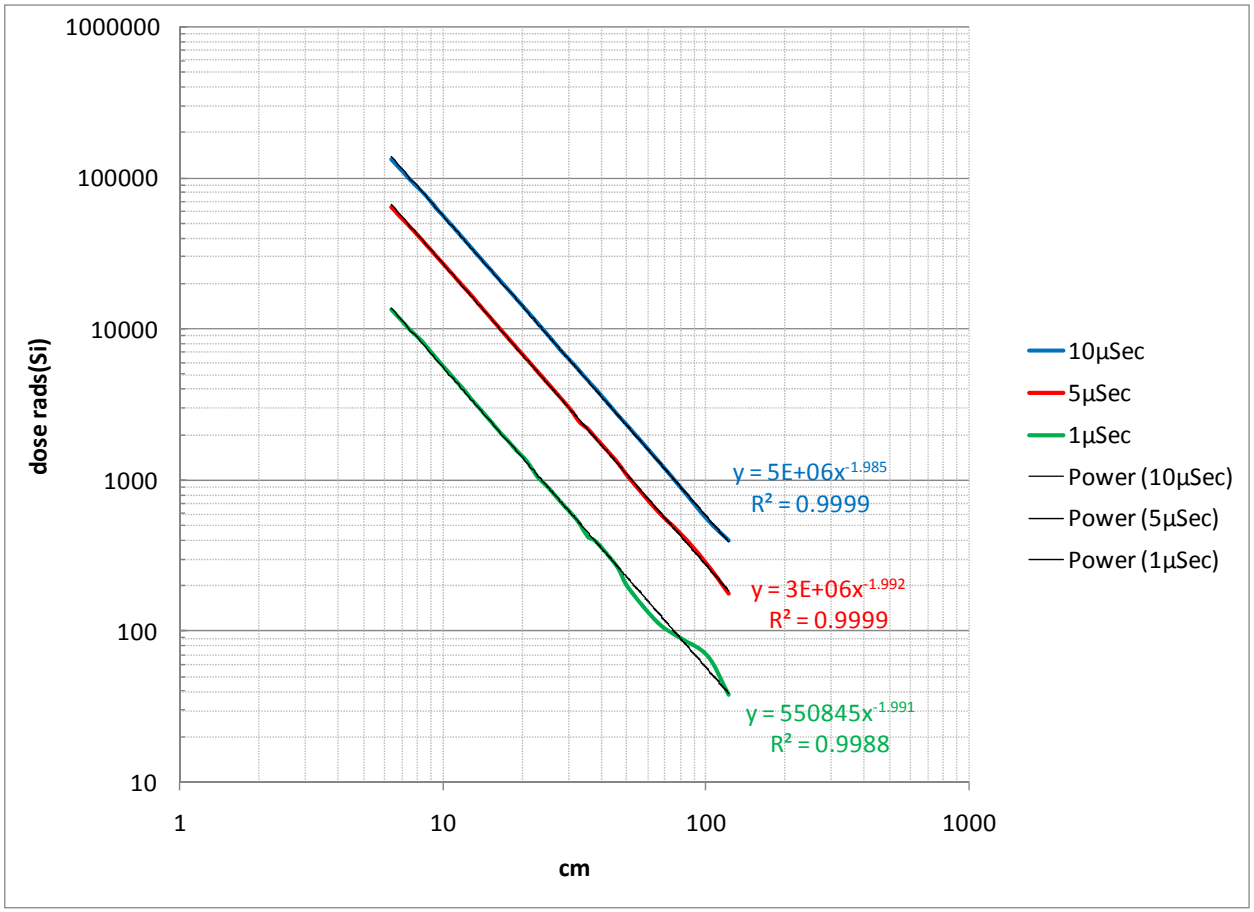

Figure 15: Dose vs. Distance for Silicon Calorimeter

3.2.4 Silicon Calorimeter Dose vs. Pulse Width

For a fixed beam energy spectrum and geometry, the dose at any fixed position should scale linearly with the electron fluence. As shown earlier, the MEDUSA energy spectrum is almost constant with time, so one would expect this linear scaling. Therefore, the ratio of dose as measured with the calorimeter to the integral of the beam current should be a constant. This ratio is shown as a function of pulse width in Figure 16. To allow plotting of this ratio for multiple positions, the values of the ratio rad(Si)/Coulomb for each position and pulse width have been normalized to the value at that position at 1 microsecond pulse width.

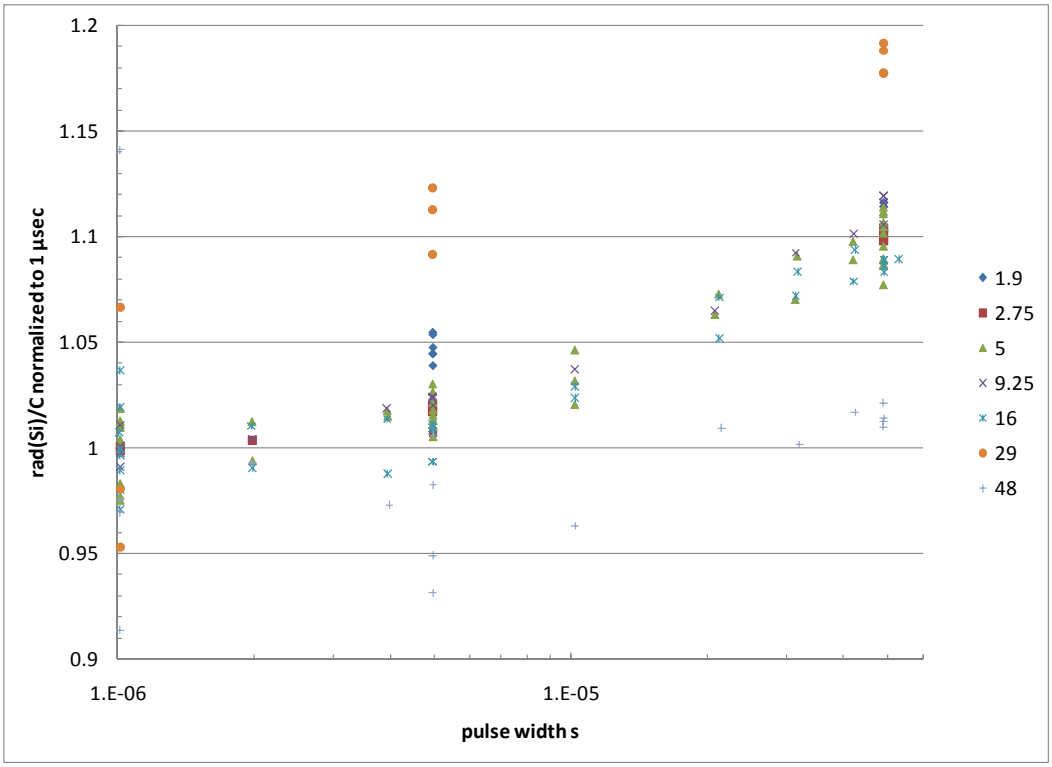

Figure 16: Silicon Calorimeter Dose (rad(Si)) to Beam Current Integral (C) Ratio for Different Pulse Widths and Dose Rates

(Dose rates are set by the distance silicon calorimeter is located from the exit port of the LINAC and the number is given in inches on the right side of graph.)

Note that the most of the data for the silicon Calorimeter shows a pronounced trend of increasing ratio of dose to current integral with increasing pulse width. The values for the 29 and 48 inch positions are parallel to but offset from the general trend. This offset is likely an artifact of the error in measuring the (low) dose at 1 microsecond with the silicon calorimeter in these positions.

The increase in the ratio of dose to current integral may be the result of some weak beam self-focusing due to heating of the air between the beam head and the measurement point, since small-angle scattering of the electrons in the presence of a lateral density gradient results in preferential scattering towards the region of lower density.

3.2.5 Silicon Calorimeter Comparison with Neutron-damaged Transistor Photocurrent Integral

In a previous test series, a variety of dose measurement methods were evaluated at MEDUSA using the 19 MeV tuning of the LINAC and a 0.313 inch thick scatter plate. Most of the measurements were taken at a dose rate of approximately 1E9 rad(Si)/s.

Another silicon dose measurement method evaluated was the integral of the photocurrent output of a neutron-damaged 2N2222 transistor. The transistor was damaged with 3E14 1-MeV Si-equivalent n/cm^2 at ACRR and then annealed in accordance with ASTM E 722 to stabilize the damage. The transistor photocurrent was measured using a reverse bias of 10 V on the collector-base junction, with the emitter leg was left open. The base signal was measured across 50 ohms using a Lecroy 6100 Waverunner oscilloscope.

The integral of the transistor photocurrent is compared to the silicon calorimeter signal for a fixed position, calorimeter, and "blue" amplifier, computing the ratio for each value of pulse width. These ratios are normalized to the value for the 1 microsecond pulse width. For the transistor photocurrent integral, the ratio is 1 at 1 microsecond pulse width and stabilizes at a value of approximate 0.98 for all other pulse widths, as shown in Figure 17.

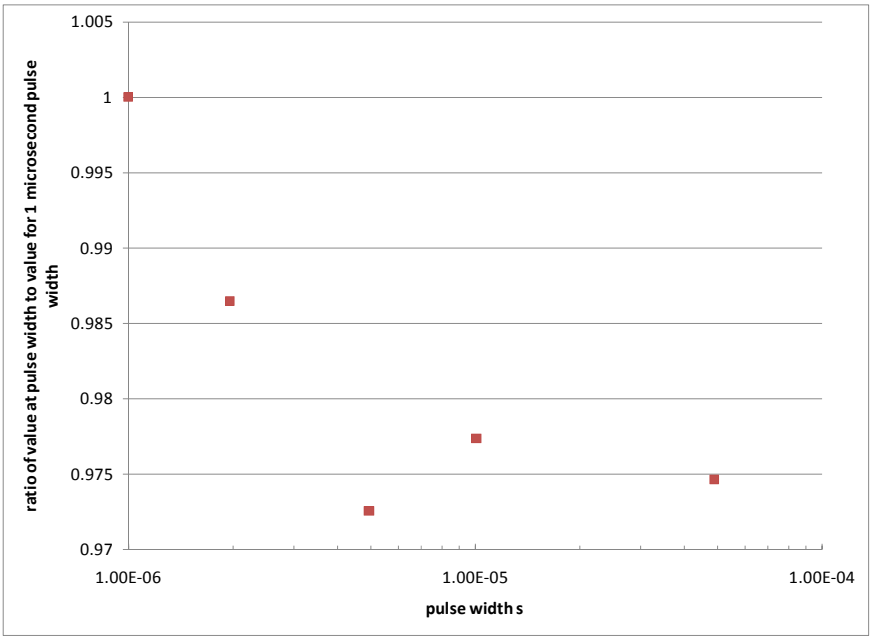

Figure 17: Normalized Ratio of Photocurrent Integral Dose to Calorimeter Signal Dose for Multiple Pulse Widths

3.2.6 Discussion of Silicon Calorimeter Results

A series of consistency measurements shows variations in dose readings among different amplifiers results in an uncertainty of no more than about ±2%. Variations among calorimeters may contribute ±5%. The time dependence of the silicon calorimeter output agrees well with thermal modeling using standard values for the thermal properties of the calorimeter materials, so anomalous heat flow should not be affecting calorimeter output. The dose-distance behavior of the silicon calorimeter indicates a linear response over the range of interest. The dose pulse width behavior suggests a slightly increasing

measured dose rate at a fixed position with increasing pulse width. This is likely the result of weak focusing of the electron beam in air for pulses in the tens of microseconds in width. Since this focusing would occur for all dosimetry fielded at a given position and pulse width, this focusing does not cause any dosimetry anomaly. The dose measured with a silicon calorimeter tracks the photocurrent integral for a highly damaged silicon device. A brief consideration of the mechanisms of ionizing energy deposition in silicon identifies no reason to expect anomalous response in this electron energy regime. The characterization of the silicon calorimeter performed here suggests that the uncertainty in the dose measured using the calorimeters is no more than about ±6% for most applications, increasing to +6/-13% when doses greater than 1Mrad(Si) are being measured rapidly because of the assumption of a constant dose/voltage relationship. Noise introduces an error of ±30 rad(Si).

3.3 Dosimetry Using Calcium Fluoride TLDs

3.3.1 Comparison of SNL TLDs and SVIC TLDs

Calcium fluoride TLDs that were provided and read by the SVIC at Little Mountain and SNL's Radiation Metrology Laboratory were fielded on seven pairs of shots. All of these were taken with the accelerator tuned to produce a nominal 19 MeV beam. At each position, 5 TLDs were fielded in the aluminum TLD holder, as shown in Figure 18 (note – all dimensions are inches), with one TLD on axis and the other 4 located up, down, left, and right, at a center to center distance of 0.33 cm (0.120 in). These shot sequences were done at the nominal 1E9 and 3E9 positions, as measured with the silicon calorimeter, using pulse widths of 1, 5, 20, and 50 microseconds (the 50 microsecond shot was performed only at the 3E9 position).

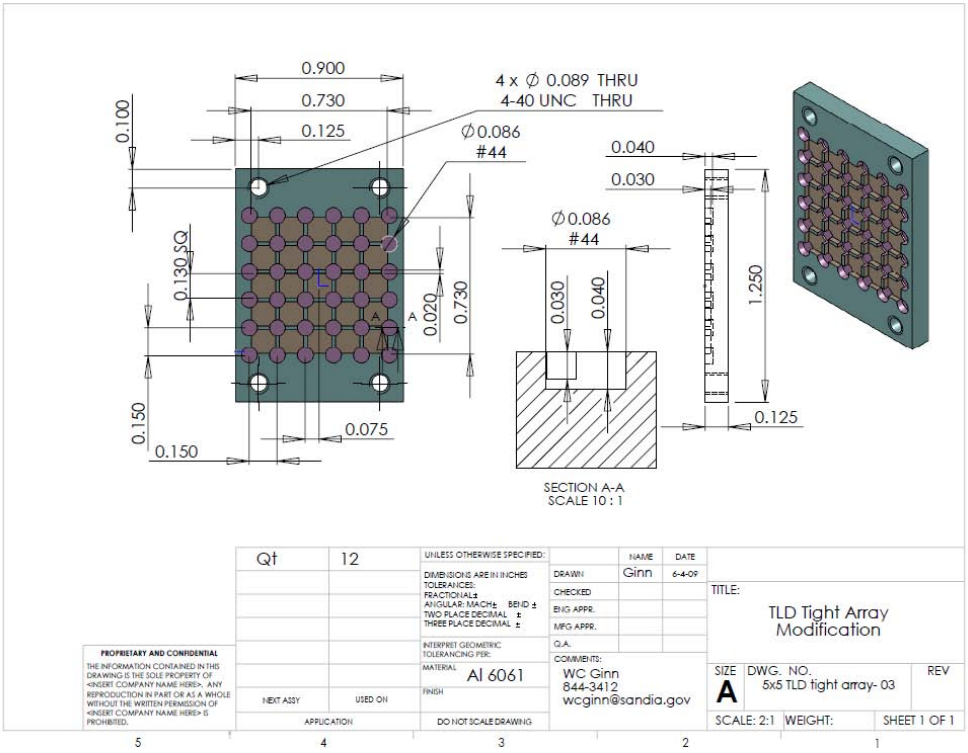

Figure 18: TLD Holder

The results are shown in the Figure 19. The error bars reflect the variation in the measurements, and include no consideration of possible calibration error. The trend is not strong enough to conclude that there is a systematic difference in the calibration between the two sets of TLDs. It does however suggest that there are potential variations in calibration of TLDs that may sometimes lead to variations in measured dose approaching 20%.

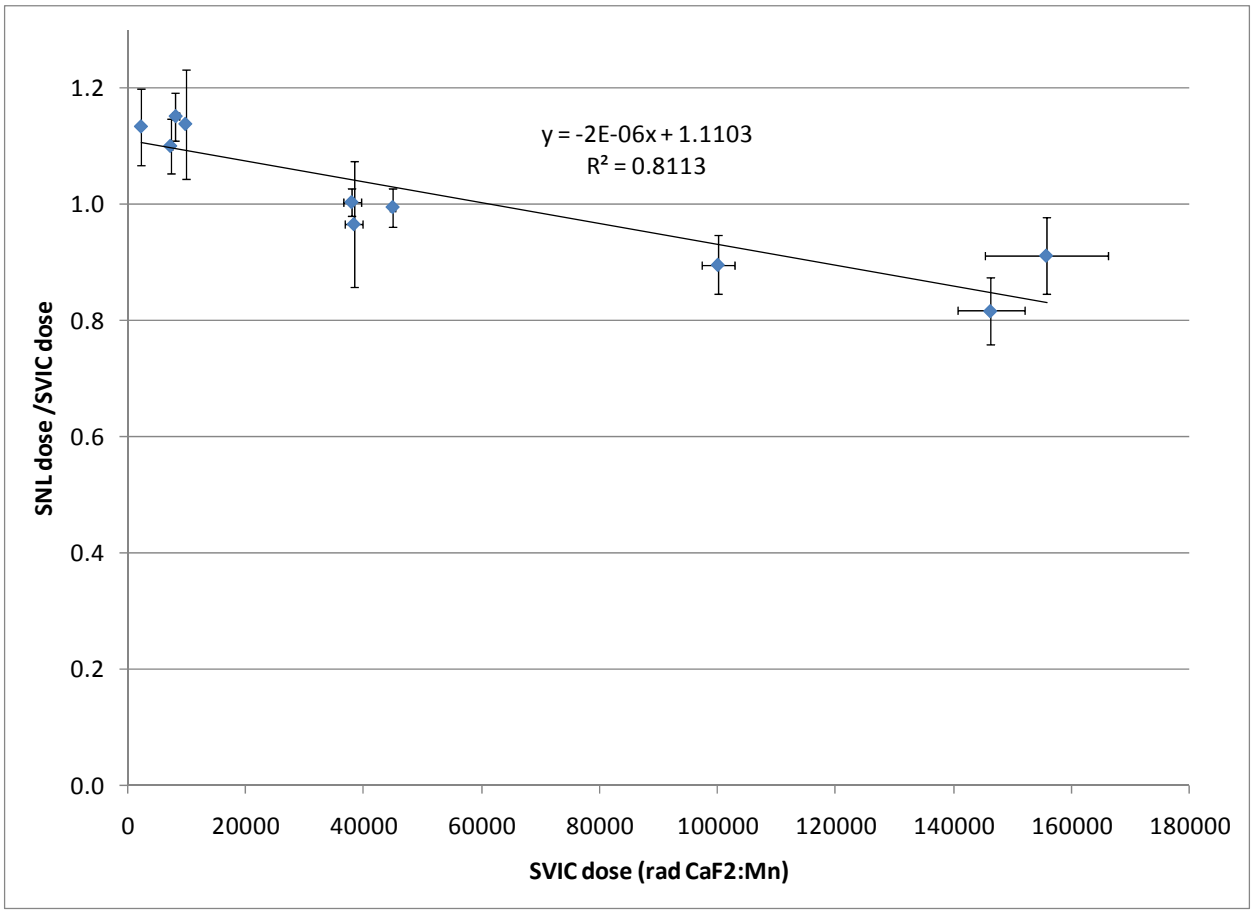

Figure 19: Comparison of SNL and SVIC Measured TLD Dose

3.3.2 Dependence on TLD Housing

To examine the effect of the TLD housing on the observed doses, a series of shots were taken using SNL TLDs in which 5 TLDs were exposed in an array as described above and 5 TLDs were exposed in a calorimeter housing. The TLDs are embedded in a low density polystyrene foam, with a front thickness of 30 mil (0.075 cm) and a rear thickness of about 1 mm. Four TLDs were located in the up, down, left, and right positions, with spacing as in the array. The center was reserved for an alanine dosimeter. The alanine results are discussed in a later section.

During the same shot sequence described for the comparison of the SVIC and SNL TLDs, the ratio of the SNL TLD dose as exposed in the calorimeter housing and the SNL TLD dose as exposed in the array was measured. The results are shown in Figure 20. The vertical error bars are the standard deviation of the measured ratio based on the standard deviation of the dose in the calorimeter housing, while the horizontal error bars are the standard deviation of the array measurements. Neither set of error bars reflects calibration uncertainty. The results are consistent with no effect of the difference in housing on the measured dose, so in the remainder of the analysis the effect of housing the TLDs in the array instead of the calorimeter housing is assumed to be insignificant.

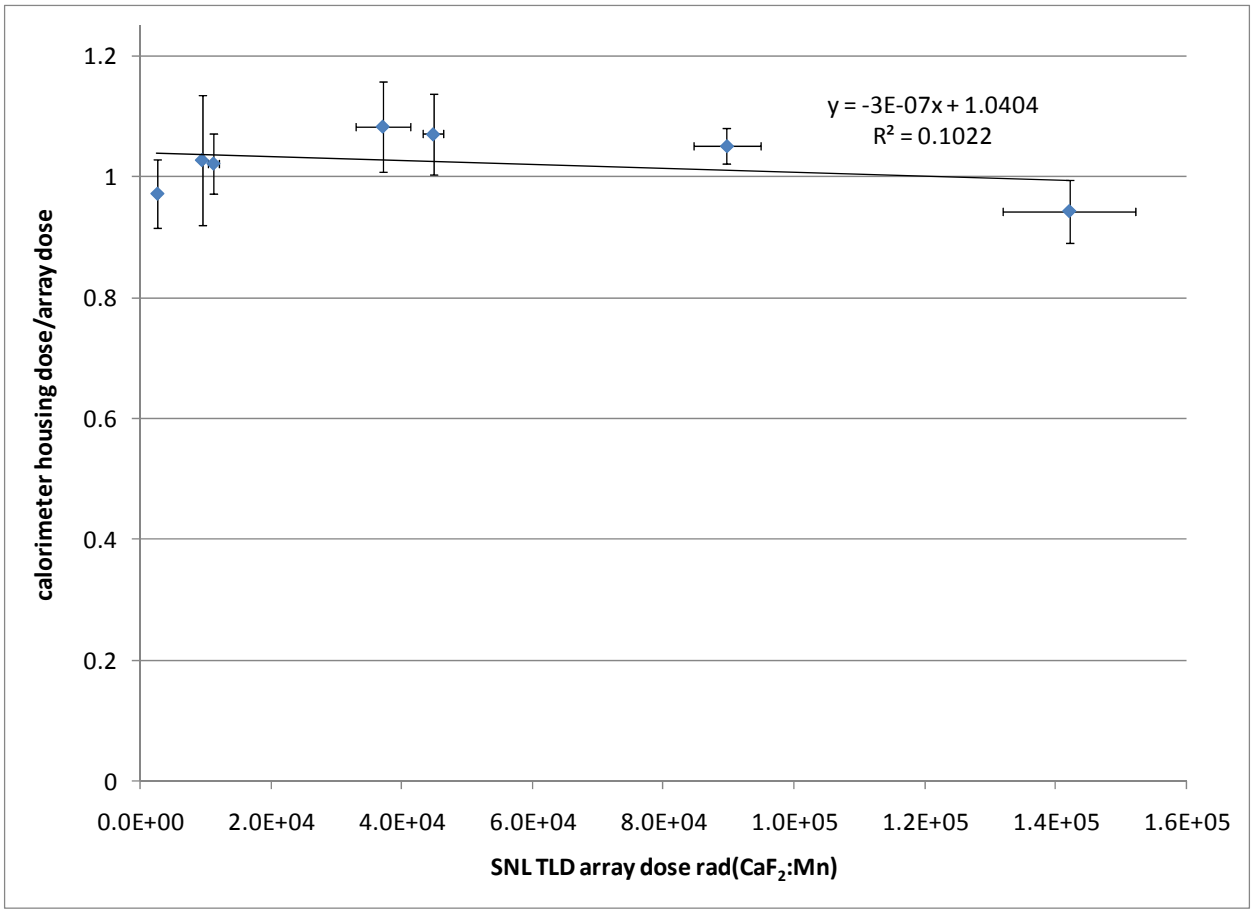

Figure 20: Ratio of Calorimeter Housing Dose to Array Dose

3.3.3 Dose-Distance Scaling for TLDs

To evaluate the consistency of the TLD measurements with the expected $1/r^2$ behavior of a point source, scans of TLD dose vs. distance were for nominal pulse widths of 1, 5, and 50 microseconds for a thin scatter plate (.125) and at a single pulse width for a thick scatter plate (.313). The results are shown in Figures 21 and 22 below. These show that the falloff with distance does not track $1/r^2$, as it should if there were not dose-dependent anomalies in the TLD response, and the discrepancy is largest at the largest doses.

The results for CaF_2:Mn TLDs taken with a thick (.313 inch) aluminum scatter plate on the LINAC output are shown in Figure 21.

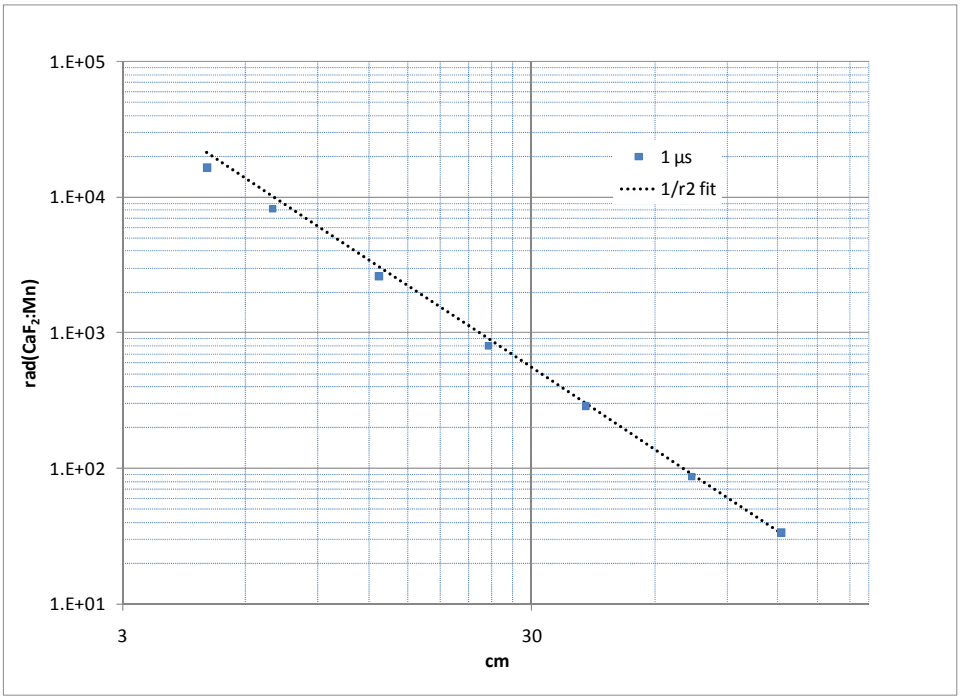

Figure 21: TLD Dose vs. Distance with .313 Inch Scatter Plate

Figure 22 shows TLD data taken with a thin (.125 inch) equilibrator on the LINAC output.

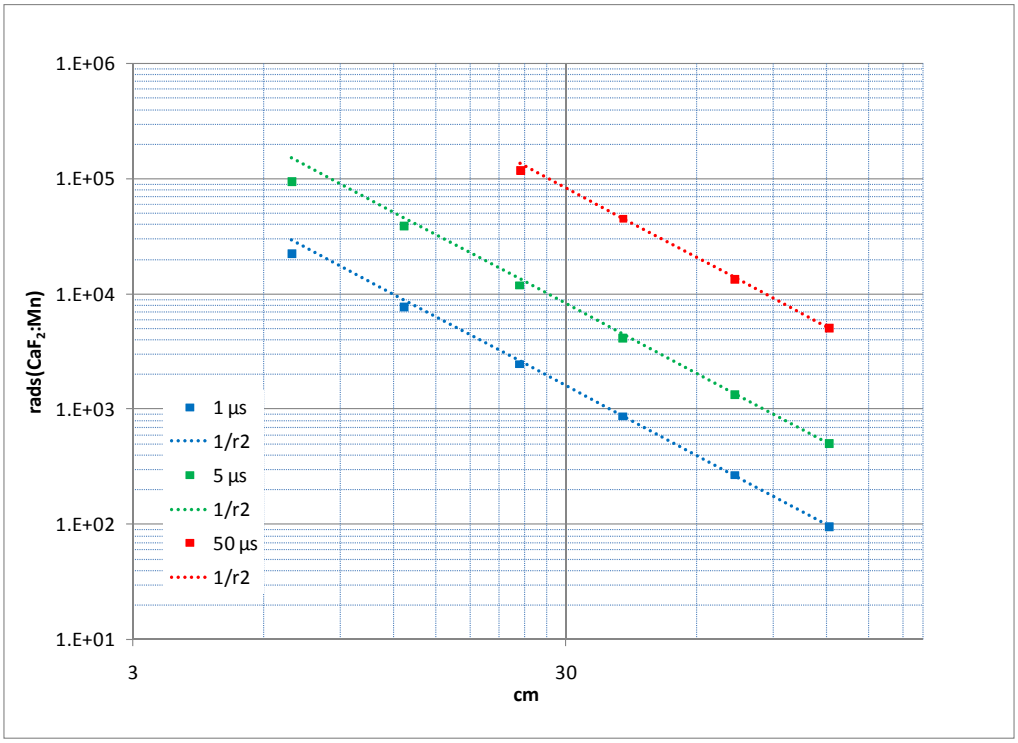

igure 22: TLD Dose vs. Distance with .125 Inch Scatter Plate

3.3.4 Discussion of CaF_2:Mn TLD Results

Comparison of results between two batches of TLDs calibrated at two facilities suggests calibration uncertainties can approach 20% at certain doses, although for the most part they are well within stated uncertainties in TLD dosimetry. No dependence on TLD housing for the housings used in these measurements was found. The dose-distance measurements show a falloff at high doses.

The appendix presents a discussion with references of the physical mechanisms of energy deposition and saturation in CaF_2:Mn. This discussion is summarized here. A consideration of the complex energy deposition mechanisms in CaF_2 identifies no particular reason to expect variation in the response to different types of ionizing radiation. However, the known saturation behavior of CaF_2:Mn TLDs, along with consideration of the behavior of high LET particles in CaF_2:Mn, suggest there may be a possible mechanism for CaF_2:Mn TLDs to approach saturation at lower dose in a 19 MeV electron beam than in a Co-60 gamma radiation field.

3.4 Relationship between Silicon Dose and TLD Dose

To evaluate the relationship between silicon dose and TLD dose, silicon calorimeters and SVIC TLDs mounted in arrays as described above were exposed to a variety of conditions as shown below. It should be noted that the ratio of the stopping powers would suggest that dose ratio rad(CaF_2:Mn)/rad(Si) should be 0.96 at 10 MeV and 0.97 at 20 MeV.

Test condition	Beam voltage	Dose rate (rads(Si)/s)	Pulse width (microseconds)	Dose (rads(Si))
Values	19 MV, 10 MV	1E8 - 5E10	1 - 50	1E2 – 2E5

3.4.1 Dose Dependence of TLD/Calorimeter Ratio

Figure 23 provides an aggregate view of all the shots at 19 MeV under the range of conditions shown above. The indicated uncertainties reflect the calorimeter uncertainty noted above and the standard deviation in the TLD measurements. Note that the uncertainties are large at low doses because of the calorimeter uncertainty. The ratio of TLD dose to calorimeter dose appears to be primarily dependent on dose within this range of parameters. Based on the spectrum-weighted tabulated collisional stopping power, one would expect the ratio of the TLD dose to the calorimeter dose to be 0.966. ITS calculations using the ACCEPT code, the measured MEDUSA spectrum, and the scatter plate used in these experiments gives a ratio of 0.95 ± 0.07. Most values of the ratio using the uncorrected TLD dose lie below the expected value, in the range 0.75-0.9 out to about 50 krad, after which it appears to drop.

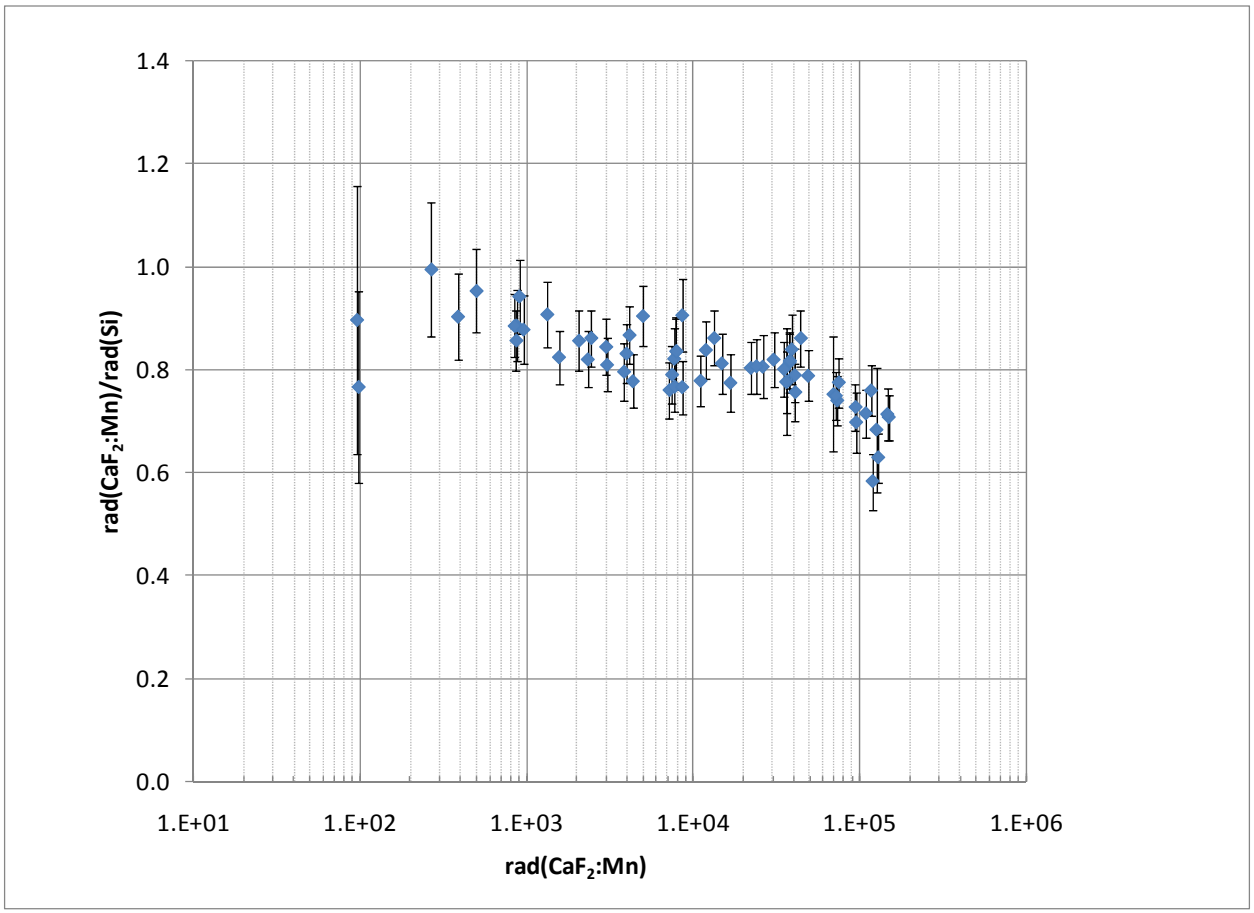

Figure 23: Ratio of CaF_2:Mn Dose to Silicon Calorimeter versus Dose at 19 MeV

Figure 24 shows the same information for the 10 MeV mode shots. The data are too sparse to show a clear trend, but the results are consistent with the 19 MeV mode results.

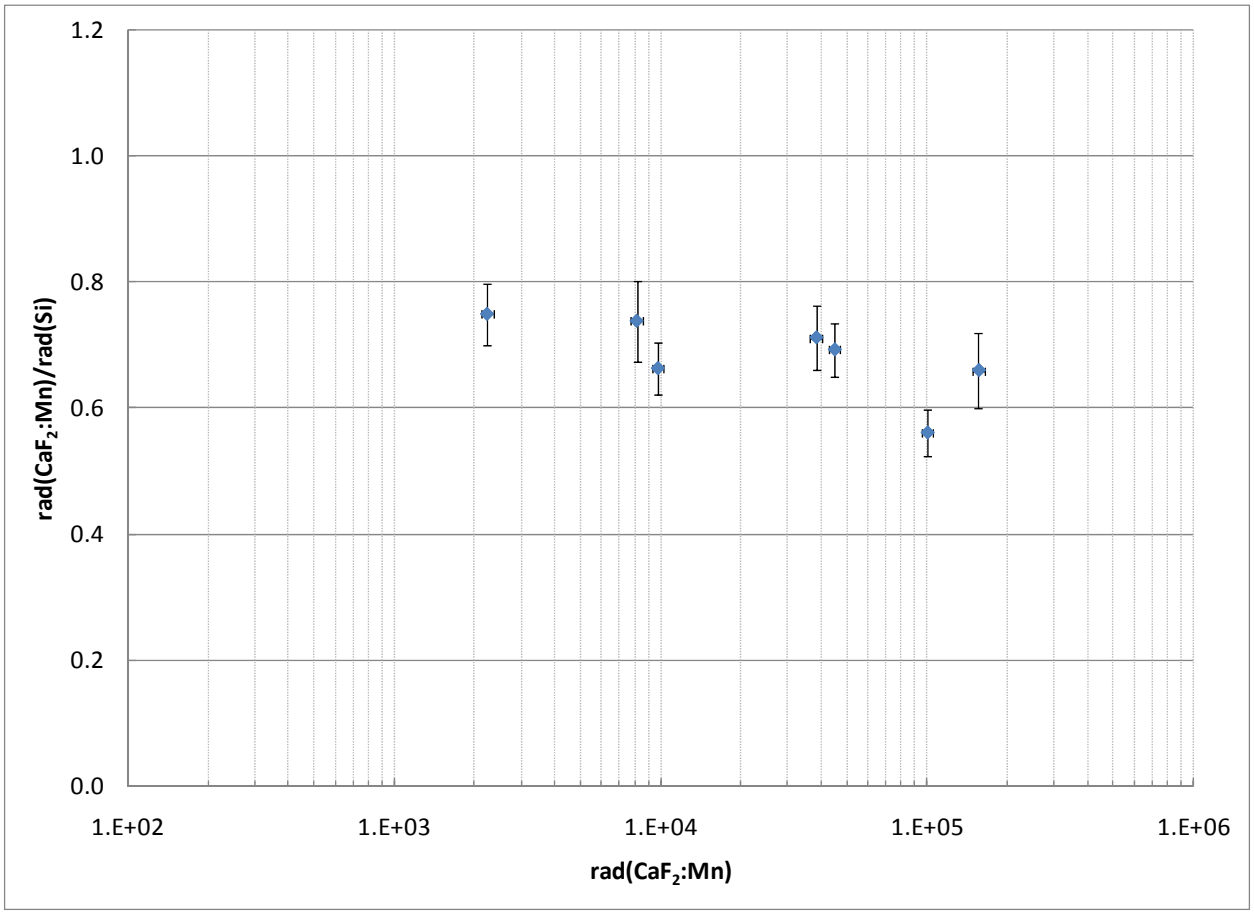

Figure 24: Ratio of CaF_2:Mn Dose to Silicon Calorimeter versus Dose at 10 MeV

3.4.2 Pulse Width Dependence of TLD/Calorimeter Ratio

Previous experiments have suggested a dependence of the measured ratio on pulse width. Figure 25 shows the ratio TLD dose/ Si calorimeter dose vs. pulse width in seconds for a series of dose rates in rad(Si)/s. These are nominal dose rates (varying from 1E8 to 5E10 rad(Si)/s) based on the silicon dose rate at the 1 microsecond pulse width. For each shot sequence, the position was fixed and the pulse width was varied.

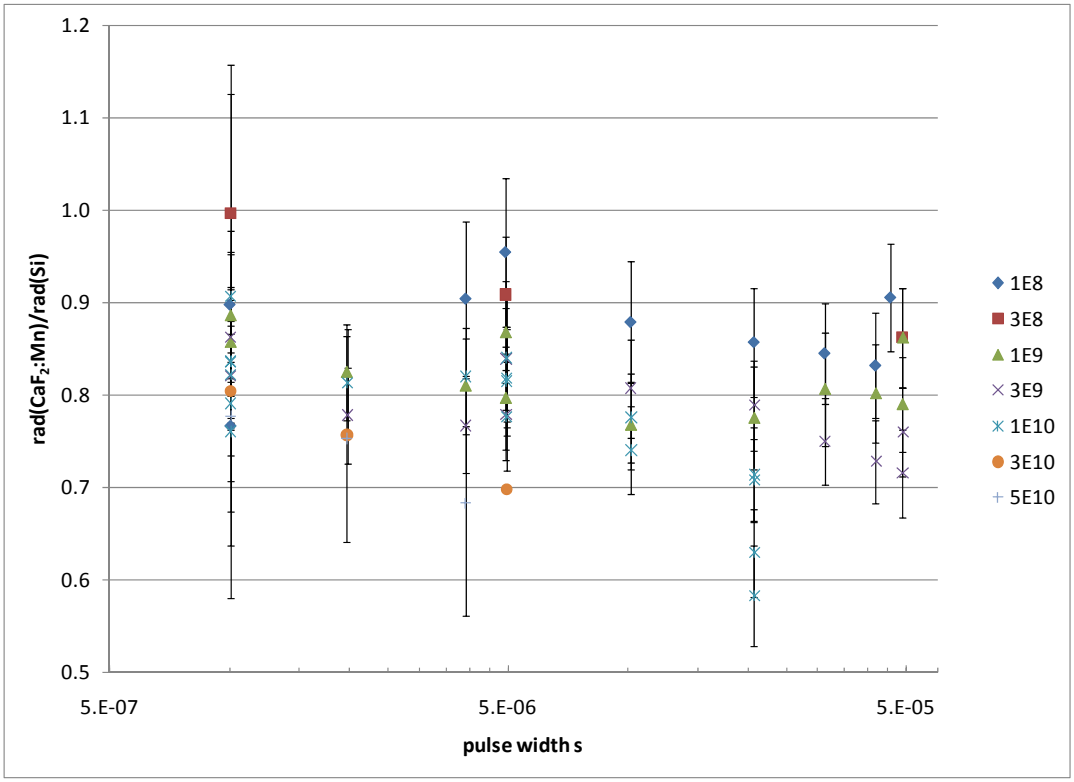

Figure 25: TLD Dose / Si Calorimeter Dose vs. Pulse Width in Seconds for Dose Rate Ranging from 1E8 to 5E10 rad(Si)

Inspection of these results suggests that there is not a consistent trend with pulse width.

Figure 26 shows the same data for MEDUSA tuned to operate in the 10 MeV mode The data are much more limited. Although the slope is suggestive the data are still consistent with no dependence of the dose ratio on the pulse width. They indicate that the dose discrepancy under this set of test conditions may be greater for the 10 MeV mode than for the 19 MeV mode. As noted earlier, the ratio of the stopping power of the TLDs to that of silicon should be 0.96.

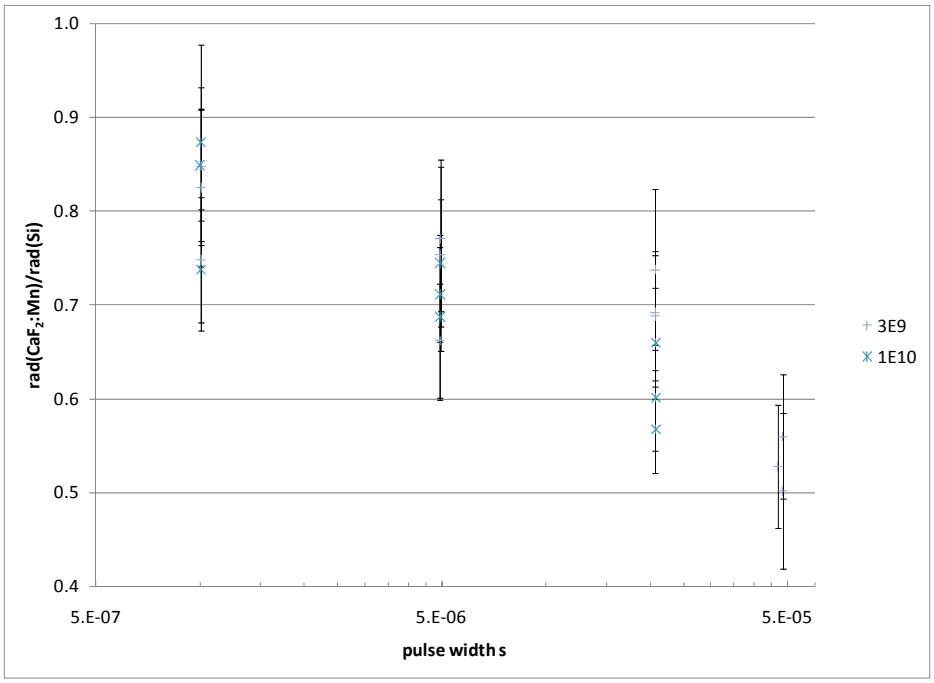

Figure 26: Ratio of CaF2:Mn Dose to Si Calorimeter Dose vs. Pulse Width in Seconds for Dose Rate Ranging from 3E9 to 1E10 rad(Si)

3.5 Dosimetry using MOSFET Threshold Voltage Shift to Characterize Dose

3.5.1 Introduction

The objective of the MOSFET tests was to characterize discrepancies in dosimetry between silicon calorimeter and MOSFET total ionizing dose measurements. The method was to measure the MOSFET threshold voltage shifts at MEDUSA and convert these measurements to equivalent dose using calibration factors based on moderate dose rate x-ray irradiations.

3.5.2 Experiment Description

The LINAC irradiations were performed on the MEDUSA accelerator at Hill Air Force Base using 20 and 10 MeV (nominal) electrons. An aluminum scatter plate 0.125 inch thick at the beam exit port was used. Devices were measured at dose rates ranging from 2E9 to 5E10 rad(Si)/s. Pulse widths ranged from 1 to 49 microseconds. The measurements were made during two experimental campaigns in August and September, 2009. Silicon calorimeters were used to characterize the LINAC dose.

The x-ray calibration irradiations were performed at Sandia using a 10 keV x-ray source at a dose rate of 1667 rad(SiO_2)/s, so the irradiation time to obtain a dose of 1 Mrad(SiO_2) is approximately 10 minutes.

The MOSFETs were fabricated at Sandia in the 1980s using the 4/3 µm technology. Gate oxide thicknesses of 48 and 65 nm were used. LINAC tests at the Boeing Physical Science Center's LINAC and x-ray tests at Sandia of these devices in the 1990s showed good correlation in MOSFET voltage shifts at equivalent times after irradiation. The 48 nm devices were tested in August 2009 and the 65 nm devices were tested in September 2009.

The devices used for these tests (Figure 27) were fabricated in the 1980s using Sandia's 4/3 µm technology. The process lot was G1928A. The radiation-induced degradation of transistors from this process lot has been investigated extensively in the past. Two wafers from this lot were tested. W11 transistors have an oxide thickness of 65 nm and W44 transistors have an oxide thickness of 48 nm. These transistors were processed in a full IC process. The transistors were packaged in 24-pin DIP packages using the TA629 DCT bondout. The layout of the G1928A die and the package pinout are given in figure 27. For reference, the size of the bond pads is 100 µm x 100 µm. P-channel and n-channel transistors were tested. Three sizes of transistors were tested. The gate length and gate widths of these transistors are 16 µm x 3 µm, 16 µm x 4 µm and 100 µm x 10 µm.

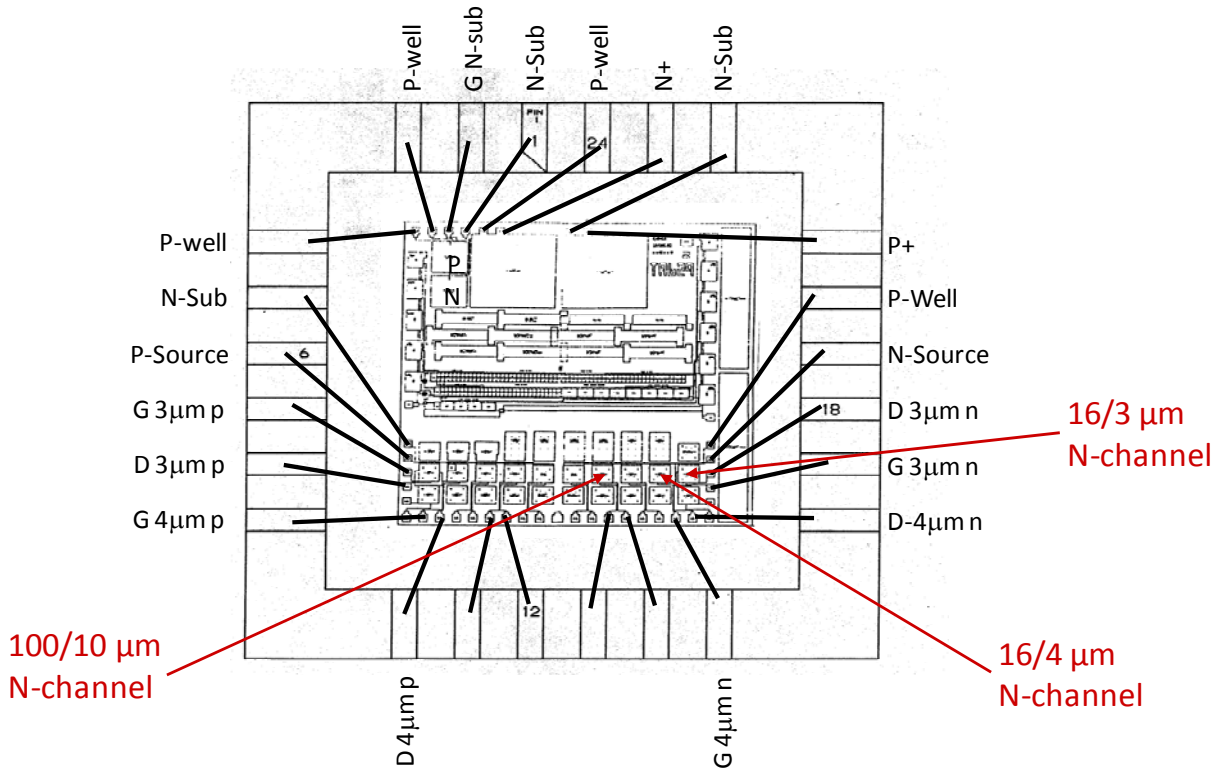

Figure 27: Layout of the G1928A Die and the Package Pinout

3.5.3 X-Ray Test Results

3.5.3.1 X-Ray N-Channel Transistor Tests Yield Expected Results

The transistors were irradiated and characterized for the threshold voltage, threshold voltage shift, ΔV_{th}, threshold voltage shift due to oxide trapped charge, ΔV_{ot}, and threshold voltage shift due to interface trap charge, ΔV_{it}. Oxide-trapped charge (e.g., positively charge holes) is radiation-induced

charge trapped in the oxide. Interface-trap charge is due to the generation of radiation-induced interface traps at the Si/SiO_2 interface. Interface-trap charge is predominantly negatively charged for an n-channel transistor and positively charged for a p-channel transistor. For either an n-channel or p-channel transistor, $\Delta V_{th} = \Delta V_{ot} + \Delta V_{it}$. Thus, for an n-channel transistor ΔV_{ot} and ΔV_{it} compensate each other and for a p-channel transistor ΔV_{ot} and ΔV_{it} add together. The time scales for the buildup and neutralization of oxide-trapped charge and interface-trap charge are considerably different. For oxide-trapped charge, ΔV_{ot} is at maximum immediately after irradiation and can neutralize with time after irradiation. ΔV_{it} can take thousands of seconds after irradiation to reach its maximum value and does not readily anneal or neutralize at room temperature. Because the total threshold voltage shift is due to both oxide-trapped and interface-trap charge, these two charges compensate each other for an n-channel transistor, and these two charges have different time scales for buildup and anneal, in almost all of the characterizations, we use either ΔV_{ot} or ΔV_{it}, and in most cases ΔV_{ot}. As will be shown below, as long as the total radiation plus anneal time is the same, ΔV_{ot} can be quantitatively compared for widely different radiation sources. In the Figure 28, ΔV_{ot} is plotted versus total ionizing dose for W44 n-channel transistors irradiated using a 10-keV x-ray source at Sandia at a dose rate of 1667 rad(SiO_2)/s. Data are shown for the three different sizes of n-channel transistors. The transistors were irradiated with an oxide electric field (pre-irradiation) of 2 MV/cm. As for all irradiations in this work, a bias voltage was applied to the gate of the transistor and the source, drain, and substrate were grounded during irradiation. Data are shown for a single transistor (i.e., the transistor was irradiated in steps and characterized after each step).

As is apparent in Figure 28, there is no substantial difference in ΔV_{ot} versus transistor size for total ionizing dose levels up to 2 Mrad(SiO_2). This is typical of transistors from this wafer. The difference in ΔV_{ot} is negligible for different sizes of transistors.

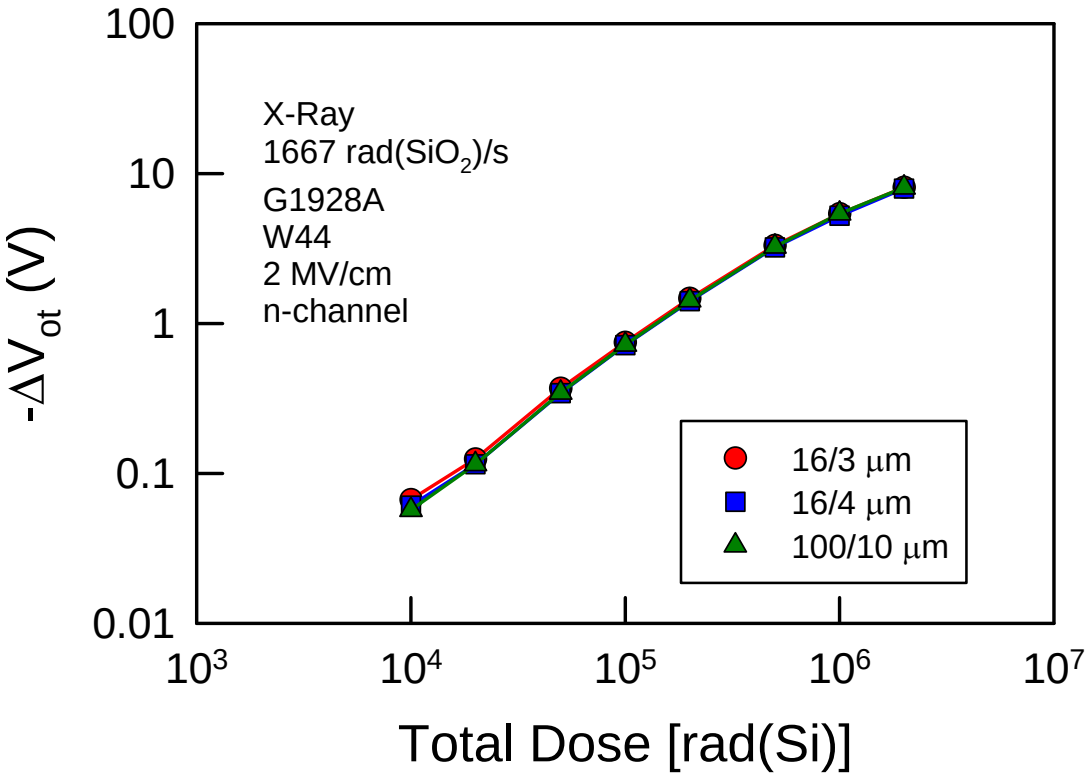

Figure 28: Voltage Shift vs. X-Ray Total Dose for Three Sizes of 48-nm Gate Oxide N-channel Transistors

3.5.3.2 X-Ray P-Channel Transistor Tests Also Yield Expected Results

In the Figure 29, ΔV_{ot} is plotted versus total ionizing dose for W44 p-channel transistors irradiated using a 10-keV x-ray source at Sandia at a dose rate of 1667 rad(SiO_2)/s. Data are shown for the three different sizes of p-channel transistors. The transistors were irradiated with an oxide electric field (pre-irradiation) of 2 MV/cm. Data are shown for a single transistor (i.e., the transistor was irradiated in steps and characterized after each step). As is apparent in Figure 29, there is no substantial difference in ΔV_{ot} versus transistor size for total ionizing dose levels up to 2 Mrad(SiO_2) similar to that for the n-channel transistors. This is typical of transistors from this wafer. Once again, the difference in ΔV_{ot} is negligible for different sizes of transistors.

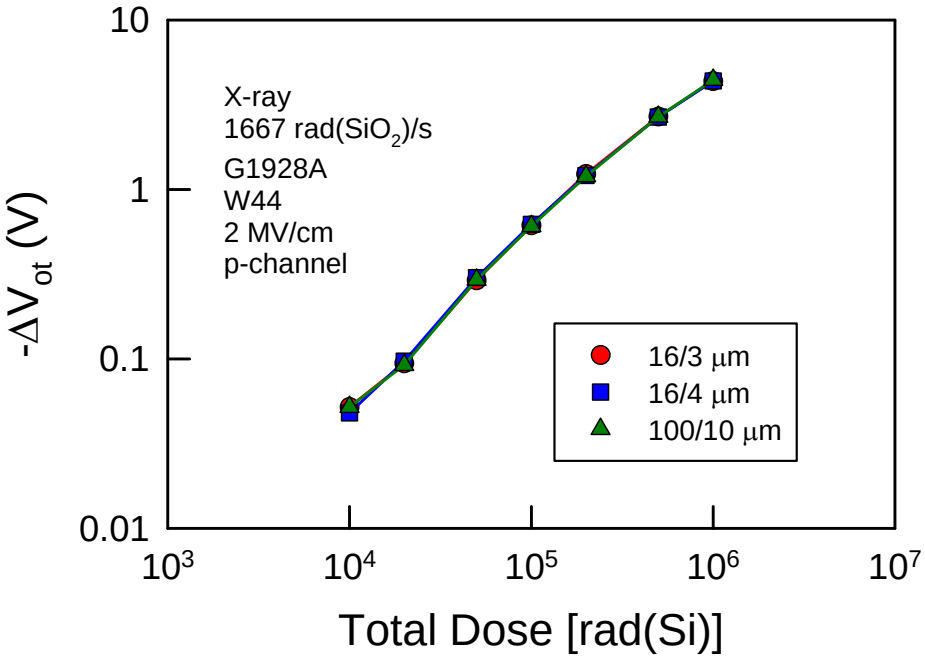

Figure 29: Voltage Shift vs. X-Ray Total Dose for Three Sizes of 48-nm Gate Oxide P-channel Transistors

3.5.3.3 Correlation between ΔV_{ot} for N- and P-Channel Transistors Observed

In Figure 30, ΔV_{ot} is plotted for 16 x 3 µm n- and p-channel transistors. The data were taken from the previous two figures. There is very little difference between ΔV_{ot} for the n- and p-channel transistors. Again, this is the typical (expected) response for this technology. Also, based on the physics of charge buildup, there should be very little difference in ΔV_{ot} for n- and p-channel transistors. (This is not necessarily true for ΔV_{it}.) These data show that the x-ray radiation-induced degradation of these transistors is well behaved (there are no abnormalities in the response).

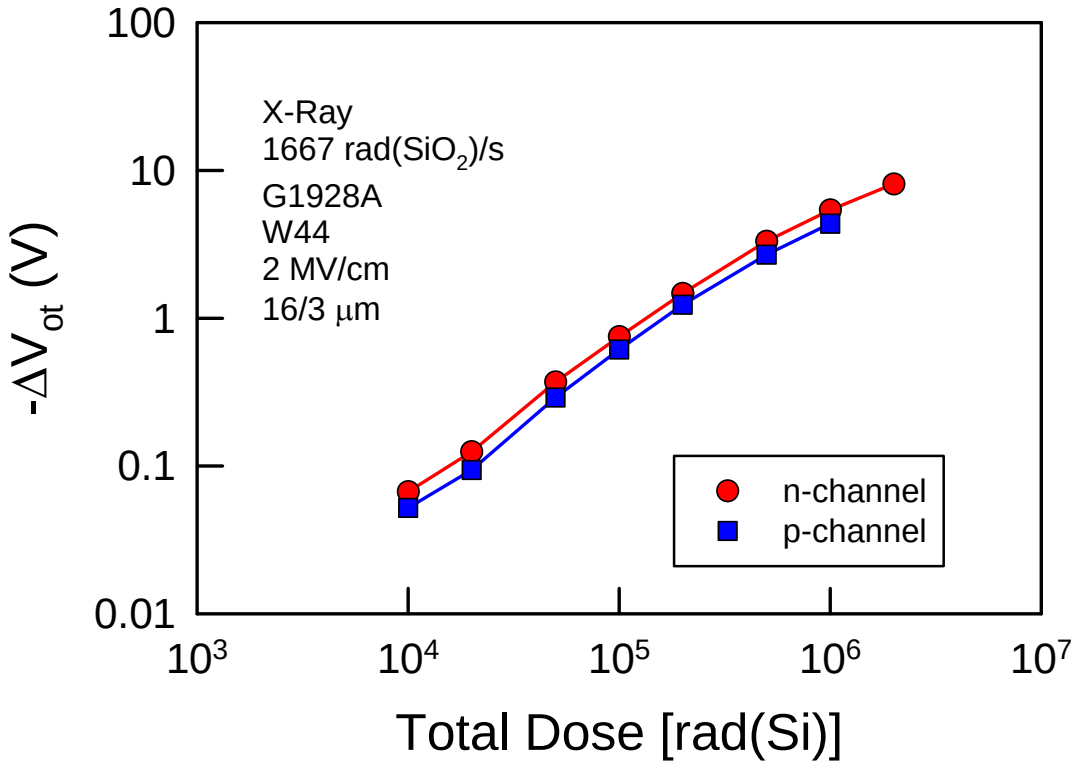

Figure 30: Comparison of Voltage Shift vs. X-Ray Total Dose for One Size of 48-nm Gate Oxide P- and N-channel Transistors

3.5.4 LINAC Test Results: Comparison of N- and P-Channel Transistor Voltage Shifts for Different Sizes of Transistors

3.5.4.1 LINAC N-Channel Transistor Tests Yield Expected Results at the Lowest Dose Rate

Transistors from the same wafer were irradiated at the Hill Air Force Base electron linear accelerator (LINAC) with 19 MeV electrons. Whereas the x-ray irradiations were at a relatively low dose rate, the LINAC irradiations were at a very high dose rate in a single pulse of electrons.

For Figure 31, n-channel transistors were irradiated at a dose rate of $3x10^9$ rad(Si)/s. Data are shown for the three different sizes of transistors. The data were taken immediately after irradiation. The total ionizing dose per pulse was varied by changing the pulse width (from 1 to 50 µs). These data are for n-channel transistors irradiated with an oxide electric field of 2 MV/cm. Each total ionizing dose level is for a different (non-irradiated) transistor. The variation in ΔV_{ot} for the three different sizes of transistors is <0.1V. (Note that for this dose rate, for the smaller total ionizing dose levels, ΔV_{ot} is relatively small (~0.1 V or less). A 0.01 or 0.02 V variation in ΔV_{ot} is not unlikely.) While observed differences in ΔV_{ot} between different sizes of transistors are larger than observed for x-ray irradiation, the differences are still relatively small (<0.1 V) at this low dose rate.

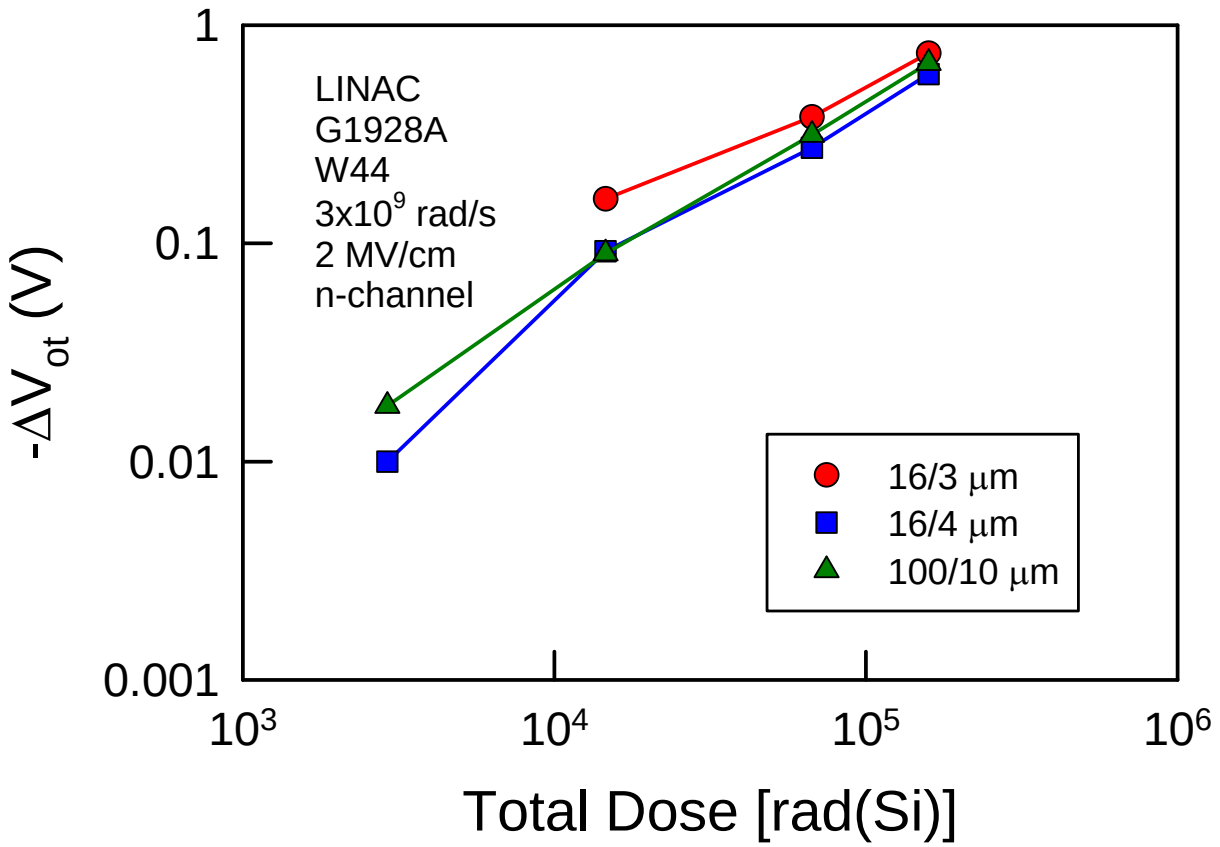

Figure 31: ΔV_{ot} vs. LINAC Dose (Measured using Silicon Calorimeters) for Three Sizes of 48-nm Gate Oxide N-channel Transistors at 3E9 rad(Si)/s

3.5.4.2 LINAC P-Channel Transistor Tests Yield Expected Results at the Lowest Dose Rate

For Figure 32, p-channel transistors were irradiated at a dose rate of $3x10^9$ rad(Si)/s. Data are shown for the three different sizes of transistors. The total ionizing dose per pulse was varied by changing the pulse width (from 1 to 50 µs). These data are for p-channel transistors irradiated with an oxide electric field of 2 MV/cm. The data were taken immediately after irradiation. Each total ionizing dose level is for a different (non-irradiated) transistor. The variation in ΔV_{ot} for the three different sizes of transistors is <0.02V. (Note that for this dose rate, for the smaller total ionizing dose levels, ΔV_{ot} is relatively small (~0.1 V or less). A 0.01 or 0.02 V variation in ΔV_{ot} is not unlikely.) Good agreement in ΔV_{ot} is observed for different sizes of transistors (<0.02 V difference).

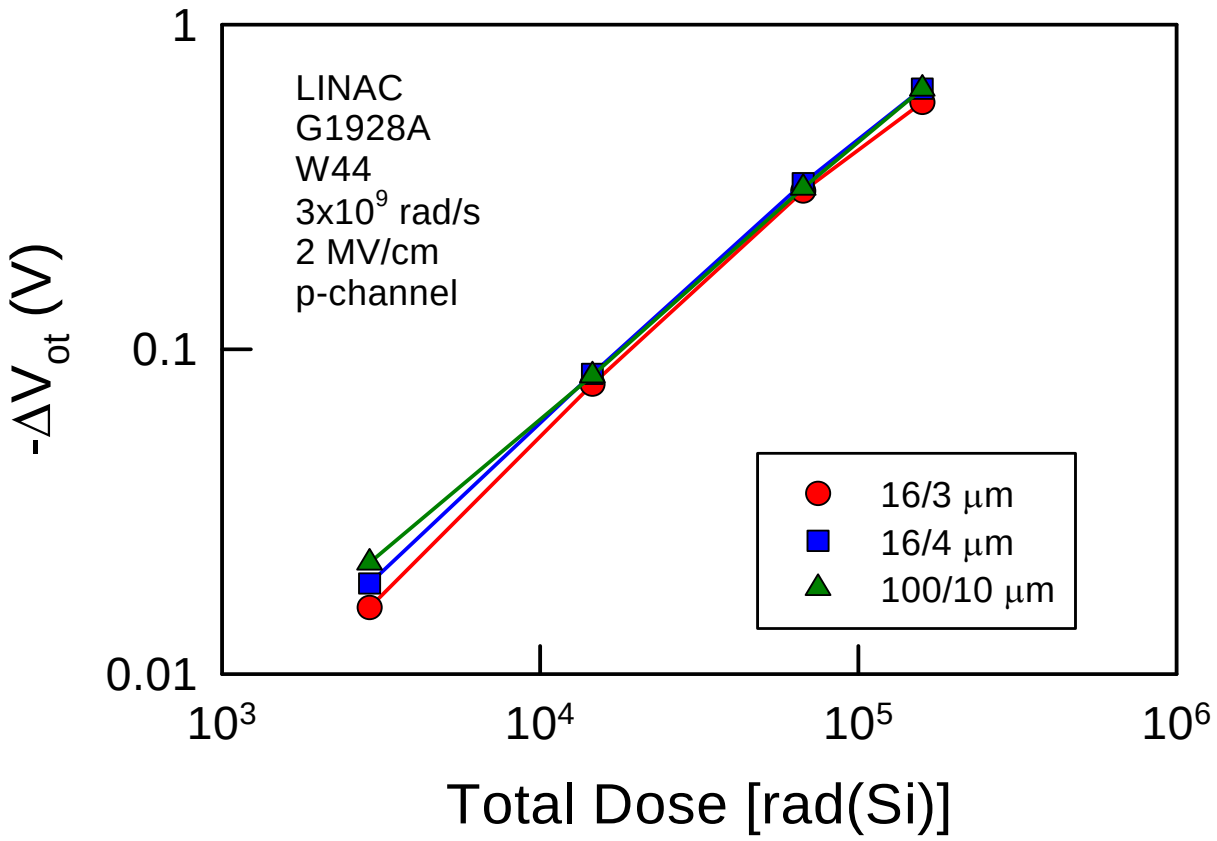

Figure 32: ΔV_{ot} vs. LINAC Dose (Measured using Silicon Calorimeters) for Three Sizes of 48-nm Gate Oxide P-channel Transistors at 3E9 rad(Si)/s

3.5.4.3 LINAC N-Channel Transistor Tests Yield Expected Results at Intermediate Dose Rate

For Figure 33, n-channel transistors were irradiated at a dose rate of $1x10^{10}$ rad(Si)/s. Data are shown for the three different sizes of transistors. The total ionizing dose per pulse was varied by changing the pulse width (from 1 to 50 µs). These data are for n-channel transistors irradiated with an oxide electric field of 2 MV/cm. The data were taken immediately after irradiation. Each total ionizing dose level is for a different (non-irradiated) transistor. Just as for the lower dose rate, the variation in ΔV_{ot} for the three different sizes of transistors is <0.02. (Note that for this dose rate, for the smaller total ionizing dose levels, ΔV_{ot} is relatively small (~0.1 V or less). A 0.01 or 0.02 V variation in ΔV_{ot} is not unlikely.) Once again, there is good agreement in ΔV_{ot} observed for different sizes of transistors (<0.02 V difference).

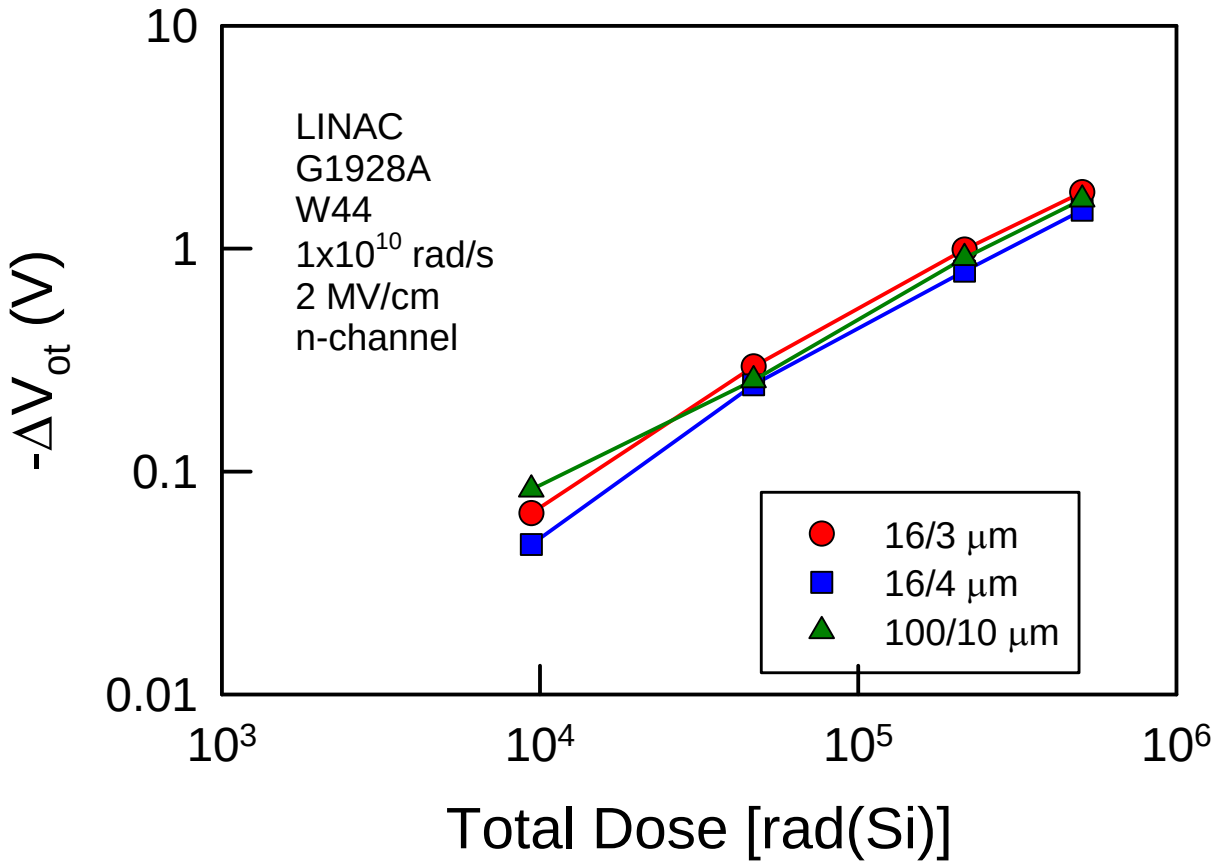

Figure 33: ΔV_{ot} vs. LINAC Dose (Measured using Silicon Calorimeters) for Three Sizes of 48-nm Gate Oxide N-channel Transistors at 1E10 rad(Si)/s

3.5.4.4 LINAC P-Channel Transistor Tests Yield Expected Results at Intermediate Dose Rate

For Figure 34, p-channel transistors were irradiated at a dose rate of $1x10^{10}$ rad(Si)/s. Data are shown for the three different sizes of transistors. The total ionizing dose per pulse was varied by changing the pulse width (from 1 to 50 µs). These data are for p-channel transistors irradiated with an oxide electric field of 2 MV/cm. The data were taken immediately after irradiation. Each total ionizing dose level is for a different (non-irradiated) transistor. Just as for the lower dose rate, the variation in ΔV_{ot} for the three different sizes of transistors is <0.01. (Note that for this dose rate, for the smaller total ionizing dose levels, ΔV_{ot} is relatively small (~0.1 V or less). A 0.01 or 0.02 V variation in ΔV_{ot} is not unlikely.) Good agreement in ΔV_{ot} is observed for different sizes of transistors (<0.01 V difference).

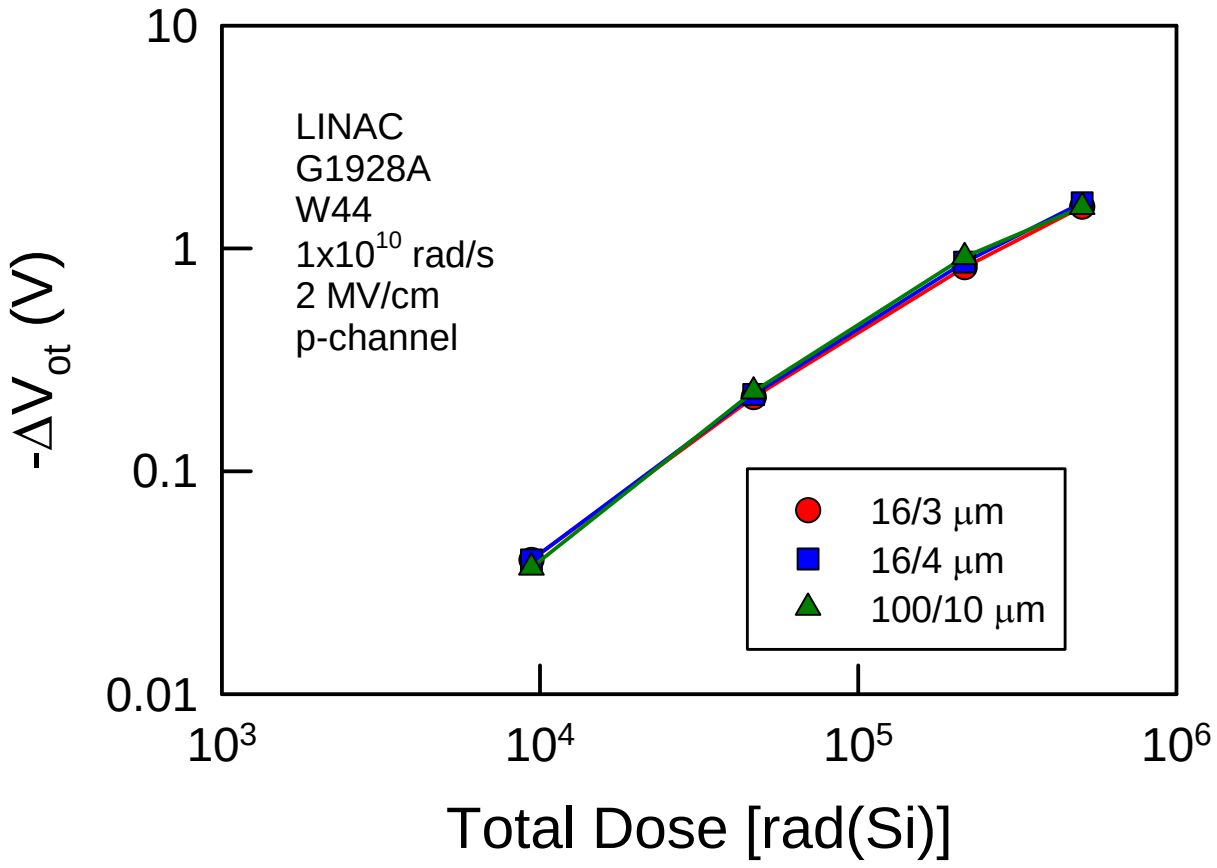

Figure 34: ΔV_{ot} vs. LINAC Dose (Measured using Silicon Calorimeters) for Three Sizes of 48-nm Gate Oxide P-channel Transistors at 1E10 rad(Si)/s

3.5.4.5 Good Correlation in ΔV_{ot} for N- and P-channel Transistors Observed at Intermediate Dose Rate

In Figure 35, ΔV_{ot} is plotted for 16 x 3 µm n- and p-channel transistors. The data were taken from the previous two figures. There is very little difference between ΔV_{ot} for the n- and p-channel transistors. Hence for dose rate pulses of $3x10^9$ and $1x10^{10}$ rad(Si)/s, the behavior of ΔV_{ot} is typical of devices for this technology, just as it was for the x-ray irradiations. There is nothing from the data presented so far to suspect that the x-ray or LINAC data are flawed.

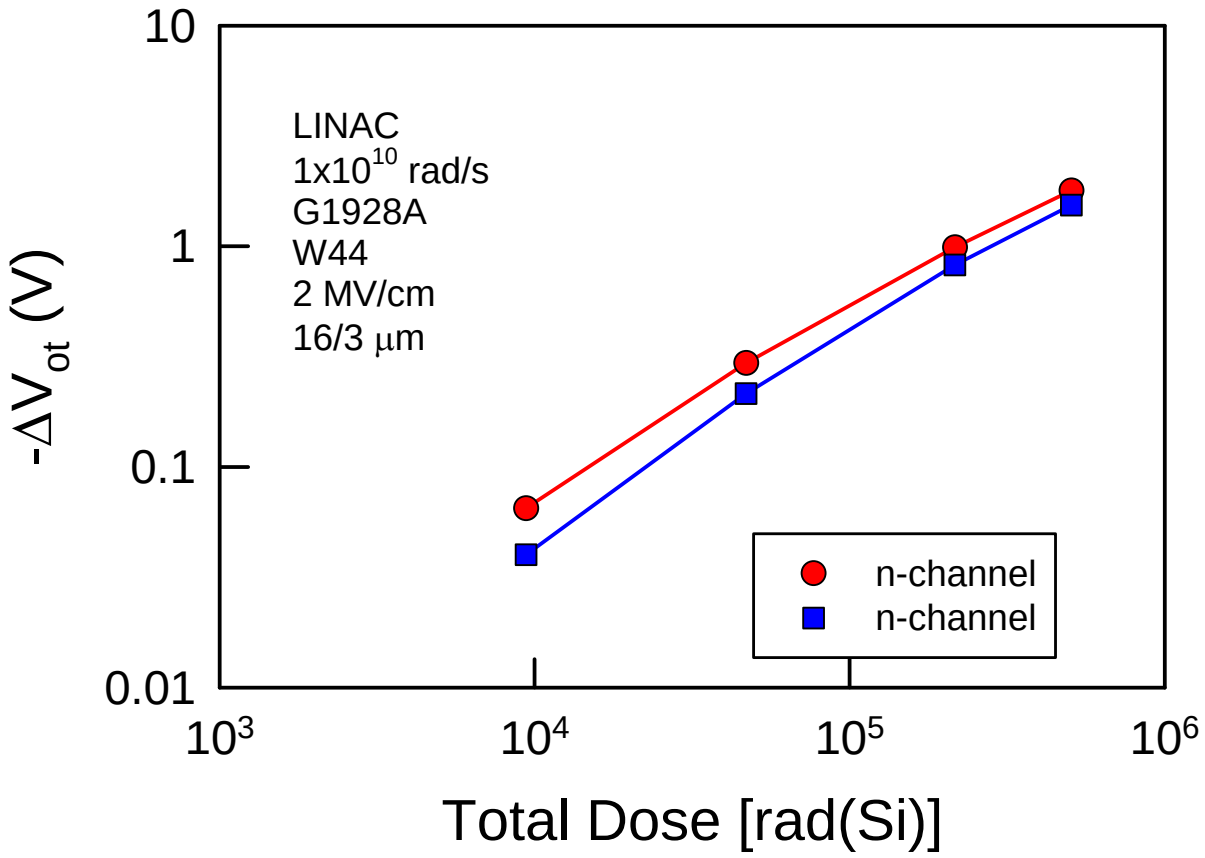

Figure 35: ΔV_{OT} vs. LINAC Total Dose (Measured using Silicon Calorimeters) for One Size of 48-nm Gate Oxide P- and N-channel Transistors at 1E10 rad(Si)/s

3.5.4.6 LINAC N-channel Transistor Tests Yield Expected Results at the Highest Dose Rate

For Figure 36, n-channel transistors were irradiated at a dose rate of 4.6×10^{10} rad(Si)/s. Data are shown for the three different sizes of transistors. The total ionizing dose per pulse was varied by changing the pulse width (from 1 to 50 μs). These data are for n-channel transistors irradiated with an oxide electric field of 2 MV/cm. The data were taken immediately after irradiation. Each total ionizing dose level is for a different (non-irradiated) transistor. Just as for the lower dose rates, the variation in ΔV_{ot} for the three different sizes of transistors is within experimental uncertainty.

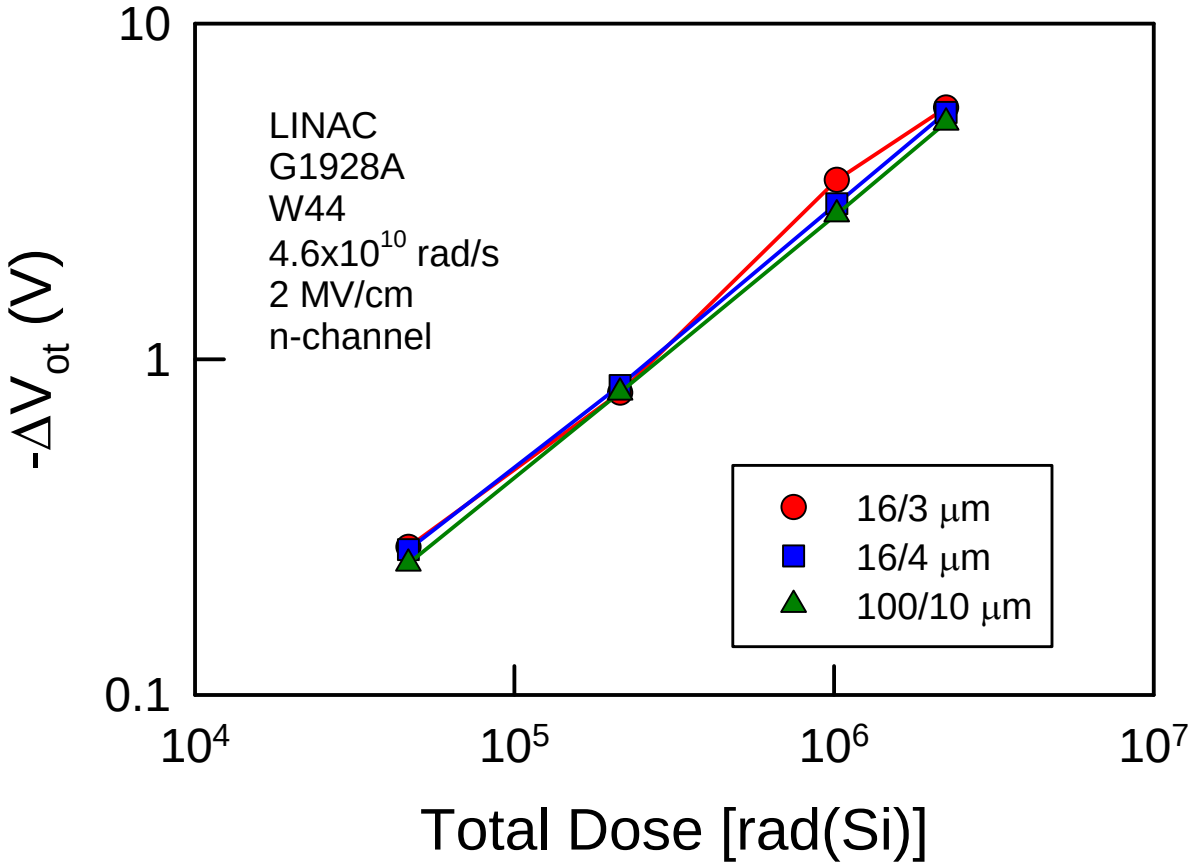

Figure 36: ΔV_{ot} vs. LINAC Dose (Measured using Silicon Calorimeters) for Three Sizes of 48-nm Gate Oxide N-channel Transistors at 4.6E10 rad(Si)/s

3.5.4.7 Large Differences Observed in LINAC P-Channel Transistor Test Results at the Highest Dose Rate

For Figure 37, p-channel transistors were irradiated at a dose rate of 4.6×10^{10} rad(Si)/s. Data are shown for the three different sizes of transistors. The total ionizing dose per pulse was varied by changing the pulse width (from 1 to 50 µs). These data are for p-channel transistors irradiated with an oxide electric field of 2 MV/cm. The data were taken immediately after irradiation. Each total ionizing dose level is for a different (non-irradiated) transistor. Unlike the n-channel data at this dose rate and the n- and p-channel data at lower dose rates, there is a very large difference in ΔV_{ot} for the different size transistors. These data are completely unexpected. Note that the large difference in ΔV_{ot} is independent of total ionizing dose. It occurs at both low and high total ionizing dose levels. Also note that the difference in ΔV_{ot} does not appear to consistently follow the variation in transistor size, i.e., the values for ΔV_{ot} for the smallest and largest transistors are relatively close to each other while the values for ΔV_{ot} for the 16 x 4 µm transistors are considerably less than for the other size transistors. The cause of the large difference is unknown. One possible cause is that there are larger variations in the beam uniformity for the highest dose rate than for the lower dose rates. At the highest dose rate, the transistors were positioned fairly close to the exit port of the beam. This could have resulted in more observable variation in the beam uniformity. A second possible explanation is that the transistors are located at different positions of the die and therefore the inductance and capacitance of the wire bonds, metal lines between the bond pads and the transistors, etc. could be different resulting in a different response of the transistors. In any case, these results indicate that an unknown mechanism has impacted the ΔV_{ot} measurements. Which data set (if any) is the correct response is not known. Why this difference appeared for the p-channel transistors and not the n-channel transistors is also unknown (if it is not purely coincidence).

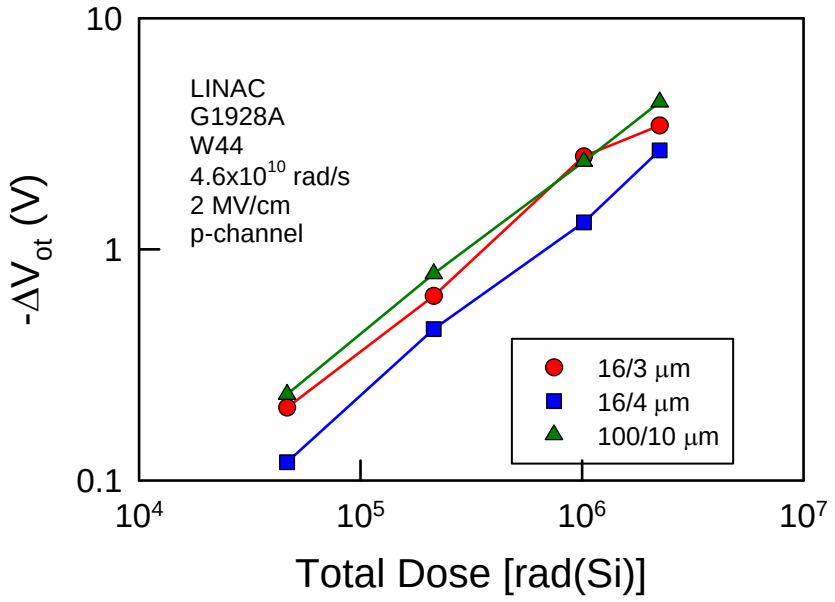

Figure 37: ΔV_{ot} vs. LINAC Dose (Measured using Silicon Calorimeters) for Three Sizes of 48-nm Gate Oxide P-channel Transistors at 4.6E10 rad(Si)/s

3.5.4.8 Poorer Correlation in ΔV_{ot} for N- and P-Channel Transistors observed at the Highest Dose Rate

In Figure 38, ΔV_{ot} is plotted for 16 x 3 µm n- and p-channel transistors. The data were taken from the previous two figures. The difference in ΔV_{ot} for the n- and p-channel transistors is larger than it was for the data taken at lower dose rates, consistent with the previous data at this dose rate. These data raise the possibility of uncertainties in the radiation results taken at MEDUSA at high dose rates, not just for these devices, but possibly for all devices.

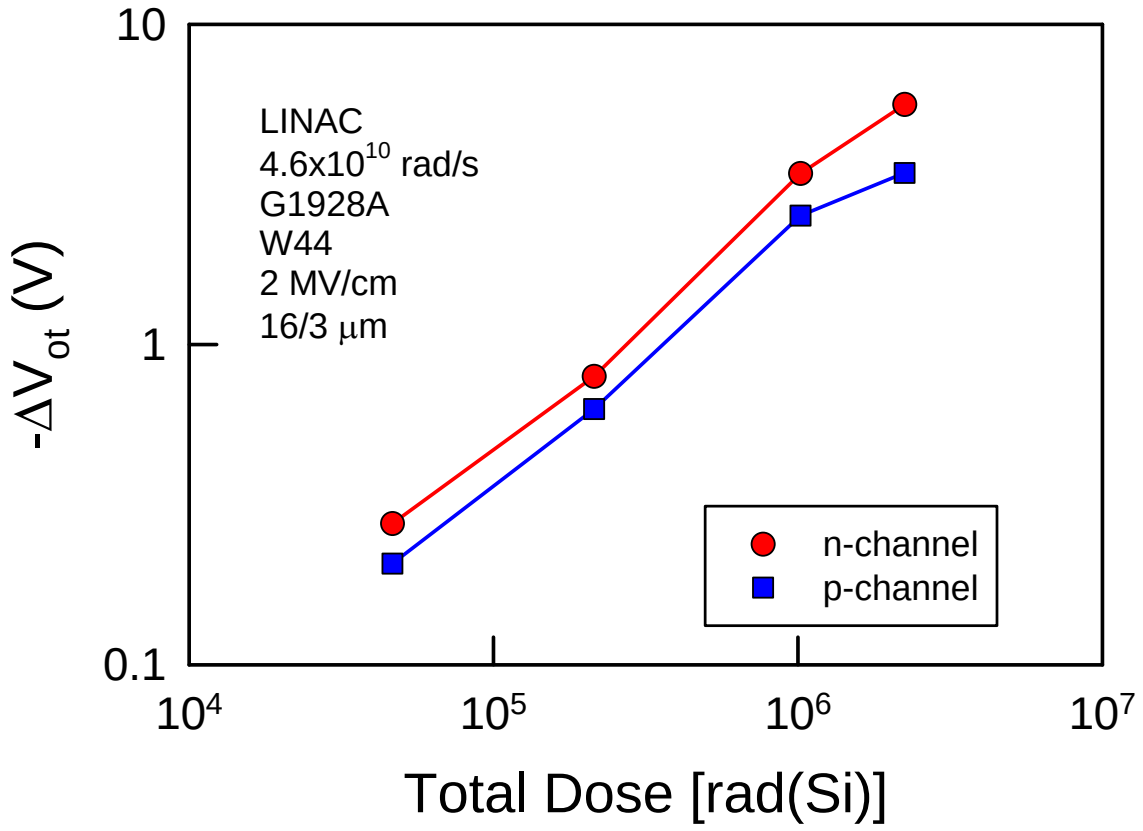

Figure 38: ΔV_{OT} vs. LINAC Dose (Measured using Silicon Calorimeters) for One Size of 48-nm Gate Oxide P- and N-channel Transistors at 4.6E10 rad(Si)/s

3.5.4.9 Implications

The large differences at the highest dose rate observed for p-channel transistors could be due to a number of factors. These include variations in beam uniformity at the highest dose rate, which is the closest position to the beam head; variations in inductance due to differences in length of bond wires, metallization path lengths on the die, etc. and due to variations in internal photocurrents in wells, etc. causing variations in bias conditions during pulse; or unknown factor(s). These differences could cause variability in all high dose rate tests at the Hill Air Force Base LINAC (and possibly at other LINACs). For future testing it is important to understand the mechanisms for the large differences.

3.5.5 Comparison of Total Ionizing Dose Inferred From X-Ray and LINAC Voltage Shifts

LINAC measurements were all taken immediately after irradiation (i.e., no intentional anneal). For the x-ray exposures at a dose rate of 1667 rad(SiO_2)/s, it takes 10 minutes of beam time to irradiate to a total dose of 1 Mrad(SiO_2). A considerable amount of annealing of ΔV_{ot} can take place in this time period. However, to match LINAC ΔVot measurements to x-ray measurements, it is possible to anneal under bias the transistors irradiated using the LINAC for the time it took to irradiate the transistors using x-rays.

3.5.5.1 Neutralization of Oxide-trap Charge can occur over Many Decades in Time

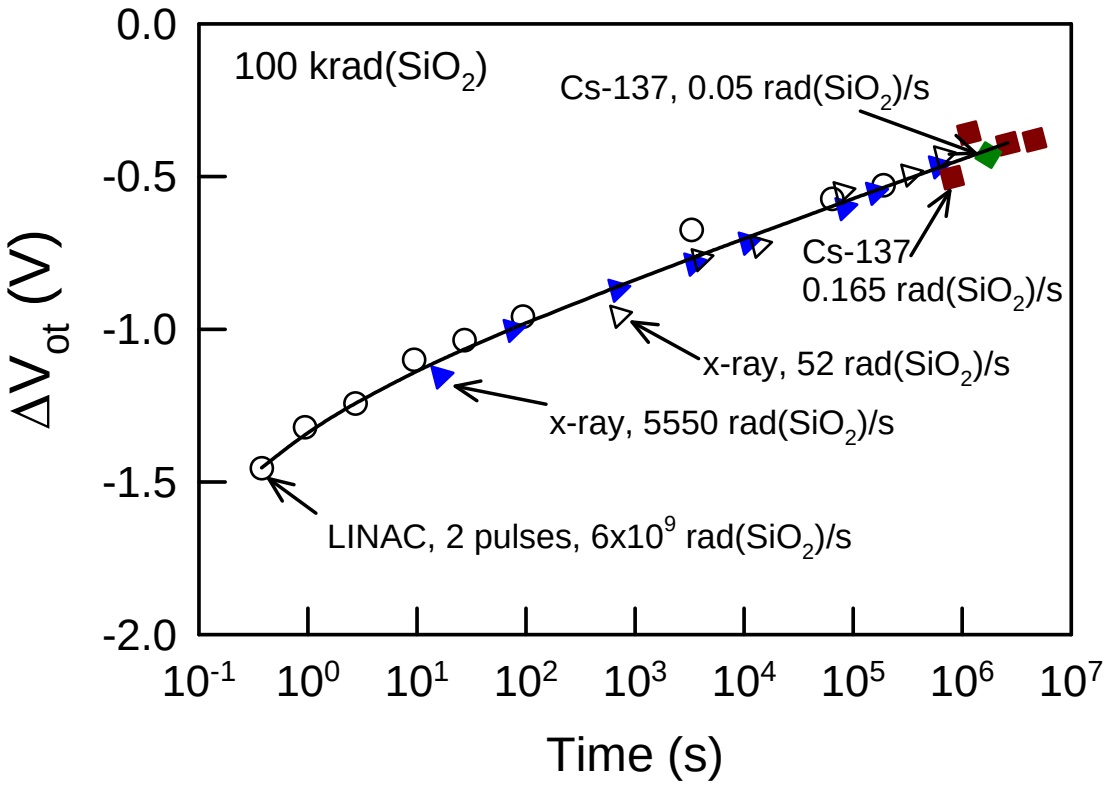

After D. M. Fleetwood, et al., IEEE Trans. Nucl. Sci. NS-35, 1497 (1988)

Figure 39: ΔV_{OT} Changes with Annealing Over Time

The annealing process is illustrated in the Figure 39. The data for this figure were taken on 4/3 µm transistors (from a different lot than for the transistors of the previous figures) irradiated to 100 krad(SiO_2) with a 6 V gate bias using several different radiation sources. After each irradiation, the transistors were annealed with a 6 V bias and re-measured at periodic intervals. As long as the transistors are annealed, regardless of the dose rate of radiation source, the same values for ΔV_{ot} are measured. Neutralization follows a transient annealing curve which is independent of dose rate. Therefore, LINAC voltage shifts can be quantitatively compared to x-ray voltage shifts if the annealing time is adjusted to be the same.

For Figures 40-47, transistors were irradiated using x rays or using the LINAC. To compare the LINAC data to the x-ray data, the transistors irradiated using the LINAC were annealed to approximately the same time as it took to irradiate transistors using the x ray source. For example, it took about 2 minutes to irradiate transistors to 200 krad(SiO2) in the x-ray source. To compare this data to LINAC data, transistors were irradiated to 200 krad(SiO2) at the LINAC and then annealed for 2 minutes under bias and then measured. (Measurements were also taken immediately after and after a 10 minute anneal on the transistors irradiated at the LINAC.) In this manner, it is possible to compare ΔV_{ot} for the LINAC irradiations to ΔV_{ot} for the x-ray irradiations. Any differences in ΔV_{ot} for the transistors irradiated using the two radiation sources should be due either to differences in dosimetry or due to space charge effects at the high dose rates. However, based on previous results, we do not expect there to be significant space charge effects at these dose rates and total ionizing dose levels.

3.5.5.2 ΔV_{ot} Different for LINAC and X-Ray Irradiations for 48-nm N-Channel Transistors

Figure 40 is a plot of ΔV_{ot} versus total ionizing dose for G1928A W44 n-channel transistors irradiated with 10-keV x rays and with the LINAC. LINAC data are shown for transistors characterized immediately after irradiation and after annealing for a time equivalent to the time it took to irradiate to the same total ionizing dose using x-rays (note that this required the LINAC data to be annealed for different times). The LINAC irradiations were all performed with 49 µs pulses at varying dose rate. Both the x-ray and LINAC irradiations were performed with an oxide electric field of 2 MV/cm. The annealed LINAC data do not agree with the x-ray data for all total ionizing dose levels. For example, there is a 28% difference in ΔV_{ot} at 1 Mrad(Si). A first look suggests that the LINAC dose to obtain the same voltage shift is approximately ~60% larger than the x-ray dose. Based on previous data as presented above, this is unexpected, and the cause of the differences is unknown.

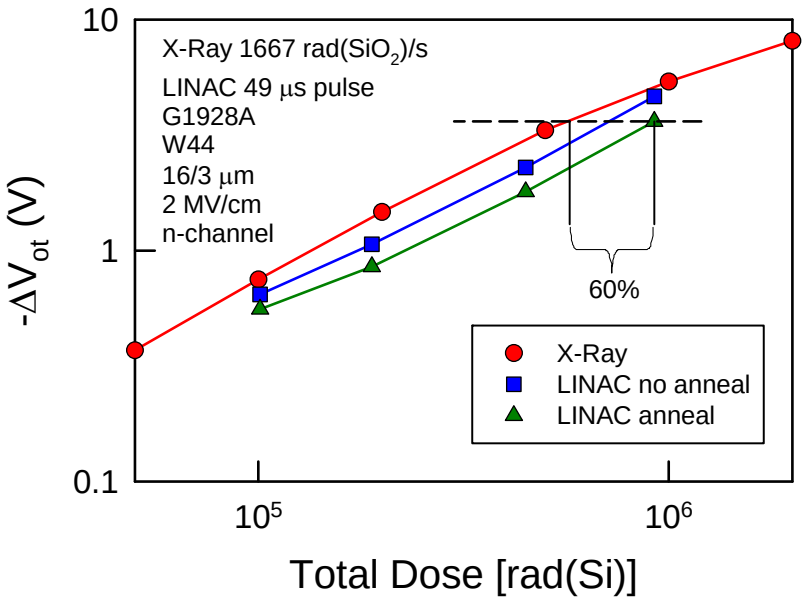

Figure 40: ΔV_{OT} vs. Total Dose for a 48-nm Gate 16x3 µm Oxide µm N-channel Transistors for X-Ray, LINAC without Annealing, and LINAC with Annealing

3.5.5.3 ΔV_{ot} Different for LINAC and X-Ray Irradiations for P-Channel Transistors

Figure 41 is a plot of ΔV_{ot} versus total ionizing dose for 48-nm gate oxide G1928A W44 p-channel transistors irradiated with 10-keV x-rays and with the LINAC. LINAC data are shown for transistors characterized after an anneal for a time equivalent to the time it took to irradiate to the same total ionizing dose using x-rays (note that this required the LINAC data to be annealed for different times). The LINAC irradiations were all performed with 49 μs pulses at varying dose rate. Both the x-ray and LINAC irradiations were performed with an oxide electric field of 2 MV/cm. The annealed LINAC data do not agree with the x-ray data for all total ionizing dose levels. For example, there is a 33% difference in the voltage shift at 1 Mrad(Si). Once again, the LINAC dose to obtain the same voltage shift is approximately ~60% larger than the x-ray dose. Based on previous data as presented above, this is unexpected.

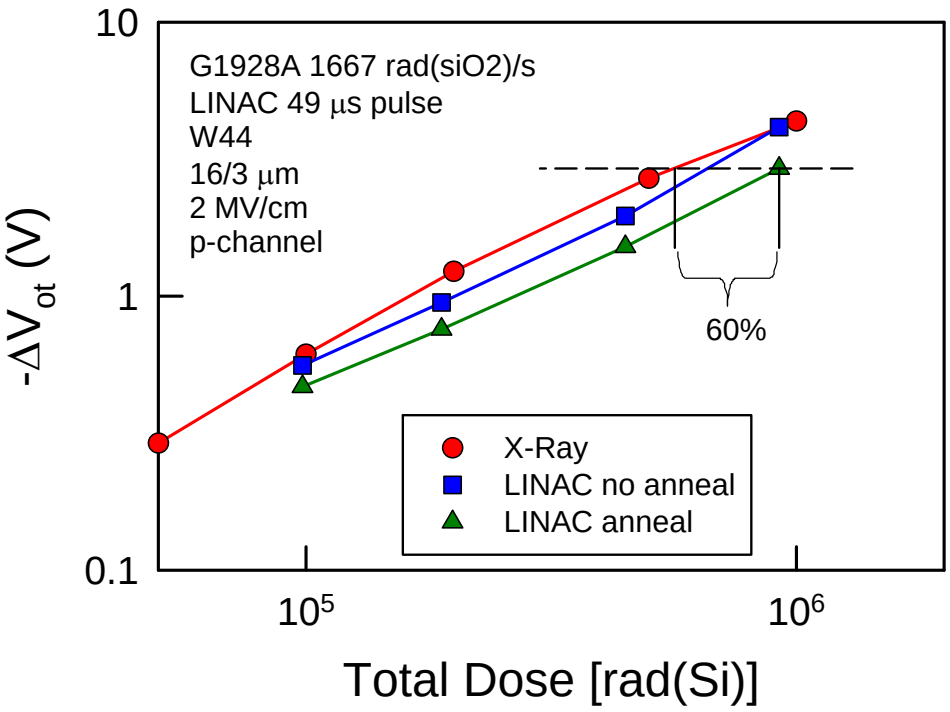

Figure 41: ΔV_{OT} vs. Total Dose a of 48-nm Gate 16x3 μm Oxide P-channel Transistors for X-Ray, LINAC without Annealing, and LINAC with Annealing

3.5.5.4 LINAC ΔV_{ot} is approximately the same for the different sizes of 48-nm p- and n-channel transistors

Figure 42 shows that the LINAC-induced ΔV_{OT} is not dependent on transistor size for either the n-channel or p-channel for the 48-nm gate oxide G1928A W44 in the dose range of 10^5 to 10^6 rad(Si).

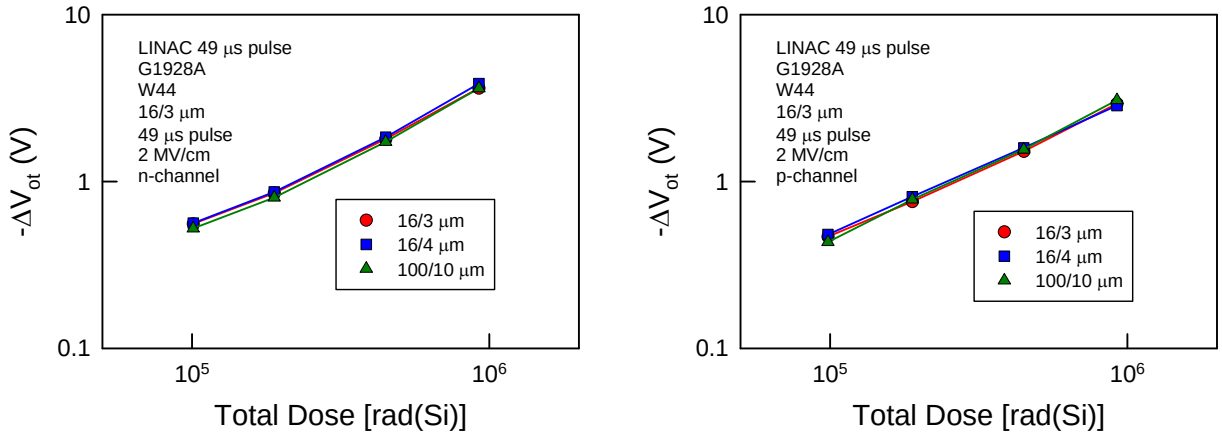

Figure 42: Effect of Transistor Size on ΔV_{OT} vs. LINAC Dose for N- and P-channel 48-nm Gate Oxide Transistors

The tests shown in Figure 43 were performed using n-channel 65-nm gate oxide transistors, while Figure 44 shows results for p-channel 65-nm gate oxide transistors. LINAC anneal measurements taken at equivalent time taken to obtain the same x-ray dose. The data shows the same general trends as for the 48-nm gate oxide transistors: silicon calorimeters indicate a lower total dose than the MOSFET measurements.

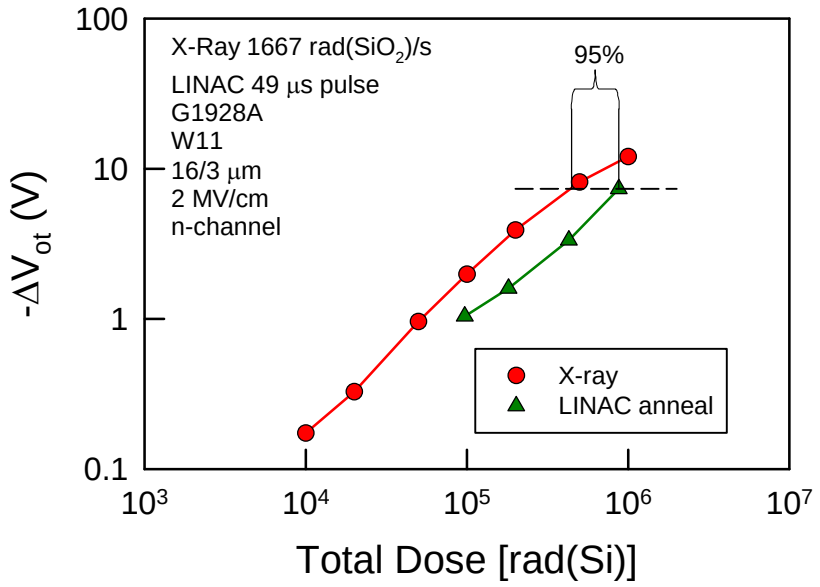

Figure 43: ΔV_{OT} for X-Ray and LINAC (with Anneal) for 65-nm Gate Oxide N-channel Transistors

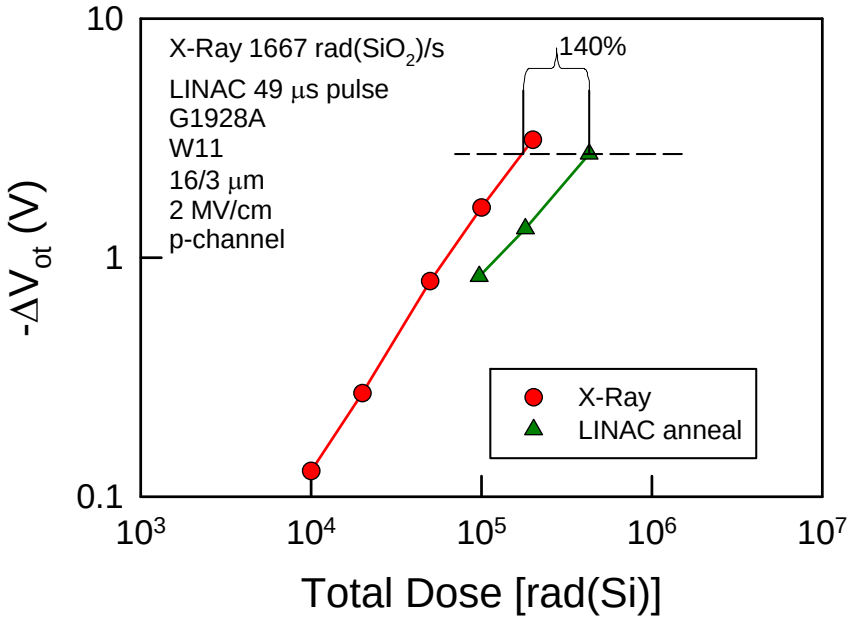

Figure 44: ΔV_{OT} for X-Ray and LINAC (with Anneal) for 65-nm Gate Oxide P-channel Transistors

Figures 45 and 46 show that the LINAC-induced ΔV_{OT} is not dependent on transistor size for either the n-channel or p-channel for the 65-nm gate oxide G1928A W11 in the dose range of 10^5 to 10^6 rad(Si).

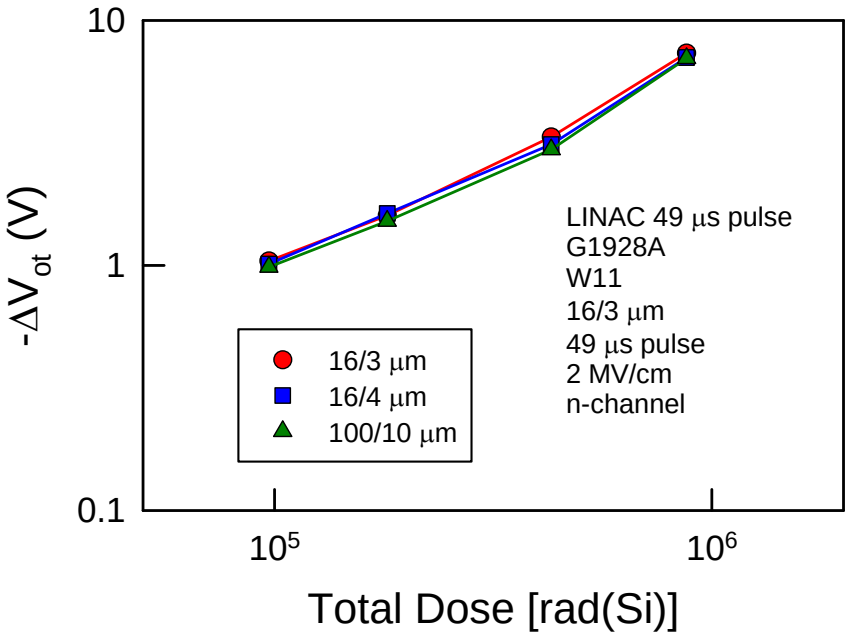

Figure 45: Insensitivity of N-channel 65-nm gate Oxide ΔV_{ot} to Transistor Size for LINAC Exposures

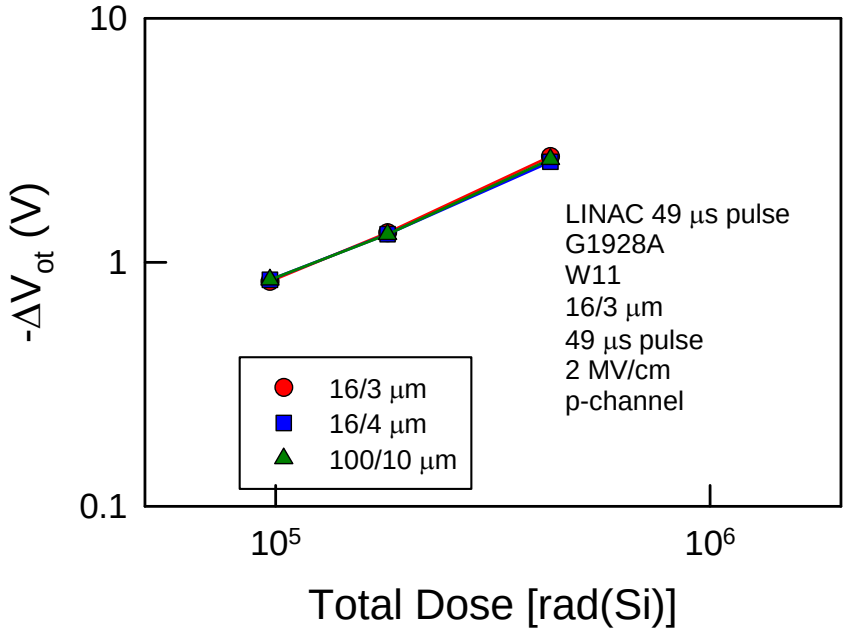

Figure 46: Insensitivity of P-channel 65-nm Gate Oxide ΔV_{ot} to Transistor Size for LINAC Exposures

3.5.5.5 The Discrepancy with Dosimetry Measurements varies with Total Dose

The discrepancy between the dose required to produce a given ΔV_{ot} using x-rays and the dose required to produce the same ΔV_{ot} using the LINAC can be estimated as shown in Figures 40 and 41. In Figure 47, this dose discrepancy is plotted as a function of the x-ray dose for the 65-nm gate oxide n-channel devices. At low total doses the difference between the silicon calorimeter and MOSFET measurements becomes less. Old LINAC results comparing x-ray and MOSFET measurements were mostly for total doses/pulse of 50 krad(Si) or less. At high total doses (dose rates) the difference does not continue to get worse. This suggests that MOSFET space charge effects are not the primary cause of the discrepancies.

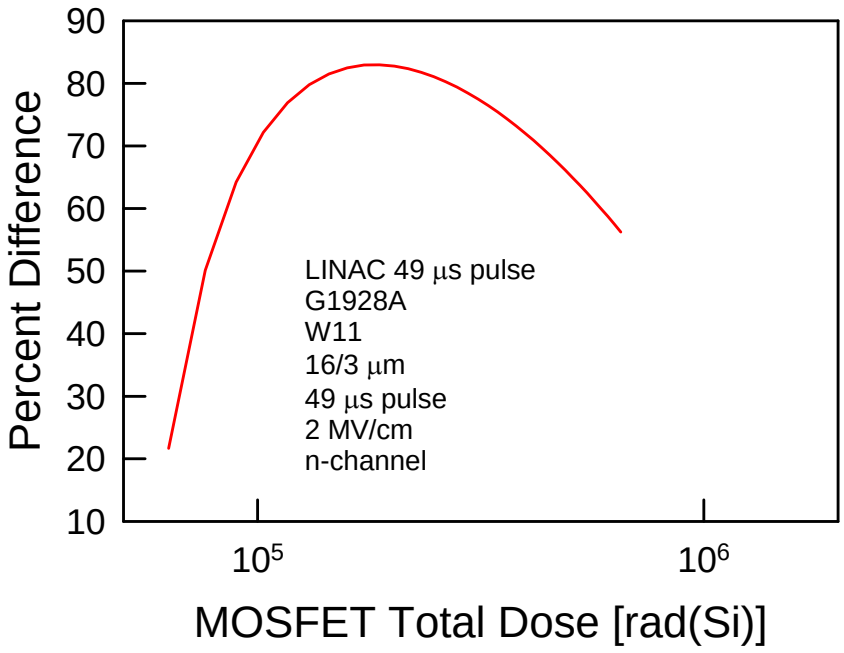

Figure 47: Percent Difference between Calorimeter and ΔV_{ot}-derived Dose for 65-nm Gate Oxide N-channel Transistors

The mechanism leading to discrepancies in voltage shifts with transistor size at high dose rate is unlikely to be the same mechanism causing the discrepancies in total ionizing dose between oxide and calorimeter.

3.5.6 Oxide Measurements Summary

Large differences in voltage shifts were observed at high dose rate for different sizes of p-channel transistors as discussed in section 3.5.4.7. Larger differences were also observed between n- and p-channel transistors at high dose rate as discussed in section 3.5.4.8. Mechanisms for differences at high dose rate are unknown. Large differences in total ionizing dose are still observed between silicon calorimeter and MOSFET measurements as discussed in section 3.5.5. Total ionizing dose for MOSFETs is inferred from voltage shifts calibrated using a 10-keV x-ray source. These data indicate lower total dose readings for the silicon calorimeter than for the MOSFETs. Differences up to 140% were observed (see Figure 44). Mechanisms for the differences at high total dose are unknown.

Although they are not plotted, multiple pulse exposures to achieve the same total dose as the single pulse exposures were also taken on the LINAC, and these experiments showed the same behavior with total dose as the single pulse exposures. This result indicates that the dose-dependent anomaly in oxide response really is dose-dependent, and is not affected by whether the dose is deposited in a single pulse or multiple pulses.

3.6 Diamond Photoconducting Detector (PCD) Dosimetry Results

Neutron-damaged diamond PCDs have a subnanosecond carrier lifetime and a relatively low conductivity response to ionizing radiation which makes them particularly useful for pulse shape characterization of high dose rate ionizing radiation sources. Diamond PCDs are routinely used at MEDUSA for pulse shape measurement and as a transfer calibration from silicon calorimeters to device experiments. For this application, the absolute calibration is not crucial, but accuracy in following the pulse shape is important. A series of experiments using single-ended PCDs have been performed to evaluate this accuracy.

3.6.1 Pulse Shape Behavior of Diamond PCDs

Inspection of waveforms suggests that the PCD signal differs substantially in shape from the accelerator current waveform, which is approximately the radiation waveform since MEDUSA operates with an almost constant electron energy spectrum. The first plot, Figure 48, shows the normalized PCD pulse shapes for fixed pulse width at three dose rates (units of rad(Si)/s). The first parts of the pulse look very similar, but the later parts of the pulse show more droop at the higher dose rate.

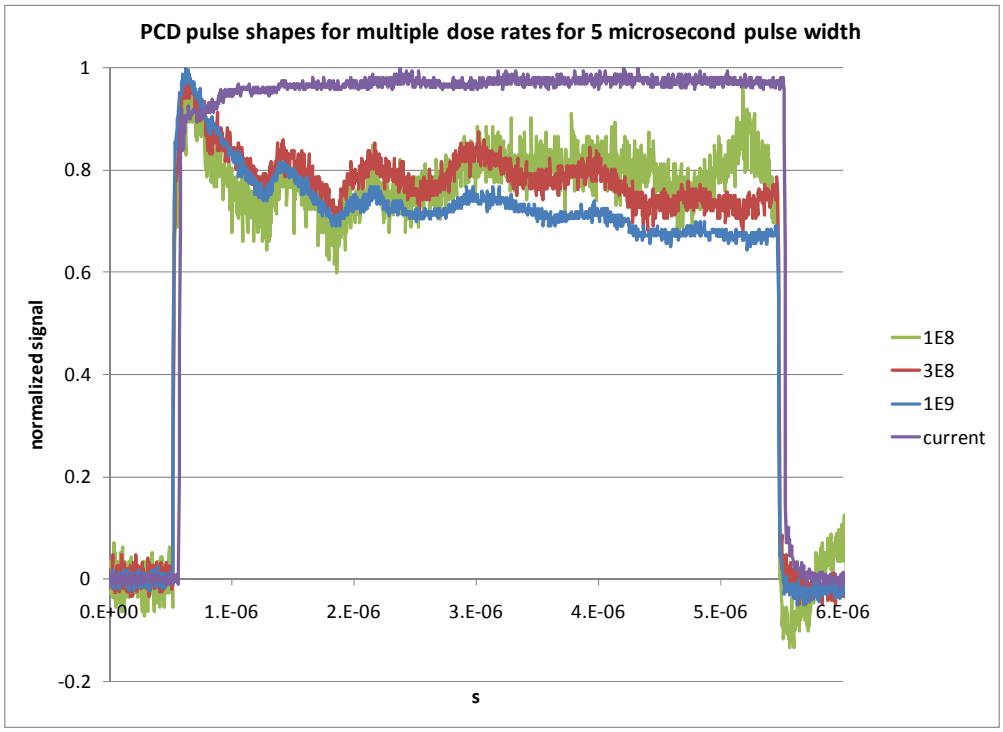

Figure 48: PCD Pulse Shapes for Different Dose Rates for 5 Microsecond Pulse Width

The next plot, Figure 49, shows the pulse shape for varying pulse width at a fixed dose rate of 1E9 rad(Si)/s. The droop reaches a minimum about 10 microseconds, and then climbs slightly later in the pulse.

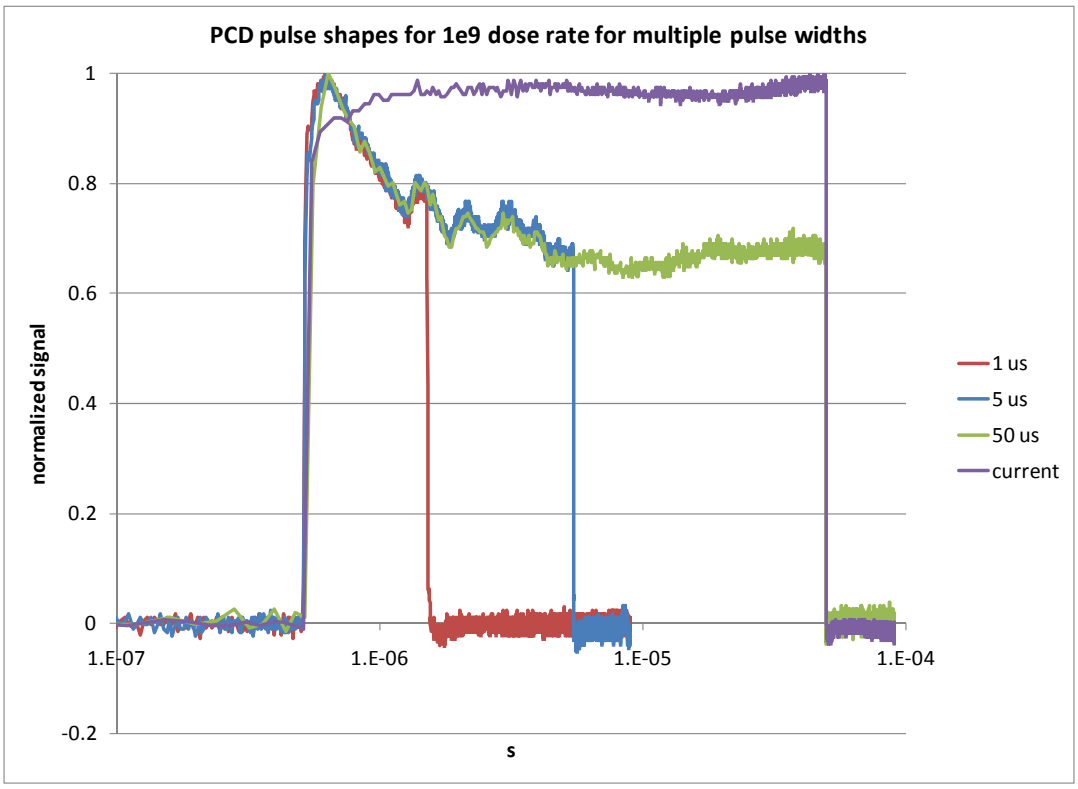

Figure 49: PCD Pulse Shapes for a 1e9 rad(Si)/s Dose Rate for Multiple Pulse Widths

3.6.1.1 Evaluation of the Possibility of Debiasing of the PCDs during the Pulse

One possible explanation of the reduced response of the PCDs later in the pulse is that the power supply of the PCDs is unable to maintain the bias during the radiation pulse. If this were true, then the shape of droop should change significantly with dose rate, dropping faster at higher dose rates. However, inspection of the figures shows that the shape of the early part of the PCD pulse is almost independent of dose rate. In addition, direct measurement of the PCD bias during the pulse using a four-wire measurement to sense the bias voltage at the PCD shows essentially no droop in the PCD bias during the pulse.

3.6.1.2 Effect of PCD Position on Pulse Shape

Interpretation of the PCD pulse shape at MEDUSA is complicated somewhat because the PCDs are fielded on either side of the device under test, so the pulse shape may be affected by a sweeping of the beam early in the pulse. However, on one set of shots, one PCD was centered and the other was in the "normal" off-axis position. As the following plot in Figure 50 shows, the pulse shapes are very similar. At the very beginning of the pulse there is some indication that the on-axis signal lags the off-axis signal slightly, but they are identical by 1 microsecond. Later in time, after about 20 microseconds, the on-axis signal is slightly higher than the off-axis signal. This may reflect the weak focusing discussed earlier in the context of the calorimeter signal. However, the major features of the PCD pulse shape discussed in this section are identical for the on-axis and off-axis signals.

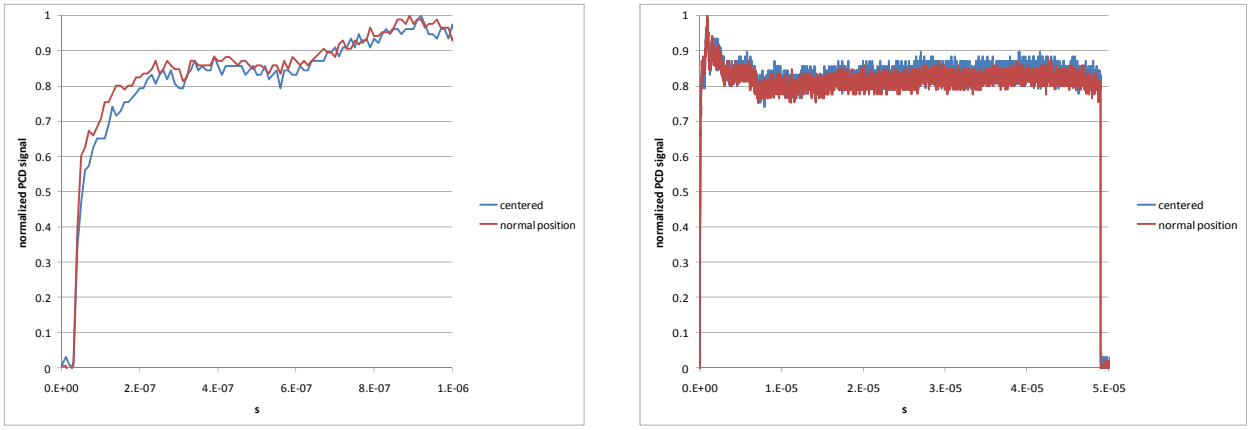

Figure 50: Comparison of Centered and Off-Axis Normal Position PCD Signals Early in Pulse and Over Full Pulse

3.6.1.3 Comparison with other Pulse Shape Monitors

As discussed above, the photocurrent output of a neutron-damaged 2n2222 transistor appears to closely track the time dependence of the silicon dose rate at a given position. The pulse shapes produced by a neutron-damaged 2n2222 transistor, as discussed previously, and a single-ended PCD at a dose rate position of approximately 1.2E9 rad(Si)/s are compared (after normalization) in Figure 51. The transistor is located in the center of the beam, and the PCD is located off to the side. However, as noted above, the PCD pulse shape depends only slightly on position.

Neither of these signals shows the nice flat top the current waveform would suggest. Even with neutron damage, the 2N222 still shows some rise time likely due to residual diffusion current contribution to the photocurrent. The PCD shows the early spike discussed earlier.

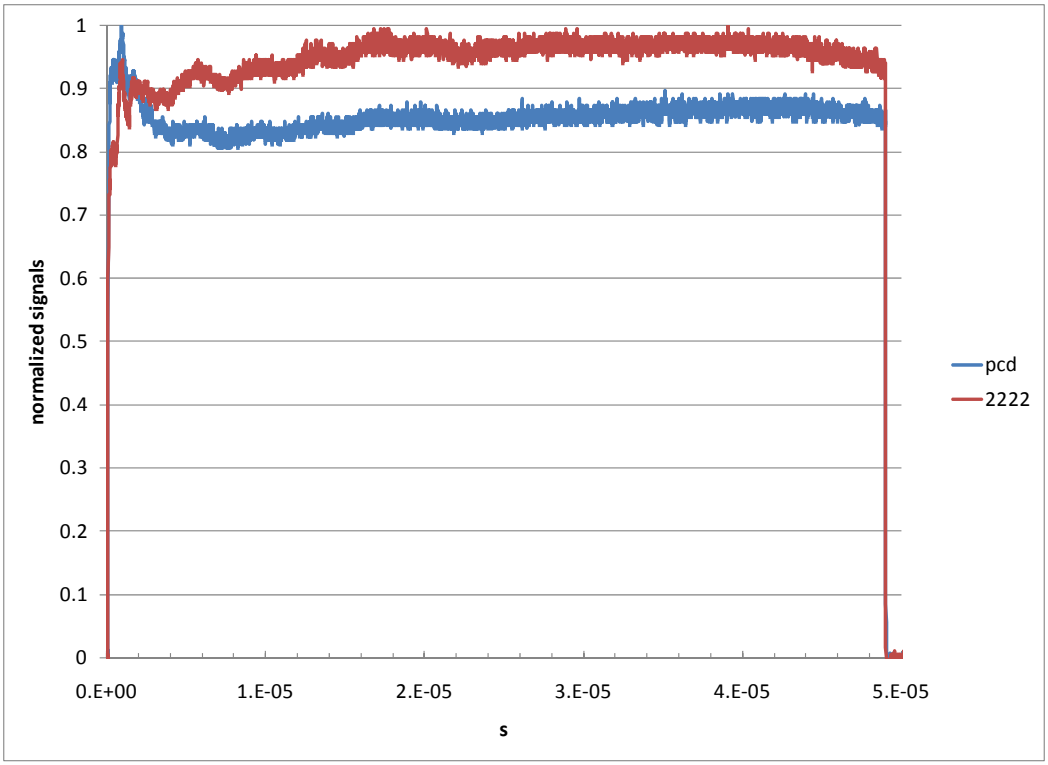

Figure 51: Comparison between PCD and Neutron-damaged 2N2222 Photocurrent

3.6.2 Discussion of PCD Results

The PCD pulse shape clearly differs from the accelerator current signal and the silicon dose rate as measured by the photocurrent in the neutron-damaged transistors. The reason for the difference is not clear.

3.7 Lithium Fluoride Dosimetry

Lithium fluoride (LiF) TLDs are commonly used in radiobiological applications because the low atomic number of the constituents means that the dose response can be related to tissue dose response in a straightforward fashion. This ready availability makes them a convenient and inexpensive choice for dosimetry, and they are commonly used at MEDUSA. The details of the thermoluminescent response of

LiF are quite complicated, with multiple luminescence peaks contributing to the glow curve, so they will not be addressed here. However, it is useful to know the relationship of LiF to CaF_2:Mn response, so a brief set of exposures comparing the response was taken with the LiF and the CaF_2:Mn in the same environment. The results are shown in Figure 52. The lithium fluoride dose tracks the calcium fluoride dose up to about 30 krad, at which point the lithium fluoride begins to underread compared to the calcium fluoride, with the difference increasing to about 15% at 60 krad. This result is not unexpected, since lithium fluoride is known to have dose/dose rate issues.

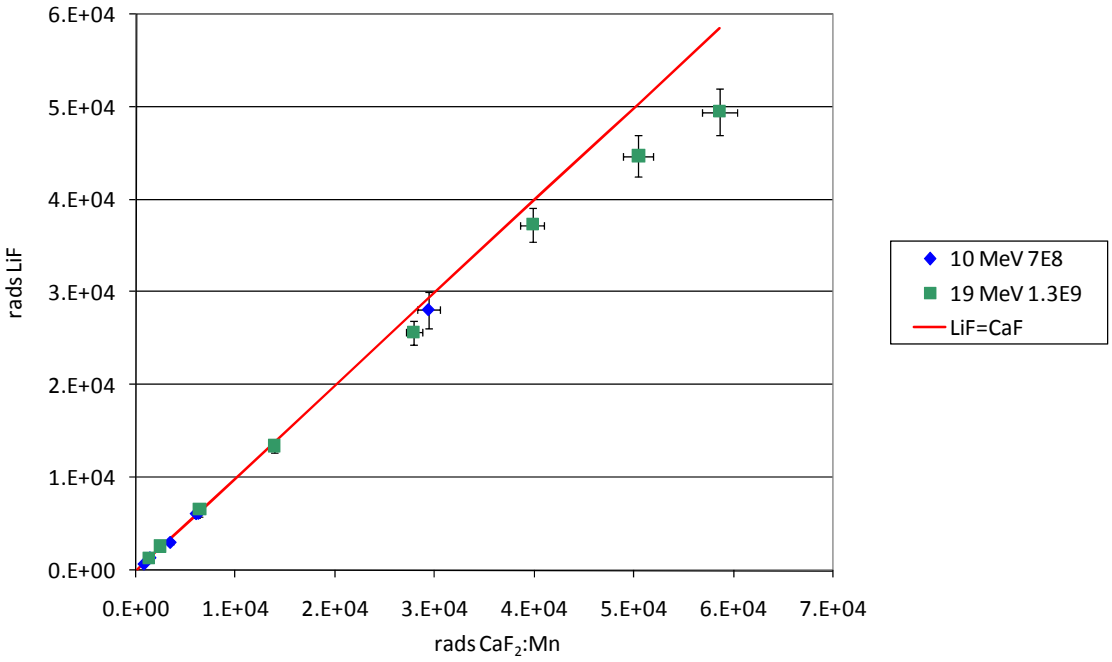

Figure 52: Rad (LiF) versus Rad(CaF2:Mn) Measured at Multiple Beam Energies and Dose Rates

3.8 Alanine Dosimetry

Alanine dosimetry has become the reference dosimetry for standards laboratories. When alanine is exposed to an ionizing radiation field, large numbers of unpaired electrons are formed. Most of these recombine immediately, but the crystal structure of alanine inhibits diffusion, and the remaining unpaired electrons remain in place. The dosimeter is read using electron paramagnetic resonance. Alanine dosimeters have the unusual property that they can be read out multiple times without destroying the dosimetry signal.

On a few shots alanine dosimeters were exposed with SVIC CaF_2:Mn dosimeters in calorimeter housings. These exposures used a .125 inch thick aluminum scatter plate at the beam head. Exposures were performed with 10 MeV and 19 MeV electrons. The results are shown in Figure 53.

The dose ratios calorimeter/alanine show no particular trend with dose. The absolute values of the dose differ, likely because the alanine is not correctly equilibrated in this environment. The approximate independence of the dose ratio from the dose is consistent with this interpretation. This dose ratio also does not seem to depend on whether the 10 MeV or the 19 MeV tuning of MEDUSA is used.

The dose ratios SNLTLD/alanine decrease with dose, similar to the behavior observed in the ratio TLD/calorimeter discussed above. This decrease supports the idea that the TLDs are underreading at high doses.

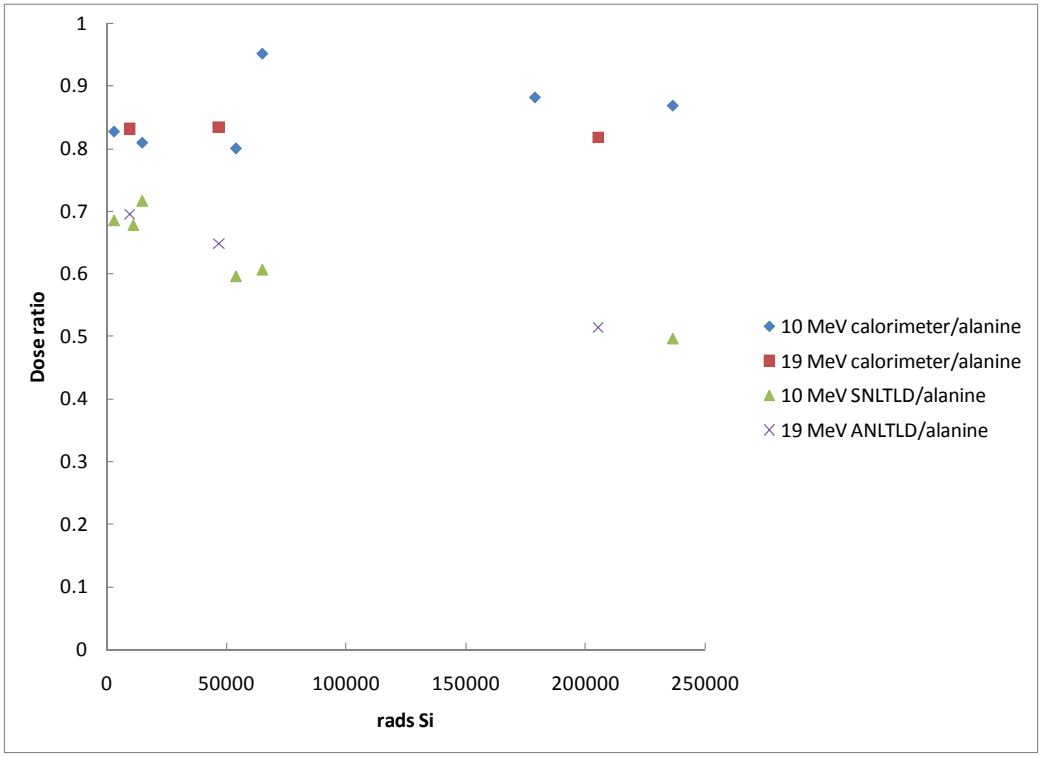

Figure 53: Dose Ratios for Calorimeter and TLD Compared to Alanine

4 Appendix

4.1 Silicon Physics Mechanisms

A brief review of coupling of the electron beam energy to the silicon may be helpful in considering whether the 19 MeV electron beam at MEDUSA may be expected to behave differently than other ionizing radiation sources.

Electrons at this energy have a non-ionizing energy loss in silicon of about 3e-4 MeV/cm[4]. This compares with the ionizing energy loss of about 4.1 MeV/cm, so represents about 10^{-4} of the deposited energy. Now at 1 Mrad(Si), the fluence of 20 MeV electrons is 3.5e13 e/cm^2. So the NIEL is 1.05e10 MeV/cm^3, or 4.2e14 silicon displacements/cm^3, or 130 rads^{NIEL}(Si). The amount of energy in the displacement is negligible for purposes of the calorimetry. It is however possible that the defects may be of interest. Most of the displacements will be in the form of isolated defects or small cascades, so recombination of those defects will not be as rapid as in the case of clustered defects created by heavier particles.

The electrons passing through the silicon interact with electrons, injecting them into the conduction band and creating electron-hole pairs. The mean energy to create an electron-hole pair is about 3.4 eV in silicon. These electron-hole pairs then recombine by various mechanisms. Since silicon is an indirect band gap material, the electrons and holes cannot recombine directly – a third body is required to conserve energy and momentum. If they recombine at a defect, this is Shockley-Read-Hall recombination. This takes place through a two-step process. First, an electron or hole is trapped by an energy state in the forbidden region associated with a defect. If a hole or electron moves up to the same energy state before the initial electron or hole is thermally reemitted to the conduction band, then the electron-hole pair recombines, with the excess energy taken up by phonons. The SRH recombination lifetime is highly dependent on the density of states near the mid-gap. If the electron-hole pair recombines with an electron in the conduction band as the third body taking up the excess energy, this is Auger recombination. If the SRH and Auger recombination rates are sufficiently small, as in nearly-intrinsic material or at very low temperatures, then radiative recombination, with a phonon acting as the third body, can play a significant role. In SRH recombination, the lattice is heated directly. In Auger recombination, the conduction electrons are heated. However, since the electron-lattice thermal equilibration time is less than 1 picosecond[5] there is no difference in the resulting lattice temperatures. With radiative recombination there is a potential for the energy to leave the lattice, reducing the deposited energy. Since the typical absorption for band-edge photons in silicon is 3-5 cm^{-1}, the likelihood of these photons leaving the calorimeter chip is reasonably high[6]. At dose rates of 10^9 rads(Si)/s, Auger recombination is by far the dominant process for electron-hole pairs created by electron energy deposition in silicon. This summary of the physical processes involved in energy

[4] Claude Leroy and Pier-Giorgio Rancoita, Rep. Prog. Phys. **70**, 493 (2007).
[5] F. E. Doany, D. Grischkowsky, Appl. Phys. Lett. **52**, 36 (1988).
[6] H. Schlangenotto, H. Maeder, W. Gerlach, Phys. Stat. Sol. (A) **21**, 357 (1974).

deposition in silicon by ionizing radiation provides no basis for supposing that silicon energy deposition by 19 MeV electrons should differ from deposition by lower energy electrons or by photons.

4.2 CaF_2:Mn TLD Physics Mechanisms

In recent years, a substantial body of work[7] has been performed to elucidate the physical mechanisms associated with the thermoluminescence in CaF_2:Mn. TLDs in normal use have about 3% Mn, which is close to the solid solution limit. These produce a strong dose-dependent luminescence at 495 nm when heated through the temperature range 200-400 C. This luminescence is due to a transition from the $^4T_{1g}$ (^4G) level, which is the first excited state, to the $^6A_{1g}$ (^6S) ground state of Mn^{2+}. The Mn^{2+} atoms substitute for Ca in the lattice. The ground state of the $3d^5$ electrons in Mn^{2+} is a spin sextet with all six spins aligned. The excited state transitions are each associated with a spin reversal and so are highly forbidden.

The sequence of processes in the TLDs has been identified as follows. Ionization produces electron-hole pairs in the lattice. Electrons and self-trapped holes undergo non-radiative recombination via an excitonic mechanism resulting in the formation of F- and H- type and I-type defects. In CaF_2, vacancy center production is a highly inefficient process because the orientation of the self-trapped exciton in a fluorite structure is not amenable to the production of a close-packed collision sequence. This makes pure CaF_2 quite resistant to color center formation. However, the presence of impurities can stabilize the formation process by the trapping of excitons such that the vacancy production may actually take place next to the Mn^{2+} sites.

The source of at least a major part of the thermoluminescence is direct excitation of the Mn^{2+} by luminescence from thermally-activated recombination of electrons and self-trapped holes.[8] The excitation and deexcitation of the Mn^{2+} are mediated by an adjacent F-center.[9]

CaF_2:Mn TLDs have attractive features including high sensitivity, linear dose response over a large range, independence from dose rate over a large range, and an acceptable fading rate. Any explanation of anomalies in the measured TLD dose must be consistent with these characteristics.

Displacement damage may be a factor in understanding the TLD response. Although the primary energy deposition mechanism for 20 MeV electrons is ionization, which leads to thermoluminescence as described above, these energetic electrons can also produce displacement damage in the lattice.[10] The displacement can be in the form of both isolated defects and clustered defects. For 1 MeV electrons, the maximum energy transfer to lattice atoms is a few tens of eV, so only isolated defects are formed (the threshold energy transfer to displace an atom is typically 20 eV). As the electron energy is increased for relativistic electrons, the maximum energy transfer to a lattice atom increases almost as the square of the electron energy, so for 20 MeV electrons displacing Ca atoms the maximum recoil energy is over 20 keV. This can result in the formation of defect clusters.

---

[7] S. W. S. McKeever, B. Jassemnejad, J. F. Landreth, J. Appl. Phys. **60** (3), 1124.
[8] B. Jassemnejad, R. J. Abbundi, M. D. Brown, S. W. S. McKeever, Phys. Stat. Sol. (A) **108**, 753 (1988).
[9] A. C. Lewandowski, T. M. Wilson, Phys. Rev. B, **52** (1), 100 (1995).
[10] O. S. Oen, in *Radiation Effects in Semiconductors*, edited by F. L. Vook (Plenum, New York, 1968), p. 264.

The saturation level for CaF_2:Mn for Co^{60} radiation is typically taken as about 500 krads, although the response begins to be sublinear at levels as low as 100 krads. This saturation is produced by a darkening of the TLD which results in self-absorption of the thermoluminescence. This darkening is not produced by the defect centers which produce the dosimetric thermoluminescence, since it is not annealed by reading the TLDs. It is however removed by the longer anneal which is used for preconditioning the TLDs, and so is produced by more stable defect complexes which are produced at a lower rate than the thermoluminescent defects.

The response of CaF_2:Mn is known to be reduced for high LET particles,[11] as shown in the following summary.

Int. J. Appl. Radiat. Isot. Vol. 33, pp. 1085 to 1100, 1982
Printed in Great Britain

020-708X/82/111085-16$03.00/0
Pergamon Press Ltd

Heavy Charged Particle Thermoluminescence Dosimetry: Track Structure Theory and Experiments*

J. KALEF-EZRA† and Y. S. HOROWITZ

Department of Physics, Ben Gurion University of the Negev, Beersheva, Israel

[11] J. Kalef-Ezra and Y. S .Horowitz, Int. J. Appl. Radiat. Isot. **33**, 1085, 1982.

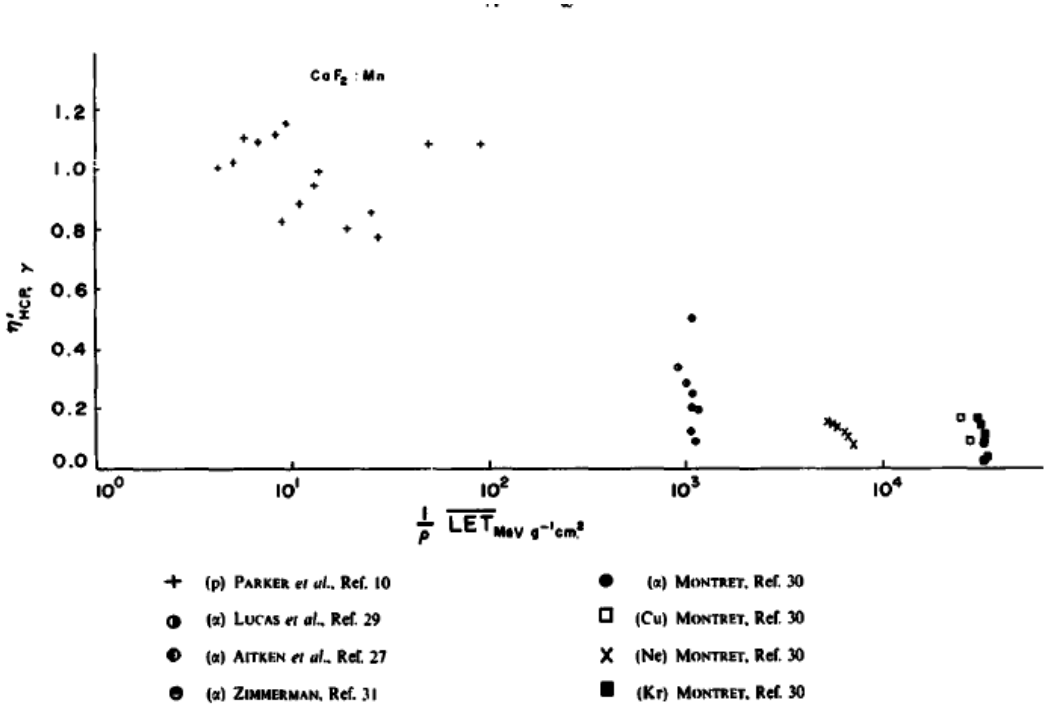

FIG. 4. Relative TL response (main peak height) of CaF_2:Mn to heacy charged particles as a function of $1/\rho\ \overline{LET}_\infty$.

One possible explanation for the reduced response for high LET particles is that the local ionization dose deposited along the path of the particle exceeds the saturation level, resulting in self-absorption of the thermoluminescence.

It is plausible to consider that a cause of the reduced response of CaF_2:Mn TLDs to high energy electron ionization is the development of local darkening along the path of energetic ions displaced by the electrons. This darkening then interferes with the escape of thermoluminescence from the body of the TLD, reducing the indicated dose. If for example the darkening is due to the formation of calcium colloids due to aggregation of anion vacancies, the absorption is in a broad band centered at 550 nm[12], which would partially obscure the thermoluminescence peak at 495 nm.

4.2.1 Radiation Effects on the CaF_2 Lattice

The following is quoted from a dissertation from the Free University of Berlin with the following link:

http://www.diss.fu-berlin.de/diss/servlets/MCRFileNodeServlet/FUDISS_derivate_000000000200/02_ch_2.pdf

2.1. Structure of the CaF_2 crystal

CaF_2 is an ionic crystal with the fluorite structure. The lattice is a face centered cubic (fcc) structure with three sublattices. The unit cell of the material is most easily described as a simple cubic lattice formed

[12] M. L. Sanjuán, P. B. Oliete, V. M. Orera, J. Phys.: Condens. Matter **6**, 9647 (1994).

by the F^- ions where a Ca_2^+ ion is contained in every second cube. The remaining empty cubes (called interstitial or hollow sites) are important for defect formation and diffusion, but also for the accommodation of unwanted impurities like rare earth ions and dopants. The lattice constant is a=5.451 Å (Fig. 2.1). The natural cleavage plane of the crystal is the (111) surface. It is build up from F^--Ca_2^+-F^- triple layers of 3.14 Å distance and is terminated by fluorine ions. The melting point of CaF_2 is at 1620 K. At a temperature of 1420 K, a maximum of the specific heat is observed that is caused by melting of the fluorine sublattice. The fluorine ions are randomly distributed over the normal lattice sites (tetrahedrally coordinated) and the interstitial sites (octahedrally coordinated). The ionic mobility consequently becomes very high. The behavior is known as superionic conduction, it is observed in a variety of materials with the fluorite structure. CaF_2 has a wide bandgap of about 12 eV, values in literature range from 11.6 eV to 12.1 eV . The first exciton peak is at 11.2 eV. The band structure was calculated by a number of authors. The valence band of CaF_2 consists of 2p levels of the fluorine ions, while the bottom of the conduction band originates from the 4s and 3d orbitals of the calcium ions.

2.2 Defects and surface defects in CaF_2

In this section, defects in CaF_2 that can be produced by electron or UV light irradiation are discussed. The defects are confined to the anion sublattice, while the cation sublattice remains unaffected. This can be understood from the large difference in formation energy of anion Frenkel pairs (2.6 - 2.7 eV) and cation Frenkel pairs (8.5 - 9.2 eV). Defects can be neutral or charged, the latter species are responsible for the increased electrical conductivity during irradiation and for field enhanced diffusion phenomena. A defect is considered neutral if the unit cell containing the defect remains neutral. In the electron and photon energy regime used in this work, defects are produced by electronic excitation only and not by displacement due to momentum transfer. The first basic step of defect creation is a bandgap excitation of an electron - hole (e-h) pair by ionizing radiation. As an estimate for the energy loss of the primary electrons per e-h excitation, Alig and Blohm gave a value of about three times the bandgap energy. Due to Coulomb attraction, the electron hole pairs form excitons. CaF_2 is a material with strong electron-phonon coupling, in which excitons localize by means of a lattice deformation to form self-trapped excitons (STE). This process occurs within picoseconds and has an efficiency of almost 1. One of the fluoride ions releases an electron and moves into one of the empty cubes. A covalent bond is established to one of the neighboring fluorides on a regular lattice site, thus an H-center is formed. The electron localizes on the vacant lattice site to form an F-center. The electronic state of the STE is a metastable $^3\Sigma_g$ state. Two optical absorption bands have been reported. At 3 eV, the F-center is excited, while the other band centered around 4.1 eV belongs to a hole excitation of the H-center. At this energy, the hole is excited from the top antibonding σ_u orbital of the F_2^- molecular ion to the binding σ_g orbital. Both excitations are slightly shifted compared those of the free defects. The lifetime of the metastable $^3\Sigma_g$ state of the STE is 1.7 µs at room temperature (RT). Three decay channels of the STE were observed. At low temperature, mainly a radiative decay takes place. The STE recombines into the ground state under emission of a broad luminescence band centered at 4.4 eV. The remaining elastic deformation is removed by the excitation of phonons. With increasing temperature, nonradiative recombination into the undisturbed lattice becomes important.

In the context of the present work, the third decay channel is the most interesting: separation of the STE into F and H-centers. Stable defects, that do not recombine as easily as the STE, are produced. Separation can be thermally activated, thus the efficiency of metal production is higher at elevated temperature. Also the excitation of the H-center at 4.1 eV results in a dissociation of the STE. The neutral fluorine can move to the next neighbor cube where again an H-center is formed by bonding to a fluoride ion on a regular lattice point. Also excitation with electrons, as was carried out in this work, was found to result in stable defects. Point defects in crystals with the fluorite structure have been reviewed by Hayes. The following brief description of the most prominent defects in CaF_2 given below has been extracted mainly from this work.

***F*-center** The *F*-center is a fluoride ion vacancy binding one electron. To avoid confusion with F denoting fluorine, the *F*-center is written as an italic letter throughout this work. The electronic structure of the *F*-center was investigated by Stoneham et al. It was shown that the ground state of the 1s wave function of the F-center is restricted to the anion vacancy. As the *F*-center is slightly larger than the fluorine ion, the cations move outwards by 4.2. The peak of the absorption band is at 3.3 eV with 0.3 FWHM and corresponds to an excitation from the 1s state to the 2p state. The 2p state, however, is already quite delocalized. Two neighboring *F*-centers form an M-center, three an R-center. A larger cluster of *F*-centers constitutes an area in the crystal that is free of fluorine. Metallic colloids can therefore be formed by F-center diffusion. In CaF_2, this process is favored because the lattice constant of the Ca fcc sublattice (5.451 Å) is very similar to the fcc lattice constant of Ca metal (5.58 Å). No reliable data are known for the *F*-center diffusion constant and energy. The annealing of F-centers in CaF_2 following neutron irradiation at 20 K has been investigated by Atobe. Three steps of *F*-center decay were observed: the first with an activation energy of 0.33 eV was attributed to the recombination of *F*-centers with thermally activated V_K-centers. The second step with an activation energy of 0.46 eV was assumed to be due to H-centers. The remaining *F*-centers decay with an activation energy of 0.72 eV. A mechanism for this last step was not proposed by Atobe, however, it follows that the *F*-center activation energy is 0.72 eV if the last step is due to *F*-center mobility, or larger if other defects become mobile and recombine with the remaining *F*-centers.

H-center A H-center in CaF_2 is an interstitial fluorine atom covalently bonded to a fluorine ion on a normal lattice site. The bond is along the <111> crystal. The peak of the optical absorption band is at 4 eV, a value for the activation energy for diffusion of 0.46 eV was given by Atobe.

I-center A negative fluoride ion residing in the center of an interstitial site is called an I-center. The defect may be produced by ionization of an H-center, as a charge compensating defect if the crystal is doped with three-valent rare earth ions, or by formation of an anion vacancy by thermal excitation (anion Frenkel pair). As the I-center consists of a filled shell ion, no covalent bonds to the neighboring ions on the regular lattice sites are formed. The I-center is not paramagnetic and no optical transitions have been reported. Only the perturbing influence on *F*-centers manifests its existence. Diffusion energies ranging from 0.53 to 1.63 eV have been reported. The I-center can be easier ionized than a regular fluoride ion as the Madelung potential in the center of the cube is negative. Since it is a charged defect, no I-center clusters are to be expected. By recombination with a V_K-center, the I-center is converted to an H-center.

Anion vacancy The anion vacancy is a positively charged defect. It is created together with an I-center by thermal excitation (anion Frenkel pair) or exists in CaF_2 as a charge compensating defect if the crystal is doped with monovalent alkali metal ions. Also electron stimulated desorption of fluorine produces vacancies at the surface. The measured activation energies for diffusion range from 0.52 to 0.87 eV. Due to its lower activation energy, the vacancy is more efficient in charge transport than the I-center. This situation is opposite to that encountered in most other solids, where the anion vacancy is less mobile than the corresponding interstitial.

V_K-center The self-trapped hole in CaF_2 consists of a F_2^- molecular ion with the bond axis oriented parallel to the <100> axis. It is formed during photoemission from valence band holes, or it may be produced together with an I-center from a H-center. The maximum of the absorption band is at 3.9 eV. Excitation energies for diffusion along the <100> axis ranging from 0.2 to 0.5 eV have been reported. The self-trapped hole plays an important role in increasing the electrical conductivity of CaF_2 during photon irradiation where also an activation energy of about 0.3 eV was determined.

4.3 MOS Device Energy Deposition Considerations

4.3.1 Radiation Transport Calculations

Typical construction of the 4/3 µm devices includes gate oxide thickness of 46 nm, a polysilicon thickness of 600 nm, and an aluminum metallization thickness of 1000 nm. Figure 54 shows that the dose profiles are not significantly different in the vicinity of the gate oxide, so no significant difference should be expected in the oxide response for equal doses to the oxide.

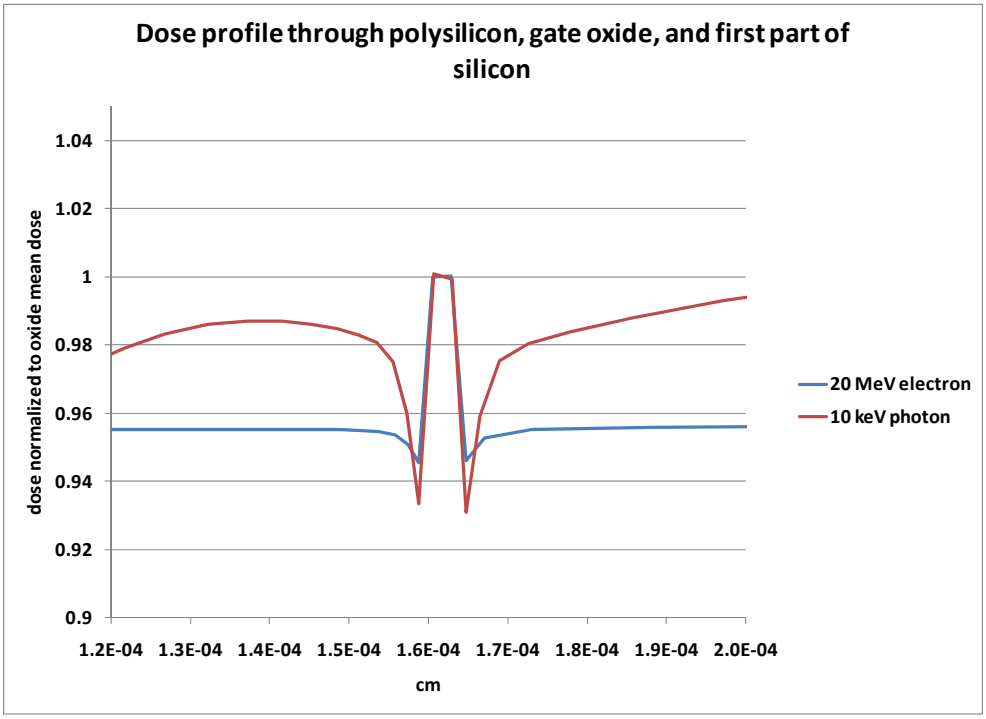

Figure 54: Dose Profile through Polysilicon, Gate Oxide and First Part of Silicon

4.3.2 Displacement Damage Effects on MOS Devices

Since MOS devices are majority carrier devices, displacement damage effects are generally considered to be unimportant. However, one can postulate a mechanism by which displacement damage could affect oxide trapped charge. The basic idea is that deep hole traps in the oxide are oxygen vacancies in the oxide lattice, and these oxygen vacancies can trap positive charge. The dominant source of these oxygen vacancies is believed to be incomplete oxidation at the Si-SiO_2 interface. Oxide trapped charge arises when holes produced by ionization encounter these traps as they migrate to the oxide boundary. One can consider that displacement damage in the oxide could increase the population of these traps, so that holes would be more likely to encounter a trap and hence the oxide trapped charge associated with an initial population of the electron-hole pairs would increase. The relevant question in this case is: what is the ratio of the number of displacement-damage induced oxygen vacancies to the initial oxygen vacancy population? The trapped charge density can be calculated using the expression $\Delta V_{OT} = -q\Delta N_{OT} / C_{OX}$ where ΔV_{OT} is the threshold voltage shift due to trapped charge in the oxide, ΔN_{OT} is the number oxide traps, and C_{OX} is the oxide capacitance. For a 1 V threshold shift, this gives a trapped charge density of ~1.2E11 cm^{-2} for the 48 nm oxide thickness. A Mott scattering calculation suggests that the number of atomic displacements in the oxide layer for 20 MeV electrons depositing 100 krads of ionization would be about 4E7 cm^{-3}, so this effect seems too small to impact the oxide threshold shift. This is consistent with vacuum ultraviolet radiation experiments that have shown that interface traps can be created by non-penetrating radiation [16-18]. In these experiments, the tops of capacitors with thin metal gates were illuminated with non-penetrating VUV radiation. All light was absorbed within the top oxide layer and none of the light reached the Si/SiO_2 interface. However, with a positively applied bias, interface-trap buildup was observed to occur, similar to that for penetrating radiation (high-energy gamma radiation). These experiments confirmed that a negligible number of interface traps are created directly by radiation as would occur due to displacement damage.

We can get some insight into the effects of particle type on formation of electron-hole pairs in silicon by examining the stopping power for electrons and protons in SiO_2 [19,20]. Figure 55 is a plot of the stopping power in SiO_2 for electrons and protons versus particle energy [21].

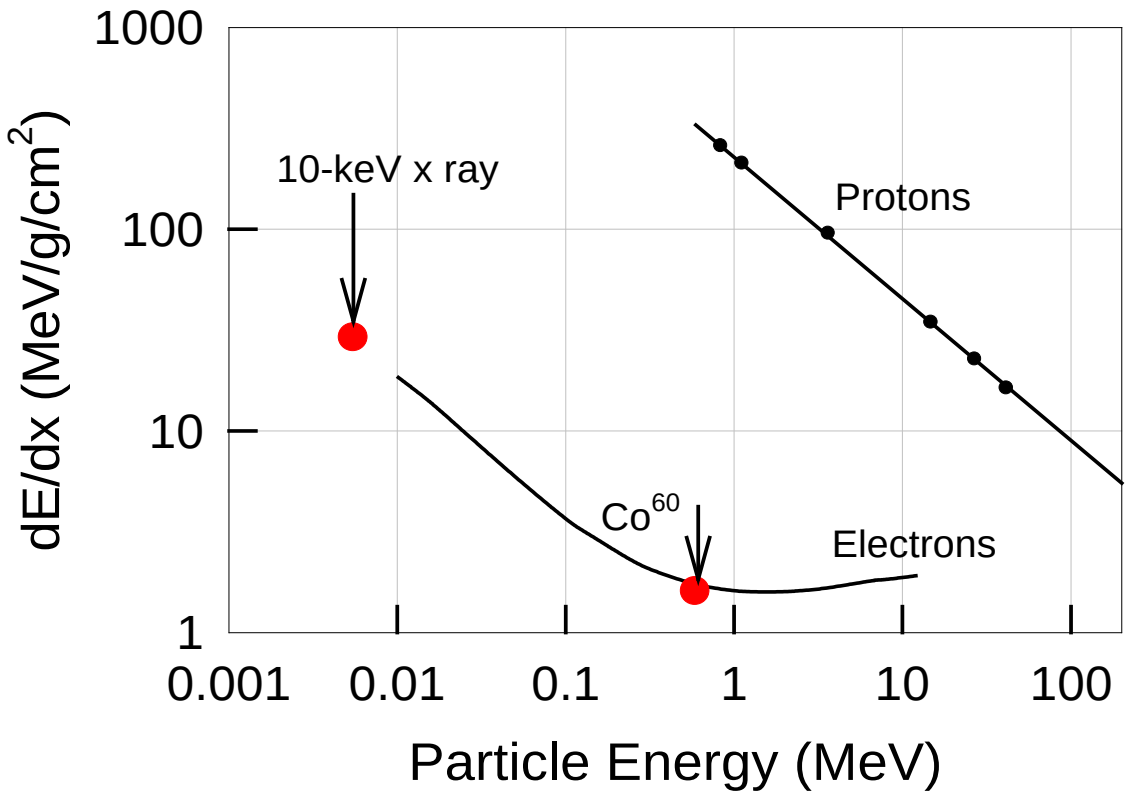

Figure 55: Stopping Power versus Particle Energy for Electrons and Protons

Also shown are the average stopping powers for secondary electrons emitted by 10-keV x rays and 1.2-MeV gamma rays. (After Ref. [21]).

The energy range shown for protons and electrons covers that typically found in space [23]. Also shown in the figure are the calculated average values of stopping power for secondary electrons generated by 10-keV x rays and 1.25-MeV Co-60 gamma rays. These values are based on calculations using the Sandia radiation transport code CEPXS/ONELD [22]. The interaction of a 10-keV photon and a 1.25-MeV photon with a thin layer of SiO_2 produces a secondary electron spectrum with an average energy of ~5.5 keV and ~590 keV, respectively. The stopping power of the electrons generated by a 10-keV photon more closely matches the stopping power of the lower energy protons (~20 to 60 MeV) than the stopping power of electrons generated by a 1.25-MeV photon. On the other hand, the stopping power of the electrons generated by a Co-60 photon more closely matches the stopping power of the electrons in space (up to 7 MeV) [23].

For low stopping powers (high-energy electrons and the secondary electrons generated by a Co-60 photon), the initial separation between a hole and its corresponding electron after they reach thermal

equilibrium and the mean separation between electron/hole pairs is relatively large. For this case, the geminate model for recombination is appropriate [21]. Because the electron/hole pairs are widely separated, the model predicts that the initial charge yield (the number of electron/hole pairs that escape initial recombination) is relatively high. Thus, we can envisage that the initial charge yields for high-energy electrons and for the secondary electrons generated by a Co-60 photon are high and approximately equal. For high stopping powers (such as those of low energy protons), the initial separation between a hole and its corresponding electron after they reach thermal equilibrium and the mean separation between electron/hole pairs is relatively short. For this case, the columnar model for recombination is appropriate [21]. Because a short distance separates the electron/hole pairs, one may expect more recombination and that the initial charge yield will be relatively low. Therefore, at low proton energies or for low-energy x-rays the charge yield is low because the distance between electron hole pairs is short.

As a result, we can expect that the number of electron/hole pairs and hence, the radiation-induced degradation generated by low energy protons will be similar to that for the secondary electrons generated by a 10-keV photon (x-ray) This was indeed found to be the case [24]. Similarly, we can expect that the number of electron/hole pairs and hence, the radiation-induced degradation generated by high-energy electrons will be similar to that for the secondary electrons generated by a Co-60 photons. This has also been shown to be the case [25].

5 References

1 E F Hartman, T A Zarick, T J Sheridan, and J C Riordan, “Spectral Unfolds of PITHON Flash X-ray Source”, Sandia National Laboratories Report SAND2007-7667, December 2007.[1]

2 E F Hartman and T A Zarick, “A Test Protocol to Screen Capacitors for Radiation-Induced Charge Loss”, Sandia National Laboratories Report SAND2008-5577, September 2008.

3 Specific Heat of Pure Silicon, A Report to Sandia National Laboratories, by Robert Taylor, January 2004, Thermophysical Properties Research Laboratory, Inc., TPRL 3103.

4 Claude Leroy and Pier-Giorgio Rancoita, Rep. Prog. Phys. **70**, 493 (2007).

5 F. E. Doany, D. Grischkowsky, Appl. Phys. Lett. **52**, 36 (1988).

6 H. Schlangenotto, H. Maeder, W. Gerlach, Phys. Stat. Sol. (A) **21**, 357 (1974).

7 S. W. S. McKeever, B. Jassemnejad, J. F. Landreth, J. Appl. Phys. **60** (3), 1124.

8 B. Jassemnejad, R. J. Abbundi, M. D. Brown, S. W. S. McKeever, Phys. Stat. Sol. (A) **108**, 753 (1988).

9 A. C. Lewandowski, T. M. Wilson, Phys. Rev. B, **52** (1), 100 (1995).

10 O. S. Oen, in *Radiation Effects in Semiconductors*, edited by F. L. Vook (Plenum, New York, 1968), p. 264.

11 J. Kalef-Ezra and Y. S .Horowitz, Int. J. Appl. Radiat. Isot. **33**, 1085, 1982.

12 M. L. Sanjuán, P. B. Oliete, V. M. Orera, J. Phys.: Condens. Matter **6**, 9647 (1994).

13 G. J. Brucker, E. G. Stassinopoulos, O. Van Gunten, L. S. August, and T. M. Jordan, IEEE Trans. Nucl. Sci. NS-30, 4383

14 (1982), E. G. Stassinopoulos, G. J. Brucker, O. Van Gunten, A. R. Knudson, T. M. Jordan, IEEE Trans. Nucl. Sci. NS-30, 1880 (1983).

15 T. R. Oldham and F. B. McLean, IEEE Trans. Nucl. Sci. **50**, 483 (2003).

16 P. S. Winokur and M. M. Sokoloski, “Comparison of Interface State Buildup in MOS Capacitors Subjected to Penetrating and Nonpenetrating Radiation,” Appl. Phys. Lett. vol. 28, no. 10, pp. 627-630, May 1976.

17 P. S. Winokur, J. M. McGarrity, and H. E. Boesch, Jr., “Dependence of Interface-State Buildup on Hole Generation and Transport in Irradiated MOS Capacitors,” IEEE Trans. Nucl. Sci. vol. 23, no. 6, pp. 1580-1585, Dec. 1976.

18 R. J. Powell and G. F. Derbenwick, “Vacuum Ultraviolet Radiation Effects in SiO2,” IEEE Trans. Nucl. Sci. vol. 18, no.6, pp. 99-105, Dec. 1971.Effect of particle type on formation of electron-hole pairs in silicon

19 J. R. Schwank, “Total-Dose Effects in MOS Devices,” in 2002 IEEE Nuclear and Space Radiation Effects Conference Short Course, pp. III-1 to III-123.

20 J. R. Schwank, M. R. Shaneyfelt, P. Paillet, D. E. Beutler, V. Ferlet-Cavrois, B. L. Draper, R. A. Loemker, P. E. Dodd, and F. W. Sexton, “Optimum Laboratory Radiation Source for Hardness Assurance Testing,” IEEE Trans. Nucl. Sci. vol. 48, pp. 2152-2157, Dec. 2001.

21 T. R. Oldham, “Analysis of Damage in MOS Devices for Several Radiation Environments,” IEEE Trans. Nucl. Sci. vol. 31, no. 6, pp. 1236-1241, Dec. 1984.

22 L. J. Lorence, “II. Radiation Transport Phenomena and Modeling,” in 1997 IEEE Nuclear and Space Radiation Effects Conference Short Course, Snowmasss, Colorado, July 1997, pp. IIA-1 to II A-29.

23 E. G. Stassinopoulos and J. P. Raymond, “The Space Radiation Environment for Electronics,” Proc. of the IEEE vol. 76, no. 11, pp. 1423-1442, Nov. 1988.

24 J. R. Schwank, M. R. Shaneyfelt, P. Paillet, D. E. Beutler, V. Ferlet-Cavrois, B. L. Draper, R. A. Loemker, P. E. Dodd, and F. W. Sexton, “Optimum Laboratory Radiation Source for Hardness Assurance Testing,” IEEE Trans. Nucl. Sci. vol. 48, pp. 2152-2157, Dec. 2001.

25 P. Paillet, J. R. Schwank, M. R. Shaneyfelt, V. Ferlet-Cavrois, R. L. Jones, O. Flament, and E. W. Blackmore, “Total Dose Hardness Assurance Testing using Laboratory Radiation Sources,” IEEE Trans. Nucl. Sci. vol. 50, no. 6, pp. 2310-2315, Dec. 2003.

Distribution

1 MS 0417	D. M. Fordham	00543
1 MS 0447	J. F. Nagel, Jr.	2127
1 MS 0453	M. A. Rosenthal	2130
1 MS 0457	R. A. Paulsen, Jr.	2211
1 MS 0513	J. D. McBrayer	5335
1 MS 0671	C. A. Coverdale	5935
1 MS 1083	M. R. Shaneyfelt	17311
1 MS 1083	P. E. Dodd	17311
1 MS 1083	J. R. Schwank	17311
1 MS 1145	P. S. Raglin	1380
1 MS 1146	P. J. Griffin	1384
1 MS 1146	K. O. Reil	1384
1 MS 1146	D. B. King	1384
1 MS 1152	C. D. Turner	1653
1 MS 1152	M. Caldwell	1653
1 MS 1152	M. F. Pasik	1654
1 MS 1152	B. D. Seidel	1654
1 MS 1159	J. W. Bryson	1344
1 MS 1159	V. H. Harper-Slaboszewicz	1344
1 MS 1159	C. E. Hembree	1344
1 MS 1159	J. Mcdonald	1344
1 MS 1167	T. A. Zarick	1343
1 MS 1167	K. M. Horn	1343
1 MS 1167	M. L. McLain	1343
1 MS 1167	T. J. Sheridan	1343
2 MS 1167	E. F. Hartman	1343
1 MS 1169	J. R. Lee	1300
1 MS 1179	M. A. Hedemann	1340
1 MS 1179	W. C. Fan	1341
1 MS 1179	H. P. Hjalmarson	1341
1 MS 1179	S. D. Pautz	1341
1 MS 1179	C. R. Drumm	1341
1 MS 1179	L. Lorence	1341
1 MS 1179	B. C. Franke	1341
1 MS 1219	D. E. Beutler	5923
1 MS 1219	V. K. Hernandez	5923
1 MS 9004	W.P. Ballard	8100
1 MS 9106	C. L. Turner	8226
1 MS 9106	D. L. Gehmlich	8226
1 MS 9154	R. E. Oetken	8244
1 MS 9154	S. E. Faas	8244
1 MS 0899	Technical Library	9536 (electronic copy)


Sandia National Laboratories